Dissertation

Giant absorption of neutrons

Ausgeführt zum Zweck der Erlangung des akademischen Grades eines Doktors der technischen Wissenschaften

unter der Leitung von

Em.O.Univ.Prof. Dipl.-Ing. Dr.techn. Helmut Rauch
E141
Atominstitut

eingereicht an der Technischen Universität Wien
Fakultät für Physik

von

Dipl. Ing. Juri Schroffenegger
0425944
Neureutherstr. 8
80799 München

Wien, am 26.3.2016

Kurzfassung

In dieser Arbeit werden mehrere Experimente zum Thema Riesenabsorption von Neutronen beschrieben. Darunter ist der Anstieg des Absorptionsquerschnittes gemäß seiner Abhängigkeit zum Kehrwert der Neutronengeschwindigkeit von stark absorbierenden Materialien wie zum Beispiel Gd zu verstehen.

Ein weiterer untersuchter Aspekt ist ob diese $1/v$-Abhängigkeit auch für gegen Null tendierende Geschwindigkeiten gilt.

Mittels eines Flugzeitmessungsaufbaus werden geschwindigkeitsabhängige Absorptionsquerschnitte bis zu 100 Mb für in schweren Wasser aufgelöstes, isotopisch angereichertes ^{157}Gd gemessen. Eine signifikante Abweichung von der $1/v$-Abhängigkeit kann nicht beobachtet werden.

Die Messung mit einem, zu diesem Zweck konstruierten, Geschwindigkeitsselektor für ultrakalte Neutron liefert Ergebnisse passend zu jenen mit der Flugzeitmethode. Allerdings hat sich diese Methode als weniger praktikabel, weil anfälliger auf Störungen von außen, erwiesen.

Ein neuer Ansatz wird in der Transmissionsmessung von sehr kalten Neutronen durch einen rotierenden Aluminiumzylinder präsentiert. Es kann gezeigt werden, dass sich die Absorption mittels einer Galileitransformation erhöhen lässt, indem die absorbierenden Atomkerne auf die Geschwindigkeit der Neutronen gebracht werden.

Zur Messung des Imaginärteils der Streulänge von Gd wurde eine Reflektometermessung durchgeführt. Diese als phänomenologische Konstante betrachtete Größe, welche neben der $1/v$-Abhängigkeit den Wert des Absorptionsquerschnitts definiert, wird auf diese Weise unabhängig von Absorptionsphänomen ermittelt. Hierbei wurde ein Wert von 12.81 ± 0.47 fm ermittelt.

Abstract

In the present work several experiments related to the giant absorption of neutrons are discussed. This means the increase of the absorption cross section according to its reciprocal proportionality to the neutron velocity of strongly absorbing materials like Gd.

Beside the measurement of as large as possible absorption cross sections the focus is here on the validity of this 1/v-dependency for velocities tending to 0 m/s.

Absorption cross sections up to 100 Mb are measured with a time-of-flight setup. Hereby isotropically enriched ^{157}Gd dissolved in heavy water was used as sample. A significant violation of the 1/v-dependency has not been observed.

The measurement is repeated with a velocity selector setup. For this purpose a new velocity selector adapted to the velocity range of the ultra-cold neutron spectrum was constructed. The results match them achieved with the time-of-flight method, although this method has been proven to be less practical, because it is more sensitive to exterior influences.

A new concept is used in the measurement of very-cold neutron transmitting a rotating aluminum cylinder. It can be shown that the absorption cross section can be increased using a Galilean transformation. This is done by accelerating the absorbing nuclei in the rotating sample to the velocity neutrons in the medium.

Beside form the neutron velocity the neutron absorption cross section is also described by the imaginary part of neutron scattering length. This quantity is considered to be a phenomenological determined material constant. To obtain a value measured independent of absorption processes it is measured with a reflectometry setup. Hereby a value of 12.81±0.47 fm is determined.

Contents

Contents

6. Conclusion and Outlook   93

Bibliography   97

List of Figures   101

List of Tables   105

Appendix   107

1. Introduction

1. Introduction

According theoretical calculation the neutron absorption cross section is assumed to be reciprocally proportional to the neutron velocity. Away from resonance phenomena multiple measurements for different absorber materials have proven this relation. Measurements using ultra-cold neutrons gave a closer look the behavior of the absorption cross section for very low neutron velocities. Also in this velocity region several measurements confirmed the 1/v-dependency for various materials. In [1] the first time a possible violation of this dependency measured in an experiment is reported. The authors used as absorber Gd in its natural isotopic abundance and enriched ^{157}Gd, what is the material with largest known neutron absorption cross section of all stable isotopes. Additional they were able to realize lower neutron velocities than in the previous experiments by decelerating the neutrons in the optical potential of heavy water, in which the Gd is dissolved.

The results of the publication started a controversial discussion in the neutron-physics community. This gave reason to reinvestigate this effect in the present work. However, the focus is here not only on this single aspect but on the more general subject of the giant absorption of neutrons. With giant absorption hereby the increase of the absorption cross section according to its 1/v-dependency in the lower velocity range is meant. Measurements of as large as possible absorption cross sections is also a goal of this work.

In the first approach to the topic the experiment presented in [1] is repeated with several improvements. Some technical improvements are applied like the use of a new type of chopper, which allows to set the open-time independently form the duty cycle improving thereby the average neutron flux. But also some more fundamental changes are implemented. An absorber foil is placed inside the flightpath. This way all otherwise on the walls of the flightpath reflected neutrons are removed and can not reach the detector. Non specular reflection would falsify the detected neutron spectrum. The flightpath is chosen as short as possible to maintain anyway a large as possible detectable neutron flux.

The measurement provides new data: absorption cross sections up to 100 Mb are measured, but it also shows that the method is at its limits.

To measure the absorption cross section in an alternative way a velocity selector for ultra-cold neutrons was build. Using this new device again the transmission of neutrons through Gd dissolved in heavy water is measured. In this experiment the same principles like in the time-of-flight measurement are applied. However, in this setup non specular reflections are avoided without the use of an additional absorber. This measurement provides results matching with them of the of the time-of-flight measurement, although the method has proven to be less functional, because its more sensitive to exterior influences.

Even if the selector method does not provide new insights in the physical topic of the giant neutron absorption, the selector itself its a technical innovation. It is the first functional apparatus of its kind operating in the velocity region of the ultra-cold neutron spectrum. As part of this work it is tested and characterized. The selector fulfills the requirements presented to it: the neutron spectrum in the range from 0 to 15 m/s can be reduced reproducible to a narrow band with a maximal velocity resolution of $\frac{\delta v}{v} = 16\%$. At the same time the mean velocity is adjustable by a software interface.

On the search of a new approach to the topic of the giant absorption the idea was born to accelerate the absorbing nuclei to the velocity of the neutrons instead of using slow neutrons. This way the neutron-absorber relative velocity is reduced and as consequence the absorption increases. Measurements according to this concept have never been reported before.

The idea is put in practice by an experiment, in which very-cold neutrons are transmitting a rotating aluminum-cylinder. The absorption cross section for this neutrons in the velocity range of 90 m/s is increased by a Galilean transformation with respect to the nuclei in the sample, which is spinning with frequencies up to 500 Hz.

Finally the imaginary part of the bound coherent neutron scattering length b_c'' for a Gd sample is measured in a reflectometry setup. The absorption cross section depends beside the neutron velocity on this quantity, which can be assumed to be a phenomenological material constant. This experiment supplies a value measured independently form absorption phenomena and gives thereby a prove of consistency with the previous experiments.

2. The neutron

2.1. Properties of the neutron

In the present work aspects of the interaction between neutrons and matter are presented. Because of the important role of the neutron in this topic the discussion starts with presentation of its properties. In Tab. 2.1 the most important are listed. As it is apparent from its quark structure

Mass	$m_n = 1.67492728 \pm 0.000000037 \cdot 10^{-27}$ kg
	$A_r(n) = 1.0086649160 \pm 0.0000000004$ u
	$m_n c^2 = 939.565379 \pm 0.000021$ MeV
Mean lifetime	$\tau = 880 \pm 1.1$ s
Electric charge	$q_n = -0.4 \pm 1.1 \cdot 10^{-27}$ e
Electric dipole moment	$d < 2.9 \cdot 10^{-26}$ e cm
Magnetic moment	$\mu_n = -0.966236 \pm 0.00000025 \cdot 10^{-26}$ J/T
	$\mu_n/\mu_N = -1.9130427 \pm 0.0000005$
Spin quantum number	1/2
Quark structure	udd

Table 2.1.: Properties of the neutron [2–4]

the neutron is a baryon and its spin quantum number 1/2 categorizes it as Fermion.

2.2. Interactions of the neutron

As it can be seen from the entries in Tab. 2.1 the neutron is interacting via all four fundamental forces [5]:

- **Gravity**
  Because of its mass the neutron can interact with a gravitational field.
  Most of the experiments discussed in the present work were performed with ultra-cold neutrons (UCN), what implies, that the kinetic energy of the neutrons is below 200 neV. In contrast to thermal neutron experiments, the interaction of the neutron with the Earth's gravitational field can not be neglected. This interaction can be expressed by the gravitational potential:

$$V_g = m_n g h \tag{2.1}$$

  where m_n denotes the neutron mass, g the acceleration in the gravitational field and h the height. Inserting the corresponding values, a change of energy per length unit of $\Delta E_g = 102.4 \frac{\text{neV}}{\text{m}}$ is obtained, what is in the same scale as the kinetic energy in a typical sized UCN-experiment. Manipulating the kinetic energy of an UCN using the gravitational potential is common procedure performing UCN-experiments.

- **Magnetic interaction**
  The neutron, which can be assumed as electrical neutral, can interact through its magnetic moment μ_n with an electromagnetic field. The corresponding potential is given by:

$$V_m = -\boldsymbol{\mu} \cdot \mathbf{B}(\mathbf{r}) \tag{2.2}$$

where $\mathbf{B(r)}$ denotes the magnetic flux density and $\boldsymbol{\mu} = \mu_n \mathbf{s}/\hbar$ is the magnetic moment with the spin $\mathbf{s}$. Similar to the gravitational potential a change in energy per unit of the magnetic field strength can be calculated: $\Delta E_m = \pm 60.3 \frac{\text{neV}}{\text{T}}$, where the sign depends on the orientation of the spin to the field.

- **Weak interaction**
  The weak interaction manifests itself in the β-decay of a free neutron:

$$ \text{n} \to \text{p} + \text{e}^- + \bar{\nu}_\text{e} + 782 \text{keV} \tag{2.3} $$

  with the decay time given by $\tau = 880 \pm 1.1$ s. [2]
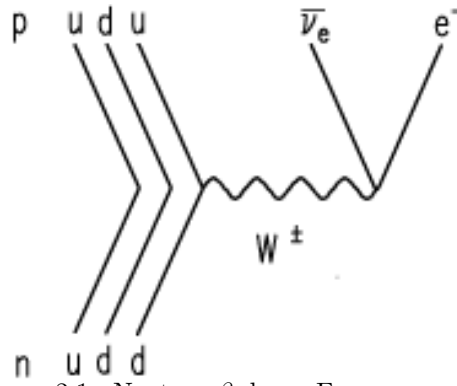 The corresponding Feynman graph is plotted in Fig. 2.1. The transformation of a down-quark

Figure 2.1.: Neutron β-decay Feynman graph.

  into an up-quark, an electron an anti-neutrino via the W-boson is shown there.
  Bound together with protons in a nucleus the neutron is stable. The reason therefore is, that the binding energy in the nucleus exceeds the energy released by the β-decay. For example the binding energy in D^2 is 2.23 MeV, almost three times the decay energy of 782 keV.
  To create a free neutron and use it in an experiment, it must be extracted from the binding in the nucleus. Nuclear reactions like nuclear fission, spallation or fusion can be used to do so.

- **Strong interaction**
  The strong interaction is responsible for the confinement of the neutrons and protons in a nucleus. The potential of the short ranged interaction can be approximated by a spherical square well potential with a depth of about $V_0 \approx 50$ MeV. Its radius is given by $R_0 A^{\frac{1}{3}}$ where A denotes the nucleon number, $R_0 = 1.21$ fm. Better representations of the potential are given by more detailed models like the Fermi form $V_F = V_0/(1 + e^{(r-R_0)/\omega})$. In Fig. 2.2 this both potentials and the corresponding wave function of the neutron are shown. Condition for the calculation of the wave functions is the assumption of a slow moving neutron: $\lambda \gg R_0$.
  The strong interaction processes of a free neutron, which includes scattering and absorption, are discussed in the following chapter.
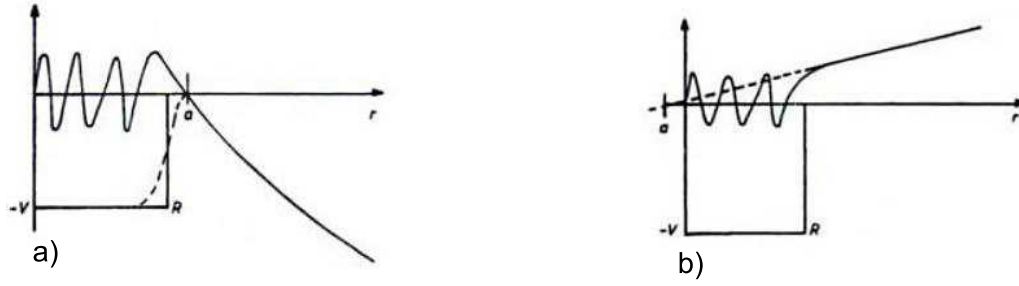
Figure 2.2.: Spherical square well approximation to the neutron-nucleus interaction and the Fermi form (broken curve) for a slow moving neutron in such a potential. a) positive scattering length, b) negative scattering length. [5] p.9

2.3. Strong interaction of a free neutron with matter

Although the focus of the experimental part of this work is mainly on the neutron absorption, it is a topic related so strongly to neutron scattering, that it can not be discussed without the formalisms found in the theoretical treatment of this field. Quantities like the complex optical potential or the scattering length are used to describe scattering as well as absorption.

The following is written along the lines of [6].

2.3.1. Formal theory of neutron interaction

The interaction of the neutron can be expressed in its most general form by a Hamiltonian of the form

$$H = H_0 + V \tag{2.4}$$

where H_0 denotes the Hamiltonian in absence of any interaction and V is the interaction potential. If Φ is the solution of the equation

$$H_0 \Phi = E\Phi \tag{2.5}$$

it represents a possible initial state of the interaction with the total energy E. The final state can be constructed by

$$\Psi = (1 - GV)^{-1} \Phi \tag{2.6}$$

where G denotes the retarded Green function

$$G = (E + i\epsilon - H_0)^{-1} \tag{2.7}$$

for ϵ shall be assumed, that it approaches zero through positive values: $\epsilon \to 0^+$. The reason for this assumption and the function of ϵ itself will discussed in more detail later. According to Eqn. 2.6, Ψ satisfies the equation

$$\Psi = \Phi + GV\Psi \tag{2.8}$$

the so called Lippmann-Schwinger equation.

Multiplying both sides of this equation with G^{-1}, results in

$$(H - E)\Psi = i\epsilon(\Psi - \Phi) \to 0 \tag{2.9}$$

so that

$$H\Psi = E\Psi \tag{2.10}$$

This demonstrates, that Ψ is an eigenstate of H and has the same energy E as Φ the eigenstate of H_0. In the further discussion it will be shown, that the terms of the Lippmann-Schwinger equation, Eqn. 2.8, can be associated on the one hand with a plane wave, what corresponds to Φ, on the other hand with an outgoing spherical wave, corresponding to G. The first expression in the equation represents the incident wave, the second the scattered wave. Ψ can also been seen as the scattered state, that evolves out of the initial sate, when the interaction V is switched on adiabatically within the time constant $\frac{\hbar}{\epsilon}$.

Eqn. 2.6 includes that

$$H\Psi = T\Phi \tag{2.11}$$

where the transition operator T is given by

$$T = V(1 - GV)^{-1} \tag{2.12}$$

The Lippmann-Schwinger equation Eqn. 2.8 can be transformed into

$$\Psi = (1 + GT)\Phi \tag{2.13}$$

The Schrödinger equation Eqn. 2.10 or the equivalent Lippmann-Schwinger equation Eqn. 2.8 can be solved by finding the transition operator T.

Eqn. 2.12 can also be expressed as

$$T = V + TGV \tag{2.14}$$

which leads to an iterativ solution, known as the Born series

$$T = V + VGV + VGVGV + \cdots \tag{2.15}$$

The series can be understood as a multiple scattering expansion, where V is associated with a single scattering process, VGV with double scattering, and so on. Neglecting multiple scattering results in the Born approximation

$$T = V \tag{2.16}$$

A macroscopic system is composed by multiple particles, with which the neutron can interact. Therefore the potential can be expressed as

$$V = \sum_i V_i \tag{2.17}$$

where V_i corresponds to the interaction with the i-th particle. Inserting this into Eqn. 2.15 gives

$$T = V + \sum_i V_i + \sum_{ij} V_i G V_j + \sum_{ijk} V_i G V_j G V_k + \cdots \tag{2.18}$$

here terms of intraparticle multiple scattering $V_i G V_i$ appear as well as terms for interparticle multiple scattering $V_i G V_j$, where $i \neq j$. The Born approximation for intraparticle multiple scattering is here not applicable. For example the formation of the compound-nucleus demonstrates the importance of this terms. Analog to the Eqn. 2.14 T_i can here be defined as the transition operator, which describes the interaction of the neutron with the i-th particle

$$T_i = V_i + T_i G V_i \tag{2.19}$$

Again an iterated solution can be found

$$T_i = V_i + V_i G V_i + V_i G V_i G V_i + \cdots \tag{2.20}$$

A similar expression can be found for V_i by inverting Eqn. 2.19

$$V_i = T_i - T_i G V_i \tag{2.21}$$

with the iterated solution

$$V_i = T_i - T_i G T_i + T_i G T_i G T_i + \cdots \tag{2.22}$$

Inserting this result into Eqn. 2.18 gives

$$T = \sum_i T_i + \sum_{i \neq j} T_i G T_j + \sum_{i \neq j \neq k} T_i G T_j G T_k + \cdots \tag{2.23}$$

This way an expression for T is given in terms of T_i. The intraparticle multiple scattering terms are implicitly summed to infinite order expressed in an explicit interparticle multiple scattering expansion.

Neglecting interparticle multiple scattering leads to the so-called kinematical theory, where Eqn. 2.23 is approximated by

$$T = \sum_i T_i \tag{2.24}$$

Multiple scattering is negligible, assuming the linear dimensions of the sample are chosen sufficiently small.

An expression for T can be found in the kinematical theory, which is formally similar to the Born approximation

$$T = \sum_i V_i \tag{2.25}$$

This way it is not necessary to introduce a model for the potential V_i and solving Eqn. 2.24 for the transition operator, but a model for T_i itself can be introduced, known as the Fermi pseudopotential. It represents a simple phenomenological treatment of the neutron-matter interaction, which is valid for the most applications in condensed-matter physics.

2.3.2. Interaction with a single nucleus

As discussed before in section 2.2 the neutron is able to interact via all four fundamental interaction. But by far the most important interaction in non magnetic material is the strong interaction. For simplicity the interactions of the neutron and the nucleus is therefore reduced to this interaction. A neutron interacting with a nucleus can ether be scattered or it can be absorbed. Avoiding a multichannel formalism both interaction processes can be described using a complex optical potential. The Hamiltonian describing such a system has the form

$$H = \frac{1}{2m_n} \mathbf{p}^2 + V(\mathbf{r}) \tag{2.26}$$

where $\mathbf{p}$ is the neutron momentum, $V(\mathbf{r})$ is the complex optical potential and $\mathbf{r}$ refers to the position of the neutron relative to the nucleus. $V(\mathbf{r})$ can be assumed to be a central potential. Constructing a detailed model of the potential is not necessary, neither for calculating the absorption cross section, nor for the scattering cross section, because both quantities do not depend on the detailed behavior of the potential but only on a single complex parameter, the scattering length. To derive the effect of this in practice phenomenological constant on the neutron-nucleus interaction the Schrödinger equation Eqn. 2.10 with the Hamiltonian given in Eqn. 2.26 must be solved.

To do so, the use of the momentum representation of the wave function as well as its coordinate

representation is helpful. In the momentum representation $|\mathbf{k}\rangle$ denotes the state in which the neutron has the momentum $\hbar\mathbf{k}$,

$$\mathbf{p}\,|\mathbf{k}\rangle = \hbar\mathbf{k}\,|\mathbf{k}\rangle \tag{2.27}$$

These momentum eigenstates form a complete orthonormal set, so that

$$\langle\mathbf{k}|\mathbf{k}'\rangle = \delta(\mathbf{k}-\mathbf{k}'), \quad \int d\mathbf{k}\,|\mathbf{k}\rangle\,\langle\mathbf{k}| = 1 \tag{2.28}$$

The free-particle Hamiltonian

$$H_0 = \frac{1}{2m_n}\mathbf{p}^2 \tag{2.29}$$

is diagonal in the momentum representation,

$$H_0\,|\mathbf{k}\rangle = E_{\mathbf{k}}\,|\mathbf{k}\rangle \tag{2.30}$$

with the energy

$$E_{\mathbf{k}} = \frac{(\hbar k)^2}{2m_n} \tag{2.31}$$

The Green function in Eqn. 2.7 can be written as

$$G = \frac{1}{E_{\mathbf{k}} + i\epsilon - H_0}\int d\mathbf{k}'\,|\mathbf{k}'\rangle\,\langle\mathbf{k}'| = \int d\mathbf{k}'\,\frac{|\mathbf{k}'\rangle\,\langle\mathbf{k}'|}{E_{\mathbf{k}} + i\epsilon - E_{\mathbf{k}'}} \tag{2.32}$$

In the coordinate representation $|\mathbf{r}\rangle$ denotes the state in which the neutron is at the position $\mathbf{r}$. Analog to the momentum representation, also these states form a complete orthonormal set

$$\langle\mathbf{r}|\mathbf{r}'\rangle = \delta(\mathbf{r}-\mathbf{r}'), \quad \int d\mathbf{r}\,|\mathbf{r}\rangle\,\langle\mathbf{r}| = 1 \tag{2.33}$$

The wave function in the state $|\mathbf{k}\rangle$ is given by

$$\phi_{\mathbf{k}}(\mathbf{r}) = \langle\mathbf{r}|\mathbf{k}\rangle = \langle\mathbf{k}|\mathbf{r}\rangle^* \tag{2.34}$$

this quantity is a plane wave with the vector $\mathbf{k}$

$$\phi_{\mathbf{k}}(\mathbf{r}) = (2\pi)^{-\frac{3}{2}}e^{i\mathbf{k}\mathbf{r}} \tag{2.35}$$

In coordinate representation the momentum operator is given by

$$\mathbf{p} = \frac{\hbar}{i}\boldsymbol{\nabla} \tag{2.36}$$

Applying it to the wave function gives

$$\mathbf{p}\phi_{\mathbf{k}}(\mathbf{r}) = \hbar\mathbf{k}\phi_{\mathbf{k}}(\mathbf{r}) \tag{2.37}$$

The free-particle Hamiltonian is given in this notation as

$$H_0 = -\frac{\hbar^2}{2m_n}\Delta \tag{2.38}$$

consequently

$$H_0\phi_{\mathbf{k}}(\mathbf{r}) = E_{\mathbf{k}}\phi_{\mathbf{k}}(\mathbf{r}) \tag{2.39}$$

Applying Eqn. 2.33 to Eqn. 2.32 gives

$$\begin{aligned}
\langle\mathbf{r}\,|G|\,\mathbf{r}'\rangle &= \int d\mathbf{k}'\,\frac{\langle\mathbf{r}|\mathbf{k}'\rangle\,\langle\mathbf{k}'|\mathbf{r}'\rangle}{E_{\mathbf{k}} + i\epsilon - E_{\mathbf{k}'}} \\
&= \int d\mathbf{k}'\,\frac{\phi_{\mathbf{k}'}(\mathbf{r})\phi_{\mathbf{k}'}(\mathbf{r}')^*}{E_{\mathbf{k}} + i\epsilon - E_{\mathbf{k}'}} \\
&= \frac{m_n}{4\pi^3\hbar^2}\int d\mathbf{k}'\,\frac{e^{i\mathbf{k}'\cdot(\mathbf{r}-\mathbf{r}')}}{k^2 + i\eta - k'^2}
\end{aligned} \tag{2.40}$$

2. The neutron

with $\eta = \frac{2m_n\epsilon}{\hbar^2}$.

Solving the integral in the limit $\eta \to 0^+$ gives

$$\langle \mathbf{r} \,|G|\, \mathbf{r}' \rangle = -\frac{m_n}{2\pi\hbar^2} \frac{e^{ik|\mathbf{r}-\mathbf{r}'|}}{|\mathbf{r}-\mathbf{r}'|} \tag{2.41}$$

In the limit $\eta \to 0^+$ the solution has the form of an outgoing spherical wave, it is called the retarded wave. In the limit $\eta \to 0^-$ the solution has a similar form, except the opposite sign in the exponent. This would describe an incoming wave, the so-called advanced wave. The problems boundary conditions demand the retarded Green function.

The final state of the interaction process $\psi_\mathbf{k}$, which satisfies the Schrödinger equation

$$H\psi_\mathbf{k} = E_\mathbf{k}\psi_\mathbf{k} \tag{2.42}$$

can be calculated according to Eqn. 2.13 out of the initial state $|\mathbf{k}\rangle$ by

$$\psi_\mathbf{k} = (1 + GT)\,|\mathbf{k}\rangle \tag{2.43}$$

in coordinate representation

$$
\begin{aligned}
\psi_\mathbf{k}(\mathbf{r}) &= \langle \mathbf{r}|\psi_\mathbf{k}\rangle \\
&= \langle \mathbf{r}| \left(1 + G \int d\mathbf{r}'\, |\mathbf{r}'\rangle \langle \mathbf{r}'|\,T \right) |\mathbf{k}\rangle \\
&= \langle \mathbf{r}|\mathbf{k}\rangle + \int d\mathbf{r}' \,\langle \mathbf{r}|\,G\,|\mathbf{r}'\rangle \langle \mathbf{r}'|\,T\,|\mathbf{k}\rangle \\
&= \phi_\mathbf{k}(\mathbf{r}) + \int d\mathbf{r}\,\langle \mathbf{r}|\,G\,|\mathbf{r}'\,\langle\rangle\,\mathbf{r}'|\,T\,|\mathbf{k}\rangle
\end{aligned}
\tag{2.44}
$$

From this it is evident that the final state wave function $\psi_\mathbf{k}(\mathbf{r})$ is a superposition of the initial state wave function $\phi_\mathbf{k}(\mathbf{r})$ and a spherical outgoing wave $\langle \mathbf{r}|\,G\,|\mathbf{r}'\rangle$ where $\langle \mathbf{r}'|\,G\,|\mathbf{k}\rangle \neq 0$.

$r \gg r'$ is clearly valid at the detector position considering that r' reefers to the size of the interacting nucleus. Because of this the approximation

$$|\mathbf{r}-\mathbf{r}'| = r - \hat{\mathbf{r}} \cdot \mathbf{r}' + O(r^{-1}) \tag{2.45}$$

can be made, where $\hat{\mathbf{r}}$ denotes a unity vector in the direction of $\mathbf{r}$. Hence,

$$k|\mathbf{r}-\mathbf{r}'| = kr - \hat{\mathbf{k}'} \cdot \mathbf{r}' + O(r^{-1}) \tag{2.46}$$

using $\mathbf{k}' = k\mathbf{r}'$. From Eqn. 2.41 then follows that in the limit $r \to \infty$,

$$
\begin{aligned}
\langle \mathbf{r}|\,G\,|\mathbf{r}'\rangle &\to -\frac{m_n}{2\pi\hbar^2} \frac{e^{i(kr-\mathbf{k}'\cdot\mathbf{r})}}{\mathbf{r}} \\
&= -\frac{\sqrt{2\pi}m_n^2}{\hbar} \frac{e^{ikr}}{r} \phi_{\mathbf{k}'}(\mathbf{r'}) \\
&= -\frac{\sqrt{2\pi}m_n}{\hbar^2} \frac{e^{ikr}}{r} \langle \mathbf{k}'|\mathbf{r}'\rangle
\end{aligned}
\tag{2.47}
$$

and hence, form equation Eqn. 2.44, that

$$
\begin{aligned}
\psi_\mathbf{k}(\mathbf{r}) &\to \phi_\mathbf{k}(\mathbf{r}) - \frac{\sqrt{2\pi}m_n}{\hbar^2} \frac{e^{ikr}}{r} \int d\mathbf{r}' \,\langle \mathbf{k}'|\mathbf{r}'\rangle \langle \mathbf{r}'|\,T\,|\mathbf{f}\rangle \\
&= \phi_\mathbf{k}(\mathbf{r}) - \frac{\sqrt{2\pi}m_n}{\hbar^2} \frac{e^{ikr}}{r} \langle \mathbf{k}'|\,T\,|\mathbf{k}\rangle
\end{aligned}
\tag{2.48}
$$

The outgoing waves $\langle \mathbf{r} | G | \mathbf{r}' \rangle$ in Eqn. 2.44 are reduced in the limit $r \to \infty$ to a single spherical wave. What can be written as

$$\psi_{\mathbf{k}}(\mathbf{r}) \to (2\pi)^{-\frac{3}{2}} \left(e^{i\mathbf{k}\cdot\mathbf{r}} + f(\theta)\frac{e^{ikr}}{r} \right) \tag{2.49}$$

where

$$f(\theta) = -\frac{4\pi^2 m_n}{\hbar^2} \langle \mathbf{k}' | T | \mathbf{k} \rangle \tag{2.50}$$

The so-called scattering amplitude $f(\theta)$ gives the angular dependent amplitude of the outgoing wave relative to the incident wave. Contrary to the conventional notation $f(\theta)$ depends on $\mathbf{k}$ and $\mathbf{k}'$ and is not only a function of the angel θ between incoming and outgoing wave.

In Eqn. 2.50 the scattering amplitude is given as the T-matrix-elements between the initial and the final state with an additional constant. To simplify the expression the scattering amplitude operator F can be defined as

$$F = -\frac{4\pi^2 m_n}{\hbar^2} T \tag{2.51}$$

so that

$$f(\theta) = \langle \mathbf{k}' | F | \mathbf{k} \rangle \tag{2.52}$$

The Schrödinger equation Eqn. 2.42 can be written in the coordinate representation as

$$\left(-\frac{\hbar^2}{2m_n}\Delta + V(r) \right) \psi_{\mathbf{k}(\mathbf{r})} = E\psi_{\mathbf{k}(\mathbf{r})} \tag{2.53}$$

The asymptotic behavior for $r \to \infty$ of the equation's solution is given in Eqn. 2.49.

Under the assumption that $V(r)$ is a central potential and that the incident wave is independent on the azimuthal angel, it is evident that $\psi_{\mathbf{k}(\mathbf{r})}$ and, hence, $f(\theta)$ must also be independent of this angel. As consequence the solution of the Schrödinger equation $\psi_{\mathbf{k}(\mathbf{r})}$ can be expanded in terms of Legendre polynomials,

$$\psi_{\mathbf{k}}(\mathbf{r}) = \sum_{l=0}^{\infty} R_l(r) P_l(\cos\theta) \tag{2.54}$$

where the radial coefficients have to satisfy the equation

$$\left[\frac{1}{r^2}\frac{d}{dr}\left(r^2 \frac{d}{dr} \right) + k^2 - \frac{l(l+1)}{r^2} - \frac{2m_n}{\hbar^2}V(r) \right] R_l(r) = 0 \tag{2.55}$$

After some calculation an expression for $f(\theta)$ can be found:

$$f(\theta) = \frac{1}{2ik}\sum_{l=0}^{\infty}(2l+1)(e^{2i\delta_l}-1)P_l(\cos\theta) \tag{2.56}$$

where δ_l is a phase shift induced by the potential V.

Since even for thermal neutrons terms with $l \geq 1$ are negligible, only terms with $l = 0$ have to be taken into account. Using this assumption and the fact that $P_0(\cos\theta) = 1$ follows

$$f(\theta) = \frac{1}{2ik}\left(e^{2i\delta_0} - 1 \right) \tag{2.57}$$

or, equivalently

$$f(\theta) = (k\cot\delta_0 - ik)^{-1} \tag{2.58}$$

where

$$\delta_0 = -kr_0 \tag{2.59}$$

Here r_0 is a measure of the nuclear radius, which is used to calculate δ_l. This is done by approximating the potential V by a hard-sphere potential with radius r_0.

2. The neutron

The details of the calculation, their result is Eqn. 2.58, are not discussed here. Although they have some importance for neutron scattering, for neutron absorption mainly the expansion

$$k \cot \delta_0 = -\frac{1}{a} + \frac{1}{2} r_e k^2 + O(k^4) \tag{2.60}$$

is of importance. This expansion can be done considering that according to Eqn. 2.59 δ_0 is an odd function of k. Consequential, $k \cot \delta_0$ is an even function of k, hence it can be expanded in power series with even exponents. The values a and r_e are introduced here. a is called the scattering length and r_e the effective range. Both parameters are characteristic properties of the optical potential $V(r)$.

Inserting Eqn. 2.60 into Eqn. 2.58 a corresponding expansion for $f(\theta)$ is given by

$$f(\theta) = -a + ika^2 + O(k^2) \tag{2.61}$$

The effective range terms are included in $O(k^2)$. The same expansion is also valid for $l \geq 1$ contributions in Eqn. 2.54, because the additional terms are in order of k^2.

The scattering length a, respectively the corresponding bound coherent scattering length b_c, which will discussed in detail later, is one of the values, their measurement the experimental part of this work is devoted to. In practice it has to be treated as a phenomenological constant and must therefore be measured in the experiment.

In the most cases it is sufficient to use only the first term in the expansion of $f(\theta)$ in Eqn. 2.61, so that it can be assumed

$$f(\theta) = -a \tag{2.62}$$

Comparing that with Eqn. 2.52, what can be written as

$$\begin{aligned} f(\theta) &= \langle \mathbf{k}' | F | \mathbf{k} \rangle \\ &= \int d\mathbf{r} \phi_{\mathbf{k}'}^* F(\mathbf{r}) \phi_{\mathbf{k}} \\ &= \frac{1}{(2\pi)^3} \int d\mathbf{r} e^{i(\mathbf{k}-\mathbf{k}' \cdot \mathbf{r})} F(\mathbf{r}) \end{aligned} \tag{2.63}$$

where $F(\mathbf{r})$ is the scattering amplitude operator in the coordinate representation, leads to

$$F(\mathbf{r}) = -(2\pi)^3 a \delta(\mathbf{r}) \tag{2.64}$$

or in combination with Eqn. 2.51 to

$$T(\mathbf{r}) = \frac{2\pi \hbar^2}{m_n} a \delta(\mathbf{r}) \tag{2.65}$$

$T(\mathbf{r})$ is the already mentioned Fermi pseudopotential. The scattering length a is in general complex. For the most isotopes its imaginary part is in the same order of magnitude as the second term in Eqn. 2.61, but for strongly absorbing isotopes it can be in the same order of magnitude as the real part. In such situations the further terms of the expansion can not be neglected, so that Eqn. 2.62 is not valid. Therefrom follows, that, while the neutron scattering amplitude is for all practical purposes uniquely determined by the scattering length, it is not always adequately described by the Fermi pseudopotential.

2.3.3. Cross sections

Assuming a complex optical potential

$$V(\mathbf{r}) = V'(\mathbf{r}) - iV''(\mathbf{r}) \tag{2.66}$$

allows, as already mentioned, the description of scattering and absorption without introducing a multichannel process. Therefore the consideration of the time dependent Schröding equation is necessary:

$$i\hbar\dot{\Psi}(\mathbf{r},t) = \left(-\frac{\hbar}{2m_n}\Delta + V(\mathbf{r})\right)\Psi(\mathbf{r},t) \tag{2.67}$$

where $\dot{\Psi}(\mathbf{r},t)$ is the differentiation of $\Psi(\mathbf{r},t)$ with respect to the time t. With the definition of the quantities

$$\begin{aligned}
\rho &= |\Psi|^2 \\
\mathbf{J} &= \mathrm{Re}(\Psi^*\mathbf{v}\Psi) \\
s &= \frac{2}{\hbar}\rho V
\end{aligned} \tag{2.68}$$

where $\mathbf{v}$ is the group velocity of the neutron,

$$\mathbf{v} = \frac{1}{m_n}\mathbf{p} = \frac{\hbar}{im_n}\boldsymbol{\nabla} \tag{2.69}$$

from Eqn. 2.66 follows

$$\dot{\rho} + \mathrm{div}\mathbf{J} = -s \tag{2.70}$$

This equation can be interpreted as an equation of continuity in which ρ is the neutron number density, $\mathbf{J}$ is the neutron current density and s is the neutron sink density. The total neutron number in the volume V follows from

$$N = \int_V \rho\,d\mathbf{r} \tag{2.71}$$

so that

$$\dot{N} = -\int_V (\mathrm{div}\mathbf{J} + s)\,d\mathbf{r} \tag{2.72}$$

According the Gauss' theorem

$$\int_V \mathrm{div}\mathbf{J}\,d\mathbf{r} = \int_S \mathbf{J}\cdot\hat{\mathbf{n}}\,dS \tag{2.73}$$

where $\hat{\mathbf{n}}$ is an unit vector normal to the surface S that bounds V, and dS is an element of the surface area. Hence,

$$\dot{N} = \int_S \mathbf{J}\cdot(-\hat{\mathbf{n}})\,dS - \int_V s\,d\mathbf{r} \tag{2.74}$$

This equation states, that the rate of increase in the number of neutrons in V is equal to the rate at which neutrons are flowing int V through S, minus the rate at which neutrons are being absorbed. Using the stationary state $\psi_{\mathbf{k}}$ with the energy $E_{\mathbf{k}}$, which satisfies the time-independent Schröding equation, for $\Psi_{\mathbf{k}}(\mathbf{r},t)$ follows

$$\Psi_{\mathbf{k}}(\mathbf{r},t) = e^{-iE_{\mathbf{k}}t/\hbar}\psi_{\mathbf{k}} \tag{2.75}$$

For the time-independent case the quantities ρ and $\mathbf{J}$ can be redefined as

$$\rho = |\psi_{\mathbf{k}}(\mathbf{r})|^2 \ , \ \mathbf{J} = \mathrm{Re}(\psi_{\mathbf{k}}(\mathbf{r})^*\mathbf{v}\psi_{\mathbf{k}}(\mathbf{r})) \tag{2.76}$$

Eqn. 2.49 can be normalized to represent an incident neutron beam

$$\psi_{\mathbf{k}}(\mathbf{r}) \to \sqrt{\rho_0}\left(e^{i\mathbf{k}\cdot\mathbf{r}} + f(\theta)\frac{e^{ikr}}{r}\right) \tag{2.77}$$

2. The neutron

where ρ_0 denotes the neutron number density.

The incident neutron current density is given by

$$\mathbf{J} = \rho_0 \mathbf{v} \tag{2.78}$$

where $\mathbf{v} = \hbar \mathbf{k}/m_n$ is the incident neutron velocity. Using $\hat{\mathbf{k}}$, the unity vector in the direction of $\mathbf{k}$, the velocity can be rewritten as $\mathbf{v} = v\hat{\mathbf{k}}$ where $v = \hbar k/m_n$. For $\mathbf{J}$ follows

$$\mathbf{J} = J\hat{\mathbf{k}} \tag{2.79}$$

where J is called the incident flux and is given by

$$J = \rho_0 v \tag{2.80}$$

The flux of the outgoing wave J' represents the radial component of the outgoing current density $\mathbf{J}'$, so that

$$J' = \mathbf{J}' \cdot \hat{\mathbf{r}} \tag{2.81}$$

where $\hat{\mathbf{r}}$ is the unit vector in direction of $\mathbf{r}$. For the limit $r \to \infty$ follows

$$J' = J\frac{|f(\theta)|^2}{r^2} \tag{2.82}$$

The solid angle that is given by the area S can be approximated in the limit $r \to \infty$ by

$$d\Omega = \frac{S}{r^2} \tag{2.83}$$

According its definition the differential scattering cross section $d\sigma$ is the average number of neutrons scatter into $d\Omega$ per unit time per unit incident flux. It can be expressed in terms of J and J' as

$$d\sigma = \frac{J'S}{J} \tag{2.84}$$

Using Eqn. 2.82 and Eqn. 2.83 it can be written as

$$d\sigma = |f(\theta)|^2 d\Omega \tag{2.85}$$

respectively

$$\frac{d\sigma}{d\Omega} = |f(\theta)|^2 \tag{2.86}$$

Eqn. 2.86 has a central importance in neutron scattering and will help to calculate the absorption cross section, the corresponding value for neutron absorption.

With the help of Eqn. 2.52 it can be also written as

$$\frac{d\sigma}{d\Omega} = |\langle k'| F |k\rangle|^2 \tag{2.87}$$

The total scattering cross section σ_s follows from an integration over the solid angle

$$\sigma_s = \int d\sigma = \int_{4\pi} |f(\theta)|^2 d\Omega \tag{2.88}$$

Decomposing $d\Omega$ into $d\Omega = \sin\theta d\theta d\phi$ and using the fact that $f(\theta)$ is for a central potential independent of ϕ, σ_s can also be written as

$$\sigma_s = 2\pi \int_0^\pi |f(\theta)|^2 \sin\theta \, d\theta \tag{2.89}$$

Using Eqn. 2.56 and the orthonormality relation for the Legendre polynomials

$$\int_{-1}^{1} P_l(x) P_{l'}(x) dx = \frac{2}{2l+1} \delta_{ll'} \tag{2.90}$$

for σ_s follows

$$\sigma_s = \frac{\pi}{k^2} \sum_{l=0}^{\infty} (2l+1) |e^{2i\delta_l} - 1|^2 \tag{2.91}$$

Finally the absorption cross section can be introduced, the quantity on which is the main focus of the practical part of the present work. It is defined as the average number of absorbed neutrons per unit time per unit incident flux:

$$\sigma_a = \frac{1}{J} \int_V s \, d\mathbf{r} \tag{2.92}$$

where V refers to the volume which contains the nucleus. Under the premise that ρ is constant in time what implies $\dot{N} = 0$ follows from Eqn. 2.74 that

$$\sigma_a = \frac{1}{J} \int_S \mathbf{J}' \cdot (-\hat{\mathbf{n}}) \, dS \tag{2.93}$$

$\mathbf{J}'$ denotes the total current density of the incoming and the outgoing neutron wave.
To simplify matters V can be assumed to be a sphere of radius r ,where $r \to \infty$, so that

$$\sigma_a = \frac{r^2}{J} \int_{4\pi} \mathbf{J}' \cdot \hat{\mathbf{r}} \, d\Omega \tag{2.94}$$

Analog to the scattering cross section the absorption cross section can be rewritten as function of the phase shift δ_l using Eqn. 2.56:

$$\sigma_a = \frac{\pi}{k^2} \sum_{l=0}^{\infty} (2l+1)(1 - |e^{2i\delta_l}|^2) \tag{2.95}$$

in this notation it is obvious that σ_a is only than different from 0 when δ_l is complex

$$\delta_l = \delta_l' + i\delta_l'' \tag{2.96}$$

inserting this in Eqn. 2.91 and Eqn. 2.95 follows

$$\sigma_s = \frac{\pi}{k^2} \sum_{l=0}^{\infty} (2l+1)(1 + e^{-4\delta_l''} - 2e^{-2\delta_l''} \cos(2\delta_l)) \tag{2.97}$$

and

$$\sigma_a = \frac{\pi}{k^2} \sum_{l=0}^{\infty} (2l+1)(1 - e^{4\delta_l''}) \tag{2.98}$$

The sum of absorption cross section and scattering cross section is called the total collision cross section. It denotes the average number of neutrons interacting with the nucleus per unit time per unit incident flux

$$\sigma_t = \sigma_a + \sigma_s \tag{2.99}$$

Inserting Eqn. 2.97 and Eqn. 2.98 gives

$$\sigma_t = \frac{\pi}{k^2} \sum_{l=0}^{\infty} (2l+1)(1 - e^{-2\delta_l''} \cos(2\delta_l')) \tag{2.100}$$

Comparing this equation with Eqn. 2.56, setting $\theta = 0$ and taking into account that $P_l(1) = 1$ results in

$$\sigma_t = \frac{4\pi}{k} \text{Im}[f(0)] \tag{2.101}$$

what is known as the optical theorem. It will be used to find a more practical equation for the cross sections.

Returning to Eqn. 2.86 and inserting the expansion of $f(\theta)$ found in Eqn. 2.61 and a complex scattering length

$$a = a' - ia'' \tag{2.102}$$

gives

$$\begin{aligned}\frac{d\sigma}{d\Omega} &= (a'^2 + a''^2)[1 - 2ka'' + O(k^2)] \\ &= |a|^2[1 - 2ka'' + O(k^2)]\end{aligned} \tag{2.103}$$

so that

$$\sigma_s = 4\pi|a|^2[1 - 2ka'' + O(k^2)] \tag{2.104}$$

The same procedure but using the optical theorem Eqn. 2.101 instead of Eqn. 2.86 gives an expression for the total collision cross section

$$\sigma_t = \frac{4\pi}{k}a'' + 4\pi(a'^2 - a''^2) + O(k) \tag{2.105}$$

An expression for the absorption cross section is obtained by subtracting Eqn. 2.104 from Eqn. 2.105

$$\sigma_a = \frac{4\pi}{k}a''[1 - 2ka'' + O(k^2)] \tag{2.106}$$

Taking the imaginary part of the scattering length of isotopic pure ^{157}Gd, which is the highest of all stable isotopes, $a = 47$ fm [7] and the a wave length of 40 Å, which is the lowest appearing in the following experiments, $ka'' \approx 7 \cdot 10^{-5}$ what is much less then unity. Therefore the terms in the order of k and higher in Eqn. 2.104 and Eqn. 2.106 can be neglected, so that

$$\sigma_s = 4\pi|a|^2 \tag{2.107}$$

and

$$\sigma_a = \frac{4\pi}{k}a'' \tag{2.108}$$

This last equation, with slightly modification that will discussed in the next section, is one of the things the experimental part of this work focus is on. It will be tested on its general validity, specially for k tending to zero.

2.3.4. Bound and coherent scattering length

It has been mentioned that a has to be treated as a phenomenological constant, what implies that it can not be calculated but have to be measured. Since there have been made some assumptions in the derivation of the scattering length which not match with circumstances in an experiment, the concept of the scattering length must be slightly modified to obtain a quantity that can be extrapolated from a measurement. For example up to now the nucleus has been assumed to be fixed in space. Abandoning this assumption and solving the two-body problem leads to the concept of the bound scattering length b. Another restriction that must be abandoned is the spin-independence of the interaction, what finally leads to the bound coherent scattering length b_c. It is this quantity their values are accessible in the experiment and are tabulated in the corresponding literature.

But first to the two body problem: the Hamiltonian of a system of a neutron colliding with an atom can be written as

$$H = \frac{1}{2M}\mathbf{P}^2 + \frac{1}{2m}\mathbf{p}^2 + V(\mathbf{r} - \mathbf{R}) \tag{2.109}$$

where capital letters here refer to the atom, so that M is the atoms mass, R is its position and $P = M\dot{\mathbf{R}}$ is its momentum. The lower case letters are the corresponding values of the neutron and $V(\mathbf{r} - \mathbf{R})$ is as before the complex optical potential.

The Hamiltonian can be rewritten as

$$H = \frac{1}{2M_x}\mathbf{P}_x^2 + \frac{1}{2m_0}\mathbf{p}_0^2 + V(\mathbf{r}_0) \tag{2.110}$$

by using

$$M_x = M + m_n , \quad m_0 = \frac{Mm_n}{M+m_n}$$

$$\mathbf{R}_x = \frac{M\mathbf{R}+m_n\mathbf{r}}{M+m_n} , \quad \mathbf{r}_0 = \mathbf{r} - \mathbf{R} \tag{2.111}$$

$$\mathbf{P}_x = M\hat{\mathbf{R}}_x , \qquad \mathbf{p}_0 = m_0\hat{\mathbf{r}}_0$$

This way the two body problem is reduced to two one body problems. The entire system is moving free in space, what is described by the first term of the Hamiltonian $\frac{1}{2M_x}\mathbf{P}_x^2$, while the second part $\frac{1}{2m_0}\mathbf{p}_0^2 + V(\mathbf{r}_0)$ refers to the interaction between both particles. This second part is identical with Eqn. 2.26, except the neutron mass m_n is replaced by the reduced mass m_0.

In the laboratory system momentum conservation is given by

$$\mathbf{k} + \mathbf{K} = \mathbf{k}' + \mathbf{K}' \tag{2.112}$$

when the neutron has the momentum $\mathbf{p} = \hbar\mathbf{k}$ and $\mathbf{P} = \hbar\mathbf{K}$ is the atoms momentum. The primed quantities refer to the state after the interaction. Momentum transfer can therefore be defined as

$$\mathbf{q} = \mathbf{k} - \mathbf{k}' = \mathbf{K} - \mathbf{K}' \tag{2.113}$$

Energy conservation is given by

$$\epsilon + \frac{\hbar K^2}{2M} = \epsilon' + \frac{\hbar K'^2}{2M} \tag{2.114}$$

$\hbar\epsilon$ donates the neuron energy

$$\hbar\epsilon = E_{\mathbf{k}} = \frac{(\hbar K)^2}{2m_n} \tag{2.115}$$

Analog to the momentum transfer the energy transfer can be defined as

$$\omega = \epsilon - \epsilon' = \frac{\hbar}{2M}(K'^2 - K^2) \tag{2.116}$$

Expressing the energy transfer in term of momentum transfer leads to

$$\omega = \omega_r + \mathbf{q} \cdot \mathbf{V} \tag{2.117}$$

with $\hbar\omega_r = \frac{(\hbar q)^2}{2M}$ what corresponds to the energy transfer to an atom what is initially at rest and $\mathbf{V} = \frac{\hbar\mathbf{K}}{M}$ the atom's initial velocity. Changing from the laboratory system to the center-of-mass system these quantities get an index 0

$$\mathbf{q}_0 = \mathbf{k}_0 - \mathbf{k}_0' , \quad \omega_0 = \epsilon_0 - \epsilon_0' \tag{2.118}$$

In contrast to the energy conservation momentum conservation is not given in the center-of-mass system, so that $\mathbf{q}_0 \neq 0$. The transition from laboratory system to center-of-mass system is done in respect to the relative velocity $\dot{\mathbf{r}}_0 = \dot{\mathbf{r}} - \dot{\mathbf{R}}$, in terms of $\mathbf{k}$

$$\frac{\hbar\mathbf{k}_0}{m_0} = \frac{\hbar\mathbf{k}}{m_n} - \frac{\hbar\mathbf{K}}{M} \tag{2.119}$$

so that

$$\mathbf{k}_0 = \frac{A}{A+1}(\mathbf{k} - \mathbf{K}) \tag{2.120}$$

A is the ratio of atom mass to neutron mass $A = \frac{M}{m_n}$ what is approximately the nucleus' mass number. Analog

$$\mathbf{k}_0' = \frac{A}{A+1}(\mathbf{k}' - \mathbf{K}') \tag{2.121}$$

Apparently the momentum transfer is equal in both systems:

$$\mathbf{q}_0 = \mathbf{q} \tag{2.122}$$

Also,

$$\omega_0 = \omega - \omega_r - \mathbf{q} \cdot \mathbf{V} = 0 \tag{2.123}$$

From Eqn. 2.112 and Eqn. 2.121 follows

$$\mathbf{k}' = \mathbf{k}_0' + \frac{\mathbf{k} + \mathbf{K}}{A+1} \tag{2.124}$$

so that

$$d\mathbf{k}' = d\mathbf{k}_0' \tag{2.125}$$

Transforming $d\mathbf{k}'$ into polar coordinates gives

$$d\mathbf{k}' = k'^2 \, dk' \sin\theta \, d\theta \, d\phi = \frac{m_n k'}{\hbar} \, d\Omega' \, d\epsilon' \tag{2.126}$$

and for $d\mathbf{k}_0'$

$$d\mathbf{k}_0' = \frac{m_0 k_0'}{\hbar} \, d\Omega_0' \, d\epsilon_0' \tag{2.127}$$

hence,

$$k' \, d\Omega \, d\epsilon' = \frac{A}{A+1} k_0' \, d\Omega_0 \, d\epsilon_0' \tag{2.128}$$

From Eqn. 2.125 follows

$$J \, d^2\sigma = J_0 \, d^2\sigma \tag{2.129}$$

where $d^2\sigma$ is the double differential cross section, i.e. the average number of neutrons that are scattered into $d\mathbf{k}'$ per unit time per incident flux. The scattering cross section is used here, because the derivation follows [6], a book with focus on neutron scattering. A similar proceeding is also possible using the absorption cross section. J is the incident flux in the laboratory system, respectively J_0 in the canter-of-mass system, what is already defined in Eqn. 2.80

$$J = \rho \frac{\hbar k}{m_n} \quad J_0 = \rho \frac{\hbar k_0}{m_0} \tag{2.130}$$

Solving Eqn. 2.129 explicit on $d^2\sigma$ gives

$$d^2\sigma = \left(\frac{A+1}{A}\right) \frac{k_0}{k} \, d^2\sigma_0 = \eta \, d^2\sigma_0 \tag{2.131}$$

with

$$\eta = \frac{J_0}{J} = \frac{m_n k_0}{m_0 k} = \left(\frac{A+1}{A}\right) \frac{k_0}{k} \tag{2.132}$$

Eqn. 2.131, Eqn. 2.128 and the fact that $k_0' = k_0$ imply that

$$\frac{d^2\sigma}{d\Omega \, d\epsilon'} = \left(\frac{A+1}{A}\right)^2 \frac{k'}{k} \frac{d^2\sigma_0}{d\Omega_0 \, d\epsilon_0'} \tag{2.133}$$

In general,

$$\frac{d\sigma_0}{d\Omega_0} = \int_0^\infty \frac{d^2\sigma_0}{d\Omega_0 \, d\epsilon_0'} \, d\epsilon_0' \tag{2.134}$$

and according to Eqn. 2.103

$$\frac{d\sigma_0}{d\Omega_0} = |a|^2 \tag{2.135}$$

Elastic scattering in the center-of-mass system implies that $d^2\sigma_0$ is only than different from 0 when $\omega_0 = 0$. So that

$$\frac{d^2\sigma_0}{d\Omega_0 \, d\epsilon_0'} = |a|^2 \delta(\omega_0) \tag{2.136}$$

This can be written in terms of the laboratory system by using Eqn. 2.133 and Eqn. 2.123

$$\frac{d\sigma}{d\Omega \, d\epsilon'} = \frac{k'}{k} |b|^2 \delta(\omega - \omega_r - \mathbf{q} \cdot \mathbf{V}) \tag{2.137}$$

where

$$b = b' - ib'' = \left(\frac{A+1}{A}\right) a \tag{2.138}$$

b is finally the bound scattering length. It is identical with the "free" scattering length a beside the term $\frac{A+1}{A}$, which is a result of the transformation from the center-of-mass system to the laboratory system.

To derive expressions for the cross sections analog to Eqn. 2.107 and Eqn. 2.108 in terms of the bound scattering length b the double differential cross section is used

$$\sigma_s = \int\int d^2\sigma = \int\int \eta d^2\sigma_0 \tag{2.139}$$

η what is defined in Eqn. 2.132 can also be expressed in terms of velocity

$$\eta = \frac{v_0}{v} = \sqrt{1 + \frac{V^2 - 2\mathbf{v} \cdot \mathbf{V}}{v^2}} \tag{2.140}$$

where $\mathbf{v}$ denotes the incident neutron velocity in the laboratory system and $\mathbf{v}_0$ the same quantity in the center-of-mass system, which can be written as $\mathbf{v}_0 = \mathbf{v} - \mathbf{V}$.

From the independence of η from $\mathbf{k}_0'$ follows

$$\sigma_s = \eta \int\int d^2 sigma_0 = \eta\sigma_{s0} \tag{2.141}$$

The total scattering cross section in the center-of-mass system σ_{s0} has been already calculated in Eqn. 2.107, hence

$$\sigma_s = 4\pi\eta|a|^2 \tag{2.142}$$

In the case that $\mathbf{V} = 0$, i.e. the atom is initially at rest, from Eqn. 2.140 follows that $\eta = 1$ and so $\sigma_s = \sigma_{s0}$. A finite temperature of the material, the neutrons are interacting with, implies a movement of the atoms, so that for an ideal gas with N atoms follows

$$\sigma_s = 4\pi N \langle \eta \rangle |a|^2 \tag{2.143}$$

$\langle \eta \rangle$ can be calculated in case of a thermodynamical equilibrium from the Maxwell-Boltzmann distribution

$$f(V) = \left(\frac{M}{2\pi k_B T}\right)^{\frac{3}{2}} \exp\left(-\frac{MV^2}{2k_B T}\right) \tag{2.144}$$

as

$$\langle \eta \rangle = 1 + \frac{k_B T}{2AE_{\mathbf{k}}} \tag{2.145}$$

2. The neutron

hence, σ_s depends form the temperature.

To calculate the absorption cross section the equality of absorbed neutrons per unit of time in the laboratory and the center-of-mass system is used

$$J\sigma_a = J_0\sigma_{a0} \tag{2.146}$$

Consequently,

$$\sigma_a = \eta\sigma_{a0} \tag{2.147}$$

like the scattering cross section the absorption cross section in the center of mass system has been already expressed in Eqn. 2.108, so that

$$\sigma_{a0} = \frac{4\pi}{k_0}a'' \tag{2.148}$$

Applying Eqn. 2.132 to this expressions gives

$$\sigma_a = \frac{4\pi}{k}b'' \tag{2.149}$$

It should be noted that in contrast to scattering cross section σ_s the absorption cross section σ_a is independent of the temperature.

This equation is a step closer to the description of transmission experiments, like those which are presented in the following chapters of this work.

To get an even better description of interacting processes between neutrons and atoms, it must be considered that both particles have a spin, which has influence on the interaction. Consequently the optical potential $V(\mathbf{r})$ and hence, the bound scattering length b, depend on the neutron spin $\mathbf{s}$ and the spin of the nucleus $\mathbf{I}$. Considering that $s = \frac{1}{2}$, b can be written in the most general rotationally invariant form as

$$b = b_c + 2[I(I+1)]^{-\frac{1}{2}}b_i\,\mathbf{s}\cdot\mathbf{I} \tag{2.150}$$

where the coefficients b_c and b_i are called the bound coherent and incoherent scattering length.

Since the total spin $\mathbf{J} = \mathbf{I} + \mathbf{s}$ is a constant of motion with eigenvalues $J = I \pm s$, the bound scattering length can be written for given values of J as

$$\begin{aligned} b_+ &= b_c\sqrt{I/(I+1)}b_i \\ b_- &= b_c\sqrt{(I+1)/I}b_i \end{aligned} \tag{2.151}$$

solving this equations on b_c and b_i gives

$$\begin{aligned} b_c &= g_+b_+ + g_-b_- \\ b_i &= \sqrt{g_+g_-}(b_+b_-) \end{aligned} \tag{2.152}$$

with the statistical weight factors

$$g_+ = \frac{I+1}{2I+1}\,,\ g_- = \frac{I}{2I+1} \tag{2.153}$$

which are normalized to

$$g_+ + g_- = 1 \tag{2.154}$$

With a more generalized form of Eqn. 2.87, which includes beside the state $|\mathbf{k}\rangle$ also the state $|Mm\rangle$, which is given by the eigenvalues of I_z and s_z

$$\frac{d\sigma}{d\Omega} = \sum_{M'm'Mm} P_{Mm}|\langle M'm'|F|Mm\rangle|^2 \tag{2.155}$$

it can be shown that

$$\frac{d\sigma}{d\Omega} = \langle |b|^2 \rangle \tag{2.156}$$

where the brackets denote the average of the neutron and nuclear spin states

$$\langle \cdots \rangle = \sum_{Mm} P_{Mm} \langle Mm| \cdots |Mm\rangle \tag{2.157}$$

Hence, for the scattering cross section follows

$$\sigma_s = 4\pi \left\langle |b^2| \right\rangle \tag{2.158}$$

and with a similar derivation as before using the optical theorem

$$\sigma_a = \frac{4\pi}{k} \langle b'' \rangle \tag{2.159}$$

For an unpolarized nucleus,

$$\langle I_\mu \rangle = 0 \ , \ \langle I_\mu I_\nu \rangle = \frac{1}{3} I(I+1)\delta_{\mu\nu} \tag{2.160}$$

as well as for an unpolarized neutron,

$$\langle s_\mu \rangle = 0 \ , \ \langle s_\mu s_\nu \rangle = \frac{1}{4}\delta_{\mu\nu} \tag{2.161}$$

follows that

$$\langle b \rangle = b_c \tag{2.162}$$

so that

$$\sigma_a = \frac{4\pi}{k} b_c'' \tag{2.163}$$

In the polarized case the absorption cross section can be separated in two parts depending on the eigenvalues of J

$$\sigma_a = g_+ \sigma_{a+} + g_- \sigma_{a-} \tag{2.164}$$

with

$$\sigma_{a\pm} = \frac{4\pi}{k} b_\pm'' \tag{2.165}$$

For strongly absorbing materials, where b'' is in the same order of magnitude as b', usually the absorption is only for one spin state high. For example for ^{157}Gd the state $J = I + \frac{1}{2}$ dominates, so that $b_c'' \approx g_+ b_+''$.

Eqn. 2.163 is finally the equation which describes the absorption in a conventional neutron transmission experiment. It is needed to describe the experiments in the present work and on the same time it is tested on its validity by them. b_c is the most general form of the scattering length. What is the reason why its values can be found tabulated in the corresponding literature.

2.3.5. Neutron optics

So far the interaction between neutron and matter has been discussed on the neutron-nucleus level. But for many applications a description on a macroscopic level is much more useful. Such a macroscopic description bases on the introduction of a macroscopic optical potential $V_m(\mathbf{r})$, so that a Schrödinger equation can be formulated

$$\left(-\frac{\hbar}{2m_n} + V_m(\mathbf{r})\right)\psi(\mathbf{r}) = E\psi(\mathbf{r}) \tag{2.166}$$

Since the macroscopic optical potential is in contrast to the nuclear optical potential a week potential, the Born approximation, Eqn. 2.16, respectively its inversion, can be used

$$V_m \approx T_m = \langle T \rangle \tag{2.167}$$

Neglecting local field effects the kinematic expression Eqn. 2.24 can be applied

$$T = \sum_j T_j \tag{2.168}$$

while T_j is given by the Fermi pseudopotential, defined in Eqn. 2.65, here written in terms of bound scattering length

$$T_j = \frac{2\pi\hbar^2}{m_n} b_j \delta(\mathbf{r} - \mathbf{r}_j) \tag{2.169}$$

where b_j denotes the bound scattering length of the j-th atom and $\mathbf{r}_j$ is its position. Finally $V_m(\mathbf{r})$ is

$$V_m(\mathbf{r}) = \left\langle \sum_j \frac{2\pi\hbar^2}{m_n} b_j \delta(\mathbf{r} - \mathbf{r}_j) \right\rangle \tag{2.170}$$

what is the equilibrium value of the total Fermi pseudopotential. It can also be written with the help of the bound scattering length density

$$b(\mathbf{r}) = \sum_j b_j \delta(\mathbf{r} - \mathbf{r}_j) \tag{2.171}$$

as

$$V_m(\mathbf{r}) = \frac{2\pi\hbar^2}{m_n} \langle b(\mathbf{r}) \rangle \tag{2.172}$$

From Eqn. 2.162 under the condition of a mono-atomic system follows

$$\langle b(\mathbf{r})\mathbf{r} \rangle = b_c \langle \mathrm{N}(\mathbf{r}) \rangle \tag{2.173}$$

where $\mathrm{N}(\mathbf{r}) = \sum_j \delta(\mathbf{r} - \mathbf{r}_j)$ is the particle density. If N is homogeneous over the hole medium with the volume V

$$V_m(\mathbf{r}) \rightarrow V_0 = \frac{2\pi\hbar^2}{m_n} N b_c \tag{2.174}$$

In that case the Schrödinger equation Eqn. 2.166 has the solution

$$\psi(\mathbf{r}) = \begin{cases} Ae^{i\mathbf{K}\cdot\mathbf{r}} & \text{inside } V \\ ae^{i\mathbf{k}\cdot\mathbf{r}} & \text{outside } V \end{cases} \tag{2.175}$$

The magnitudes of $\mathbf{K}$ and $\mathbf{k}$ are given by the neutron energy

$$E = \frac{(\hbar K)^2}{2m_n} + V_0 = \frac{(\hbar k)^2}{2m_n} \tag{2.176}$$

The direction of the wave vectors $\mathbf{k}$ and $\mathbf{K}$ and the amplitudes a and A can be calculated by the requiring that $\psi(\mathbf{r})$ and $\boldsymbol{\nabla}\psi(\mathbf{r})$ have to be continuous at the boundary of V.

Analog to light optics an index of refraction can be defined as

$$n = \frac{K}{k} \tag{2.177}$$

In combination with Eqn. 2.176 follows

$$n^2 = 1 - \xi = 1 - \frac{V_0}{E} \tag{2.178}$$

With the help of Eqn. 2.174 and the correlation between wave vector and wavelength $k = 2\pi/\lambda$, ξ can be written as

$$\xi = \frac{4\pi}{k^2}Nb_c = \frac{\lambda}{\pi}Nb_c \tag{2.179}$$

In the more general case of a poly-atomic system the average scattering length density is given by

$$Nb_c = \sum_l N_l b_{cl} \tag{2.180}$$

where l refers to the contribution of the different atomic species.

Eqn. 2.179 gets the form

$$\xi = \left(\frac{\lambda}{\lambda_c}\right)^2 \tag{2.181}$$

if the critical wavelength λ_c is defined as

$$\lambda_c = \sqrt{\frac{\pi}{Nb_c}} \tag{2.182}$$

Later the expression of λ_c in terms of neutron velocity will used frequently

$$v_c = \frac{2\pi\hbar}{\lambda_c m_n} = \frac{2\pi\hbar}{\sqrt{\frac{\pi}{Nb_c}}m_n} \tag{2.183}$$

The relative index of refraction can be defined on the boundary between two media A and B

$$n = \frac{K_A}{K_B} = \frac{n_A}{n_B} \tag{2.184}$$

so that

$$n^2 = \frac{1 - \xi_a}{1 - \xi_B} \tag{2.185}$$

With the equations found yet reflection and refraction of a neutron beam can be calculated. A medium with a plane boundary and an incident neutron beam with the wave vector $\mathbf{k}$ is assumed. The geometry is given in Fig. 2.3. On the assumption that a part of the incident beam is reflected and a part is refracted the Schrödinger equation Eqn. 2.166 has the solution

$$\psi(\mathbf{r}) = \begin{cases} Ae^{i\mathbf{K}\cdot\mathbf{r}} & z > 0 \\ ae^{i\mathbf{k}\cdot\mathbf{r}} + a'e^{i\mathbf{k}'\cdot\mathbf{r}} & z < 0 \end{cases} \tag{2.186}$$

Without loss of generality the incident wave vector can set to

$$\mathbf{k} = (k\cos\phi, 0, k\sin\phi) \tag{2.187}$$

From the requirement that $\psi(\mathbf{r})$ and $\boldsymbol{\nabla}\psi(\mathbf{r})$ have to be continuous at $z = 0$ follows

$$\begin{aligned} \mathbf{k}' &= (k\cos\phi, 0, -k\sin\phi) \\ \mathbf{K} &= (k\cos\phi, 0, n_z k\sin\phi) \end{aligned} \tag{2.188}$$
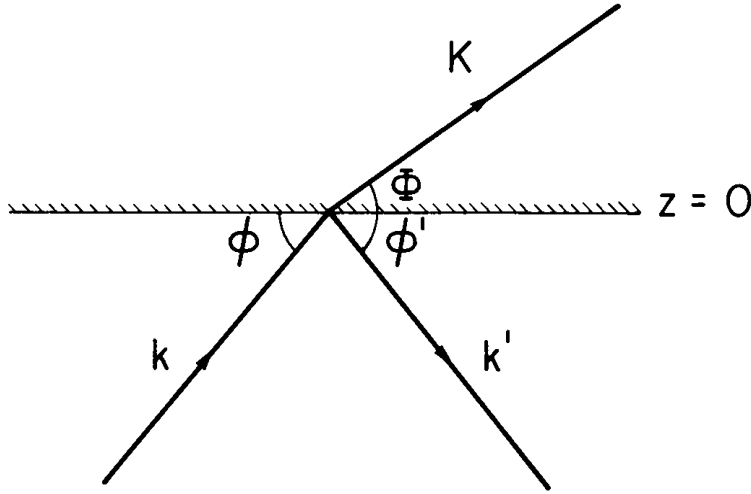
Figure 2.3.: Reflection and refraction at a plane boundary, [6] p.66

as well as

$$a' = \left(\frac{1-n_z}{1+n_z}\right) a$$
$$A = \left(\frac{2}{1+n_z}\right) a$$

$$(2.189)$$

where n_z is the index of refraction in direction z. It is defined as

$$n_z \equiv \frac{K_z}{k_z} = \sqrt{1 - \frac{\xi}{\sin^2 \phi}}$$

$$(2.190)$$

How already mentioned b_c has in general a complex value, consequently ξ and n_z must also considered to be complex

$$n_z = n'_z + in''_z$$

$$(2.191)$$

Hence,

$$\mathbf{K} = \mathbf{K}' + i\mathbf{K}''$$

$$(2.192)$$

with

$$\mathbf{K}' = (k \cos \phi, 0, n'_z k \sin \phi)$$
$$\mathbf{K}' = (0, 0, n''_z k \sin \phi)$$

$$(2.193)$$

In this case the coherent wave in the medium is an inhomogeneous plane wave, what means the planes of constant phase $\mathbf{K}' \cdot \mathbf{r} = $ const are not parallel to the planes of constant amplitude $\mathbf{K}'' \cdot \mathbf{r} = $ const.

Assuming a real $\mathbf{K}$, what is in the most cases a good approximation, follows

$$K_z = n_z k \sin \phi = K sin\Phi$$

$$(2.194)$$

where Φ is the angle of refraction, so that

$$n_z \sin \phi = n \sin \Phi$$

$$(2.195)$$

or

$$\cos \phi = n \cos \Phi$$

$$(2.196)$$

In case of a normal incident neutron beam, what is equivalent to reducing the previous expressions of $\mathbf{K}$ and $\mathbf{k}$ to their z-component the wave vector in the medium is given by

$$K = nk = \sqrt{1 - \frac{V}{E}}\, k \tag{2.197}$$

what can be written with the help of Eqn. 2.174 and Eqn. 2.176 as

$$K = \sqrt{k^2 - \frac{2m}{\hbar^2 k^2} \frac{2\pi \hbar^2}{m} N b_c\, k^2} \tag{2.198}$$

With the use of λ_c, Eqn. 2.182, follows

$$K = \sqrt{k^2 - \frac{4\pi^2}{\lambda_c}} = \sqrt{k^2 - k_c^2} \tag{2.199}$$

or in terms of neutron velocity

$$v = \sqrt{v_0^2 - v_c^2} \tag{2.200}$$

where v_0 denotes the neutron velocity outside the medium. Here the signification of the critical velocity v_c, respectively the critical wavelength λ_c becomes obvious. Since $\mathrm{Re}(v) = 0$ for $v_0 \leq v_c$, for a neutron velocity lower than the critical velocity no refracted beam exists, what can be associated, analogous to light optics, with total reflection. In this case the reflectivity $R = 1$. Hence, v_c is the critical velocity of total reflection at any angle.

For a conventional reflected beam the reflectivity can be calculated as reflected neutron flux per incident flux. According to Eqn. 2.76 the fluxes are given by

$$\begin{aligned}
\mathbf{j} &= \left(\tfrac{\hbar \mathbf{k}}{m}\right) |a|^2 \\
\mathbf{j} &= \left(\tfrac{\hbar \mathbf{k}}{m}\right) |a'|^2 \\
\mathbf{J} &= \left(\tfrac{\hbar \mathbf{K'}}{m}\right) |A|^2 e^{-2\mathbf{K''}\cdot\mathbf{r}}
\end{aligned} \tag{2.201}$$

Hence,

$$R = -\frac{j_z'}{j_z} = \left| \frac{a'}{a} \right|^2 \tag{2.202}$$

The transmissivity is defined in the same way

$$T = \frac{J_z}{j_z} = n_z' \left| \frac{A}{a} \right|^2 \tag{2.203}$$

with Eqn. 2.189 follows

$$R = \left| \frac{1 - n_z}{1 + n_z} \right|^2 \;,\; T = \frac{4 n_z'}{|1 + n_z|^2} \tag{2.204}$$

As required for neutron conservation

$$R + T = 1 \tag{2.205}$$

To calculate the transmission through a plane slab the geometry in Fig. 2.3 is changed, so that the medium ends on a plane boundary at $z = d$. If it is assumed, that the angle of incident ϕ is sufficiently large, reflection can be neglected. The new geometry is shown in Fig. 2.4. The wave function in this case is given by

$$\psi(\mathbf{r}) = \begin{cases} a e^{i\mathbf{k}\cdot\mathbf{r}} & z < 0 \\ A e^{i\mathbf{K}\cdot\mathbf{r}} & 0 < z < d \\ a' e^{i\mathbf{k'}\cdot\mathbf{r}} & d < z \end{cases} \tag{2.206}$$
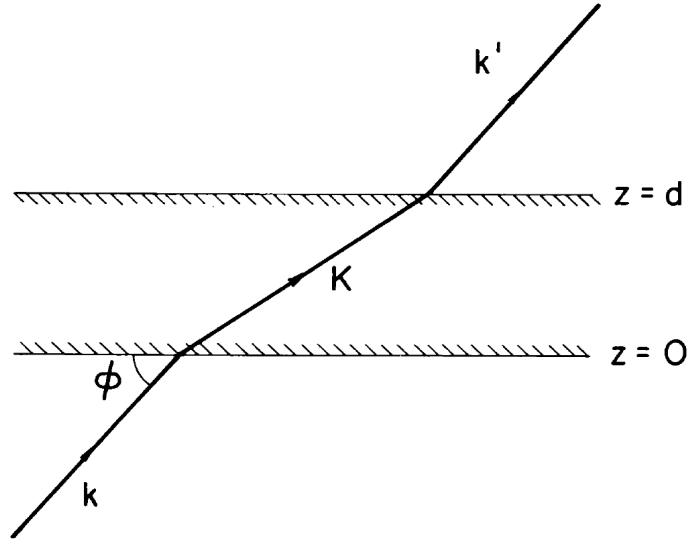
Figure 2.4.: Transmission through a plane slab, [6] p.66

That continuity of $\boldsymbol{\nabla}\psi(\mathbf{r})$ is not given, since reflection is neglected. Nevertheless the continuity of $\phi(\mathbf{r})$ is still valid. Therefrom follows

$$\begin{aligned}\mathbf{k}' = \mathbf{k} &= (k\cos\phi, 0, k\sin\phi)\\ \mathbf{K} &= (k\cos\phi, 0, n_z k\sin\phi)\end{aligned}$$

(2.207)

as well as

$$\begin{aligned}a' &= ae^{i\chi}\\ A &= a\end{aligned}$$

(2.208)

where χ is given by

$$\chi = (n_z - 1)kd\sin\phi$$

(2.209)

The assumption of a small ξ and the corresponding expansion of Eqn. 2.178 lead to

$$\begin{aligned}n &= 1 - \frac{\xi}{2}\\ n_z &= 1 - \frac{\xi}{2\sin^2\phi}\end{aligned}$$

(2.210)

consequently,

$$\chi = (n-1)kD = -\frac{1}{2}\xi kD$$

(2.211)

where D is the effective length of the neutron trajectory in the medium

$$D = \frac{d}{\sin\phi}$$

(2.212)

For $\phi = \pi/2$, i.e. normal incidence, where $D = d$ and $n_z = n$, the relation $\xi = (n-1)kD$ is exact. In this geometry the transmissivity T is defined as the fraction of incident neutrons that are transmitted by the slab

$$T = \frac{j'_z}{j_z} = \left|\frac{a'}{a}\right|^2 = \left|e^{i\chi}\right|^2$$

(2.213)

Using a complex χ, so that $\chi = \chi' + i\chi''$ follows

$$T = e^{-2\chi''}$$

(2.214)

with help of Eqn. 2.211 it can also be written as

$$T = e^{-\mu D} \tag{2.215}$$

where

$$\mu = 2kn'' \tag{2.216}$$

or by using Eqn. 2.179 as

$$T = e^{-N\frac{4\pi}{k}b''D} = e^{-N\sigma_a D} \tag{2.217}$$

This equation finally gives a correlation between a measurable value and the quantity σ_a respectively b''. T can be obtained from a intensity, respectively a count-rate measurement, comparing the value after transmission through a sample with them without sample, so that

$$T = \frac{I}{I_0} \tag{2.218}$$

Knowing the material constants N, the geometrical constant D and the neutron wave vector $\mathbf{k}$ the absorption cross section σ_a and therewith the imaginary part of the scattering length b'' can be calculated.

2.4. Ultra-cold and very-cold neutrons

Neutrons usually are categorized according their energy or in related terms like their velocity, wavelength or temperature. In the most cases the different neutron classes are associated with a corresponding moderation technique, for example neutrons in thermal equilibrium with a room temperature moderator are called thermal neutrons or cold neutrons are associated with a cold moderator like liquid deuterium at $T \approx 25$ K. However, the boundaries between the groups are quite arbitrary and vary in the literature. One possible categorization is presented in Tab. 2.2. In

	E [eV]	v [m/s]
ultra-cold neutrons	$<2 \cdot 10^{-7}$	<6
very cold neutrons	$2 \cdot 10^{-7} - 5 \cdot 10^{-5}$	$6 - 100$
cold neutrons	$5 \cdot 10^{-5} - 25 \cdot 10^{-3}$	$100 - 2000$
thermal neutrons	$25 \cdot 10^{-3}$	2200
epithermal neutrons	$25 \cdot 10^{-3} - 5 \cdot 10^5$	$2200 - 10^7$
fast neutrons	$> 5 \cdot 10^5$	$> 10^7$

Table 2.2.: Neutron categorization according their energy

the experiments discussed later only neutrons of the first two categories, ultra cold neutrons and very cold neutrons (VCN), are used.

The most evident property of UCN, what also gives reason to the categorization of this group, is, that their energy is in the region of the optical potential of the most material. In terms of velocity this means that their velocity is lower than the critical velocity for total reflection at any angel v_c, see Eqn. 2.183. As consequence of this property it is possible to store UCNs in material cavities, so-called neutron bottles. Such stored neutrons allow a variety of measurements which are not, or only conditionally, possible with a neutron beam. Experiments with "bottled" neutrons are for example the measurement of the free neutron lifetime [8–10]. In [10] it is demonstrated that the neutron

confinement can not only be done by material walls but also by a magnetic field. Another typical experiment for "bottled" neutrons is the measurement of the neutron electric dipole moment [11]. Calculating a corresponding temperature T to the energy of an UCN with

$$E = \frac{3}{2} k_B T \qquad (2.219)$$

where it is assumed that the neutrons can be treated as a ideal gas, a value of $T \approx 1.5$ mK is obtained. Considering this value it is obvious that production of UCN by conventional moderation in not feasible. A practical way is the use of a super-thermal process [12] or a neutron turbine [13]. Since all experiments presented in this work were performed at the ultra-cold and very-cold neutron facility PF2 of the ILL in Grenoble (France) only the second approach is discussed here. At this
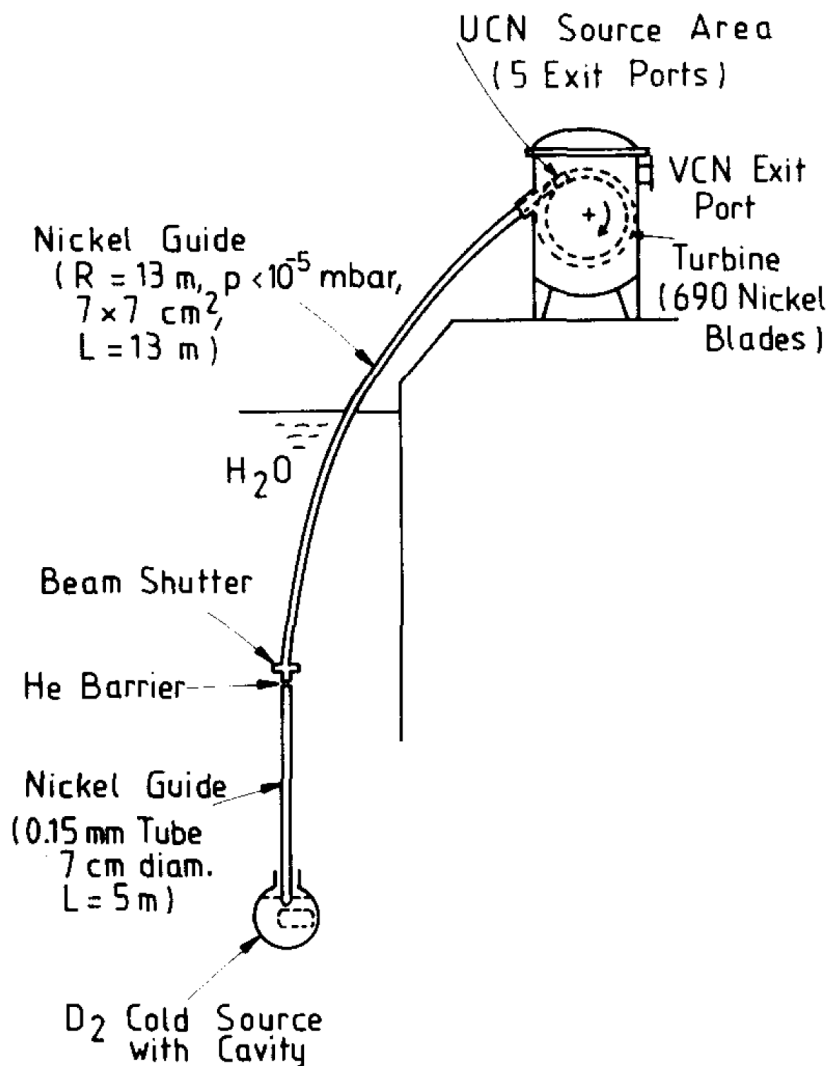
Figure 2.5.: Scheme of the UCN/VCN turbine source, [13] p.348

facility UCN are produced by extracting neutrons from a D_2-source by a vertical neutron guide. The cold neutrons lose part of their energy by rising in the gravitational field of the Earth. The upper part of the neutron guide is curved with the purpose, that neutrons their velocity is to high to fulfill the condition for total reflection at the guide walls, are separated from those which fulfill the condition. When the neutrons reach the upper end of the guide, 17 m above the source, their

energy is already in the VCN regime. Actually a fraction of the beam is bypassed at the following turbine and is directly guided to the VCN beam port.

The remaining neutrons are guided to the turbine, where they are reflected by a set of curved turbine blades, shown in Fig. 2.6. If a neutron strikes a turbine blade with the velocity v, while
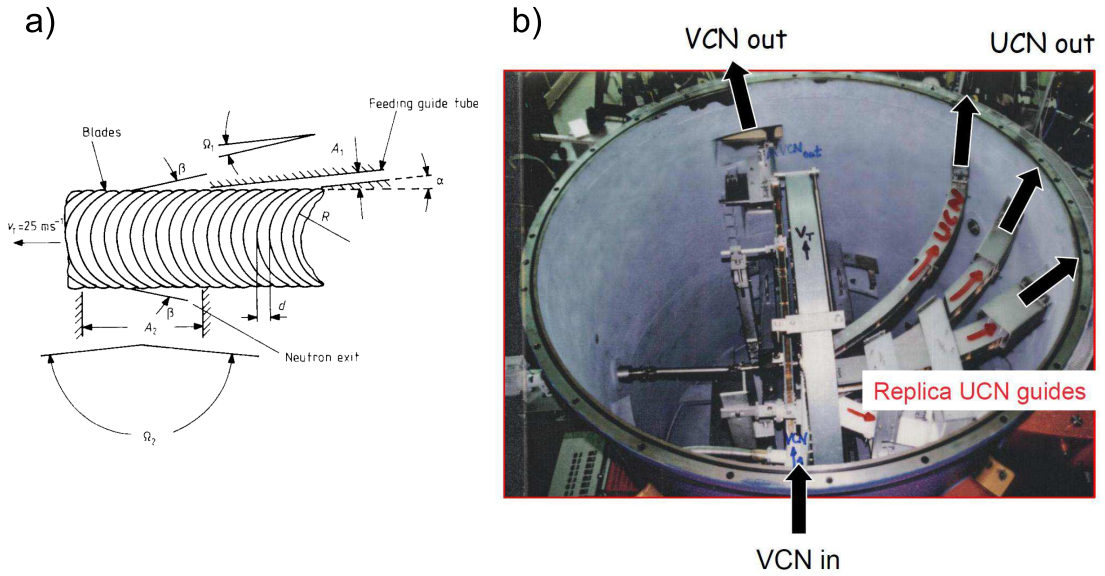
Figure 2.6.: a) Principle of the neutron turbine, [5] p.57, b) turbine with lid removed [14] p.11

the blade is moving with the velocity V in the same direction, the neutrons velocity expressed in system of the blade is $v - V$ before the collision and $V - v$ after the collision. Converted in to the laboratory system the reflected neutrons velocity is $2V - v$ [5]. In practice the turbine rotates with a frequency of 3.8 Hz what results with a diameter of 1.7 m in a peripheral velocity of $V = 20$ m/s. The velocity of the neutrons in forward direction is after passing the turbine in the region of 10 m/s. Measured spectra are shown in Fig. 2.7
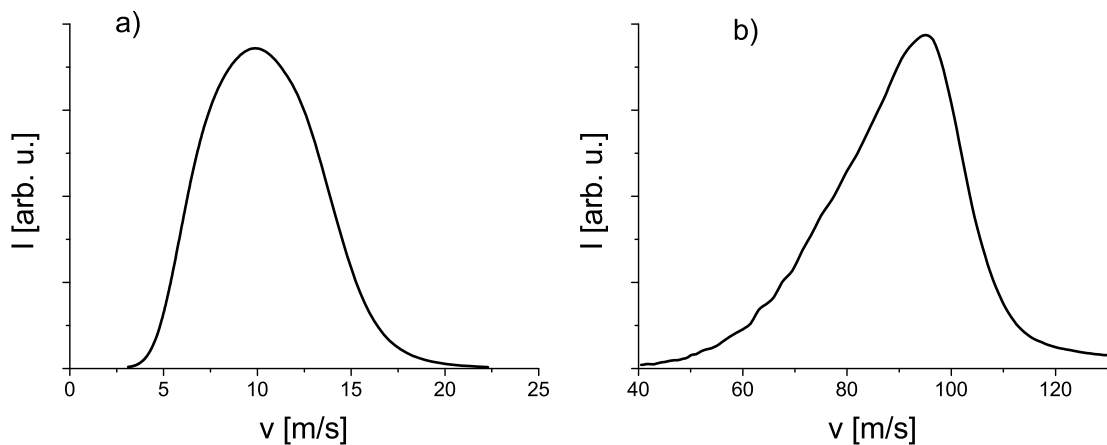
Figure 2.7.: Measured velocity spectra of the a) PF2 TES beam port and b) PF2 VCN beam port

3. Giant absorption cross section and check of the 1/v-law

3. Giant absorption cross section and check of the 1/v-law

3.1. Introduction

As described in the previous section the neutron absorption cross section can be approximated, away from resonance phenomena, in the first order by a 1/k respectively a 1/v-dependency [6]:

$$\sigma_a = \frac{4\pi}{k}b_c'' = \frac{4\pi\hbar}{vm_n}b_c'', \qquad (3.1)$$

where b" is the imaginary part of the scattering length an m_n is the neutron mass. To achieve an as large as possible absorption cross section and the associated giant absorption this dependency can be used. By using the slowest available neutrons the absorption cross section is increasing correspondingly. Measuring an as high as possible absorption cross section and testing if the 1/v-dependency is valid even for neutrons with velocities tending to 0 m/s is one of the goals of the present work.

A first experimental approach to the topic is presented in [15]. The measurement of the velocity dependent absorption cross section is reported. The authors used as absorber materials gold, aluminum and copper and additional measurements with glass, mica and air are presented. For the examined velocity region, the lower limit was in all cases at 5 m/s. The authors found the expected 1/v proportionality, see Fig. 3.1. The absorption cross sections are calculated form the attenuation
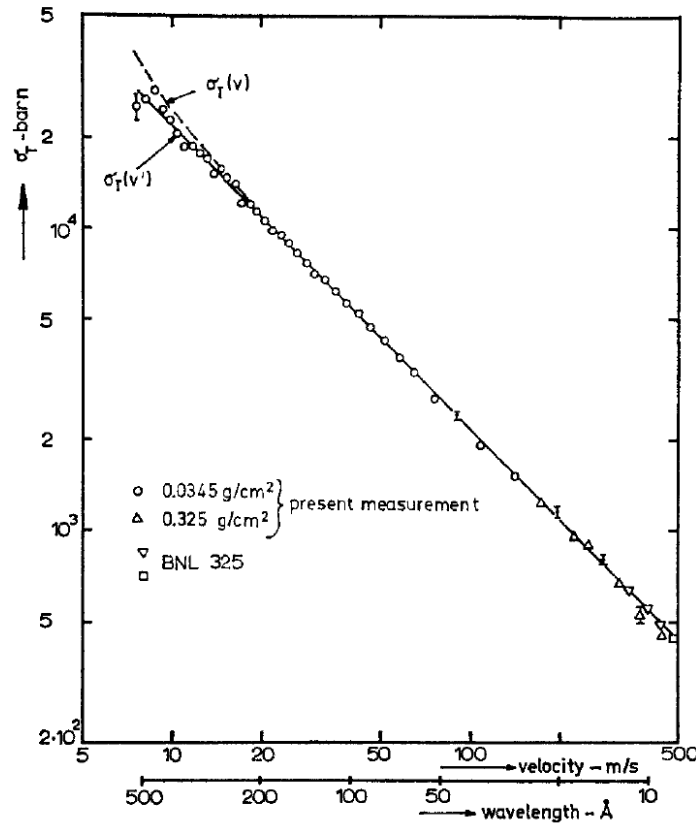
Figure 3.1.: Total cross section of two gold foils versus neutron velocity in vacuum (v) and inside the sample(v'); at temperatures 80 and 299 K. [15] p.171

of the neutron beam when transmitting through the sample. To achieve a velocity resolution a time-of-flight system was used.

Similar measurements for varies materials are reported in [5,16–19]. In all this publications the 1/v behavior was confirmed.

In [1] a measurement with a modified concept is presented. The authors measured the neutron absorption cross section of natural Gd and isotopic pure ^{157}Gd in the region from 2 to 14 m/s. To achieve a still measurable neutron flux for the strongly absorbing material, the Gd is dissolved and hereby diluted in heavy water, D_2O. The absorption cross section of the Gd is calculated by comparing the transmission values with them of a control sample consisting of pure D_2O. Using a diluted sample has the advance, that the neutrons are decelerated in the potential of the solvent. The neutron optical potential of D_2O has a value of 166 neV, which corresponds to the kinetic energy the neutron are losing. With this concept lower neutron velocities are realized than in the measurements mentioned before. To receive a velocity resolution also here a time of flight setup is used. Several aspects of the setup and its features are discussed below, because in the present work a similar, partly improved, setup up was used. In Fig. 3.2 the results found in [1] are shown. The
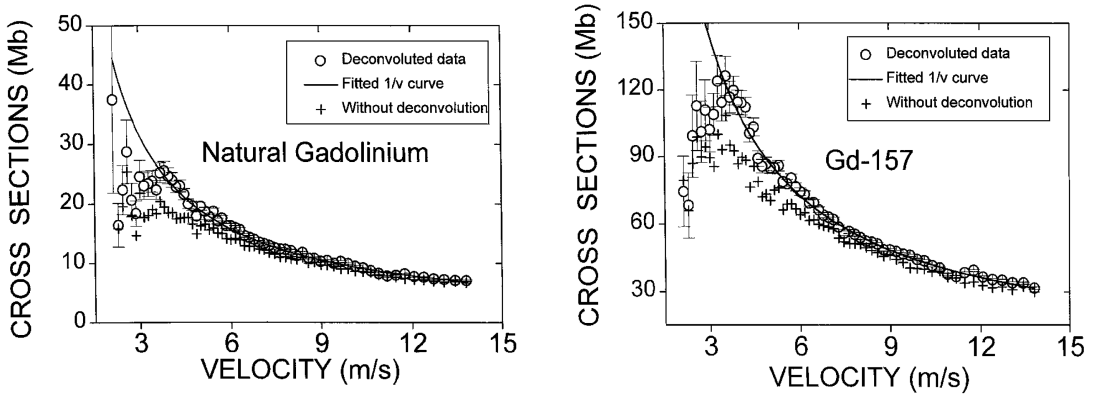
Figure 3.2.: Velocity dependence of measured ultra-cold neutron absorption cross section of Gd and ^{157}Gd. [1] p.4958

data points show a deviation from the 1/v-law in the region below 5 m/s. This unexpected results gave reason for a closer look of their origin and for the reinvestigation. According the authors a possible explanation of this effect can be found by considering the influence of fluctuation of the experimental parameters. The transmission coefficient $\alpha = \exp[-\sigma_a ND]$ with $\sigma_a = \sigma_{a,m} v_m/v$ is influenced by the velocity spread δv around the mean velocity v_m, the thickness variation δD and the particle density fluctuation δN in respect to the mean values:

$$\bar{\alpha} = \alpha_m \exp[(\sigma_{a,m} N_m \delta D)^2/2 + (\sigma_{a,m} D_m \delta N)^2/2 + (\sigma_{a,m} N_m D_m)^2(\delta v/v_m)/2] \qquad (3.2)$$

where

$$\alpha_m = \exp[-\sigma_{a,m} N_m D_m] \qquad (3.3)$$

the quantities with subscript m refer to the mean values.

Particular attention is paid to the particle density fluctuation of the absorbers within the coherence volume respectively the coherence tube of the neutron beam. Because of the low concentration of the Gd-atoms dissolved in the heavy water the fluctuation $\delta N_{coh}/N_{coh}$ is estimated with values up to 20%, what leads to a correction of the absorption cross section of 6%. In the replying articles [20] and [21] the role of the coherence volume respectively the correlation length is discussed controversially.

An other explanation for the deviation of the measured values form the 1/v-law is presented in [22]. The authors of this theoretical paper calculate the interaction in the quantum-mechanical system composed by projectile neutrons and target nuclei, starting with the wave function of the system

3. Giant absorption cross section and check of the 1/v-law

expanded in a series of eigenfunctions

$$\Psi(t) = A_{n_{\mathbf{p}}}(t)\phi_{\mathbf{p}}\Phi_N + \sum_{i=1}^{N} C_{\mathbf{p}}^i(t)\Phi_N^* + \sum_{\mathbf{p}'} B_{\mathbf{p},\mathbf{p}'}\phi_{\mathbf{p}'}\Phi_N + \sum_{k} B_{\mathbf{p},k}(t)\Phi_N|1\mathbf{k}> \qquad (3.4)$$

$A_{n_p}(t)$ is the amplitude of the state in which the target nuclei are in the ground state Φ_N and the incident neutron flow has its initial distribution $\phi_{\mathbf{p}}$. $C_p^i(t)$ is the amplitude of the state in which a target nucleus is excited and a neutron from the initial distribution with momentum $\mathbf{p}$ is absorbed. In the sate described by the amplitude $B_{\mathbf{p},\mathbf{p}'}$ the target nucleus is in the ground state, a neutron with momentum $\mathbf{p}$ is absorbed from the initial state and a neutron with momentum $\mathbf{p}'$ is emitted. In the last state with the amplitude $B_{\mathbf{p},k}(t)$ a neutron with momentum $\mathbf{p}$ is absorbed from the initial distribution and a γ quantum with momentum $\mathbf{k}$ is emitted.

Ad the end of the calculus the authors achieve a term for the absorption cross section, defined by two cases: the first case shows the already known proportionality

$$\sigma_a \propto \frac{1}{v} \qquad (3.5)$$

In contrast the second case provide a proportionality to the neutron velocity:

$$\sigma_a \propto v \qquad (3.6)$$

The transition between the two cases happens at 4 - 5 m/s, which is in good agreement with the experimental results describe in [1].

However in [23] the authors came to the conclusion, that the result found in [22] concerns only the effective cross section for a nucleus occurring in a dense medium and not for a single nucleus or for an absorber dissolved in a solvent at low concentration, what is the case in [1].

In [24] a different behavior of the absorption cross section is predicted. A saturation value is expected. This prediction is based on the approximation, that for media with large absorption cross section the imaginary part of the interaction potential is dominant and the real part can therefore be neglected. For ^{157}Gd the authors calculate about 77 Mb as saturation value. But experimental data found in [1] contradict this hypothesis, values significant higher then 77 Mb were measured.

A method to prove the validity of the 1/v-law without measuring the absolute value of the absorption cross section is presented in [25]. The authors show the independence of the transmission through an absorbing film from the neutron velocity component parallel to the sample surface. Therewith they confirm the dispersion law with the form

$$k^2 = k_0^2 - 4\pi\rho b_c \qquad (3.7)$$

where k_0 ans k are the wave numbers in vacuum respectively in the medium and b_c is the complex bound coherent scattering length. The wave vector component parallel to the interface $k_{0||}$ remains unchanged at refraction, what is a general property of waves of any nature. Subtracting the quantity $k_{||}^2 = k_{0||}^2$ from both sides of the dispersion equation

$$k_\perp^2 = k_{0\perp}^2 - \xi_0^2 \qquad (3.8)$$

is obtained, with $\xi = 4\pi\rho b$. If the dispersion shows a behavior dependent on a additional term $\epsilon(k_0^2)$ to so that

$$k^2 = k_0^2 - \xi_0^2 + \epsilon(k_0^2) \qquad (3.9)$$

respectively

$$k_\perp^2 = k_{0\perp}^2 - \xi_0^2 + \epsilon(k_0^2) \qquad (3.10)$$

this term would contribute to a violation of the 1/v-law. The dispersion law is tested by measuring the transmission of neutrons, previously monochromatized by an interference filter, through a rotating disk. On the surface of the silicon disks a thin gadolinium film with a thickens of 250 Å was deposed. Changing of the rotational frequency of the disk leads to a change of $k_{||}$. After pass-
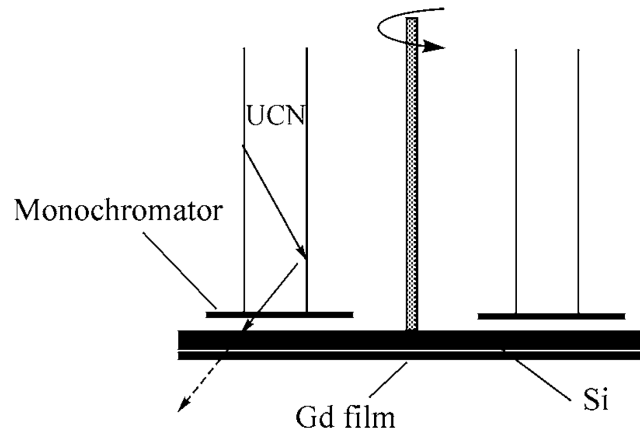
Figure 3.3.: Idea of the experiment. [25] p.106

ing the absorber disk, the neutrons are analyzed in a second interference filter. A change in the transmission depending from rotational frequency would indicate the existence of an $\epsilon(k_0^2)$ term. The authors came the result, that the transmission $\Delta T/T$ is constant with an accuracy of $5 \cdot 10^{-3}$ when the neutron velocity parallel to the absorber surface varies from 6 to 35 m/s and that the 1/v-law is valid with the same accuracy.

In a similar experiment [26] the dispersion law is checked without an absorber. The energy depen-
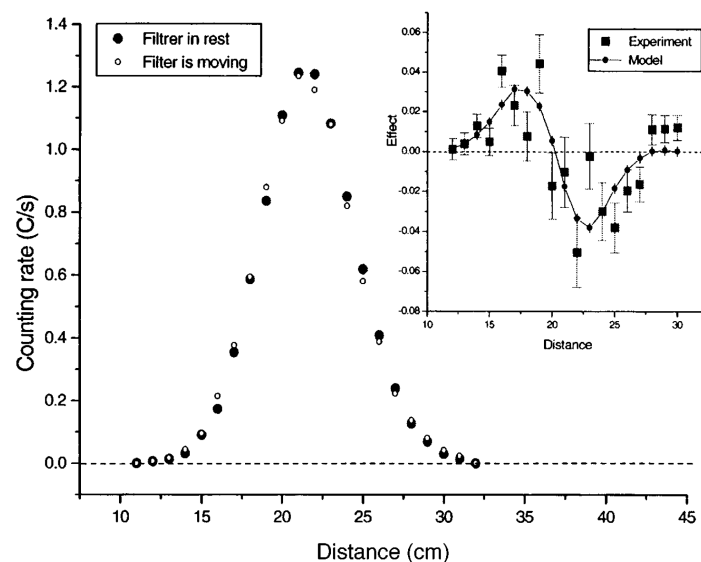
Figure 3.4.: Normalized scan curves. The errors are not indicated because when plotted they are less than the size of a dot. Insert: Differential effect, the difference of the scan curves [26] p.791

dent transmission through a interference filter is measured with a second filter used as analyzer.

3. Giant absorption cross section and check of the 1/v-law

The first filter is mounted on a motor, so that the filter can rotate around the vertical axis. The maximum of the neutron energy spectrum passing the filter is at 107 neV. The second filters maximum is at 127 neV. Taking into account the change of the neutron energy in Earth's gravitational field, the transmission spectra of both filters are matching, if they are mounted in a vertical distance of approximately 20 cm. Varying this distance provides a scan of the transmission as a function of the energy. The check of the dispersion law is done by comparing such scans with standing and spinning motor. The authors observed a shift of the transmission spectra with spinning motor of $\Delta E = 0.100 \pm 0.016$ neV. This can be interpreted as a deviation from the potential like dispersion law, what implies a violation of the 1/v-law for the absorption cross section.

For further development in the controversial debate about the behavior of the neutron absorption cross section in the low velocity region new experimental data are required. Therefore new experiments were performed, which are presented in the present work.

3.2. Time-of-flight method

3.2.1. Concept of the experiment

The measurements described in the following section were also published in [27]. They can be considered as a continuation of the experiments done in [1]. The concept of the experiment stays the same but several aspects of the setup were improved.

The aim of the experiment is to measure the velocity dependent absorption cross section of a sample in the velocity region below 10 m/s. As sample gadolinium dissolved in heavy water D_2O is chosen. The reason therefore is that D_2O provides a liquid matrix in which an absorber material can be dissolved with a low absorption and incoherent scattering cross section and simultaneously a high scattering length density respectively a high neutron optical potential. Gadolinium is the stable element with the highest neutron absorption cross section: the thermal absorption cross section for Gd, with its natural isotopic abundance, $\sigma_a = 49700$ b, for isotopic pure ^{157}Gd $\sigma_a = 259000$ b [28]. This enables the smallest amount of absorbent material to be brought into solution whilst maintaining ideal proportions for the transmission coefficient. The low concentration of the absorber in the D_2O-matrix does not noticeable change the real part of the scattering length density in the transmission sample. Entering into the potential of the D_2O the neutrons lose a part of their kinetic energy, decelerating this way. The velocity inside the sample is given according to Eqn. 2.200 by

$$v = nv_0 = \sqrt{v_0{}^2 - v_c{}^2} \qquad (3.11)$$

with

$$v_c{}^2 = \frac{4\pi\hbar^2 N b_c}{m_n^2} \qquad (3.12)$$

where n is the refraction index, v_0 the velocity outside the potential, N the particle density, b_c bound coherent scattering length and m_n the mass of the neutron.

By decelerating the neutrons in the sample it is possible to achieve lower velocities, than actually present in the neutron source's spectrum. The liquid solution is brought into the neutron beam within a glass cell.
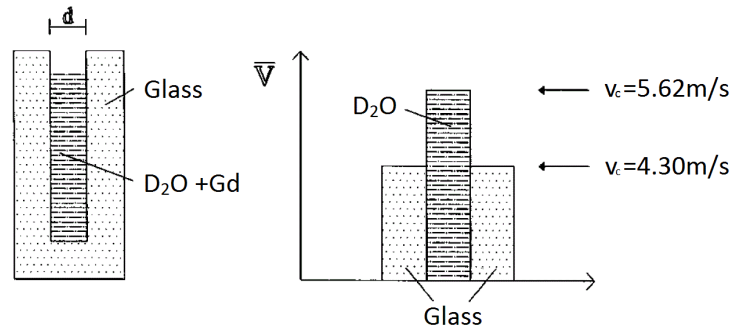
Figure 3.5.: Geometrical form and neutron optical wall potential of the described transmission samples.

In Fig. 3.5 the potential for a neutron crossing the sample is shown. To determine the absorption cross section of the gadolinium a second identical sample without dissolved gadolinium is used. By

comparing the transmission through both samples the absorption cross section σ_a can be calculated as:

$$T = e^{-Nd\sigma_a} \rightarrow \sigma_a = -\ln \frac{T}{Nd} \tag{3.13}$$

where T is the transmission, N the particle density and d the thickness of the absorber. To calculate the transmission and the related absorptions cross section as a function of the velocity, the sample is installed within a time-of-flight setup. The relation between the count rate for the samples with and without Gadolinium leads directly to the transmission.

An aspect that thereby must be considered is the angular distribution of the neutron velocity The ultra-cold neutrons, used for this experiment, show a broad angular distribution, which can be described by approximation with a cosine distribution [5]. The effective flightpath of the neutrons within the sample increases depending from the entrance angle α:

$$D_{\text{eff}} = \frac{D}{\cos \alpha} \tag{3.14}$$
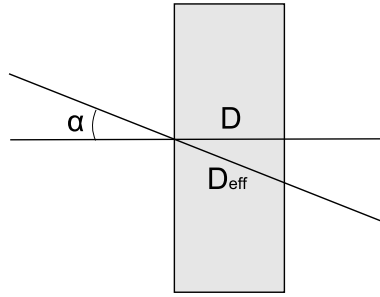
Figure 3.6.: Effective flight path of a neutron in the sample.

In the time-of-flight-setup only the component in flightpath direction of the velocity spectrum v_z can be measured. If the 1/v-law is valid the cross section can defined as a function of v_z and α.

$$\sigma_a \propto \sigma_0 \frac{v_0}{v} = \frac{\sigma_0 v_0 \cos \alpha}{v_z} = \sigma_0 \frac{\cos \alpha}{v_z} \tag{3.15}$$

inserting Eqn. 3.14 and Eqn. 3.15 into Eqn. 3.13:

$$T = \exp\left(-N\sigma_a D\right) = \exp\left(-N\sigma_0 v_0 \frac{\cos \alpha}{v_z} \frac{D}{\cos \alpha}\right) = \exp\left(-\frac{\sigma_0 v_0 N D}{v_z}\right) \tag{3.16}$$

The calculation shows that under assumption of the validity of the 1/v-law the transmission depends only on the velocity component in forward direction.

3.2.2. Experimental setup

All measurements presented in the following section were performed at the PF2 instrument at the ILL Grenoble (France), either on the UCN-beam port or on the TES-beam port.

Installed on the UCN-beam port the setup was mounted 60 cm higher than the existing turbine exit. This way the neutron spectrum is shifted to slower velocities. Installed on the TES-beam port it was mounted on the high of the turbine exit. In both cases the neutrons were delivered form the turbine exit to the setup by steal tube neutron guides. The first component of the time-of-flight-setup is the chopper [29] as indicated in Fig. 3.7. Contrary to the chopper used in the preceding experiments not a rotating-disk-chopper, but a linear-chopper is used. This type of chopper is
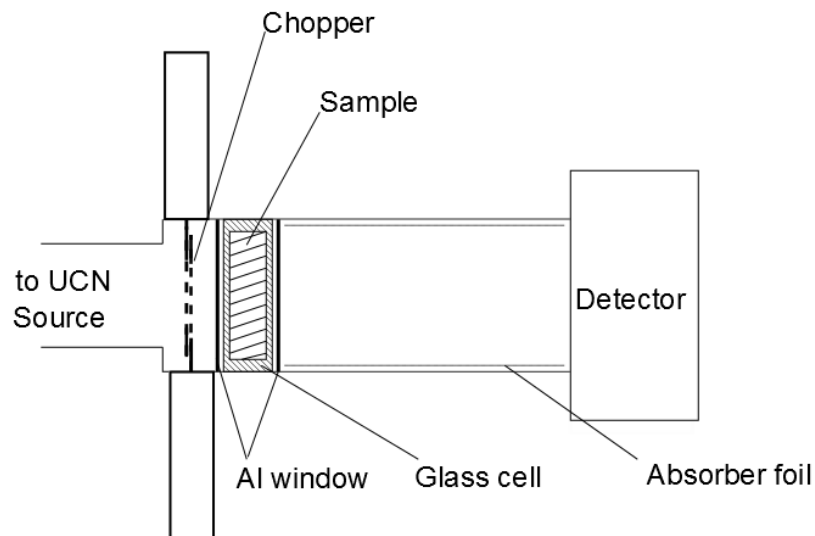
Figure 3.7.: Sketch of the time of flight setup

composed by two linear motors, which are moving two titanium grids against each other. In the starting position the grids are closed and overlap thereby 1 mm. In this position the beam is closed, thus no neutron can pass through. In the end position both grids are shifted by 2 mm, so that the slits overlap and 60% of the beam cross section is passable. A linear chopper has the advantage of an adjustable opening time and repetition frequency. This allows to optimize the open to close ratio adapted to the geometric properties of the flight path, what increases the number of usable neutrons. In contrast a rotating-disk-chopper has a fixed open to close ratio given by the aperture angel of transmission slits in the disks. For its best performance the chopper is set to a 7 ms open time with a repetition rate of 10 Hz. The corresponding opening function, measured with light, is shown in Fig. 3.8. The chopper setup is a well characterized system, the variation of the open function is less than 1%. The properties of the chopper are discussed in more detail in appendix A. Integrated into the stainless steel chopper housing a cell holder for the mentioned heavy water
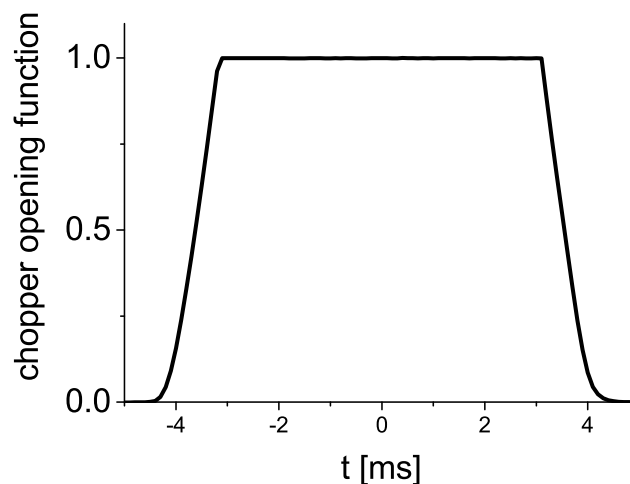
Figure 3.8.: Measured opening function of the used linear chopper

samples starts the flight path. At the first attempt of measurement the position of the cell and the chopper was inverted and as chopper grid material polyethylene was used. Changing the order of the elements in the beam and the grid material significantly reduced the background counting rate. Fig. 3.9 shows the therewith improved peak-background ratio. The origin of the background reduction lies in avoiding up-scattering of UCN to thermal velocities. Inelastic neutron scattering respectively up-scattering is practicable way to remove ultra-cold neutrons form the beam. The neutrons are scattered to higher energies and a random directions, this way they can most likely exit the experimental setup. Since the chopper and the glass cell, the origins of the up-scattered neutrons, in this setup are very close to the detector, the probability of their detection is still high enough to produce significant background. If the cell is installed behind the chopper, it is only exposed
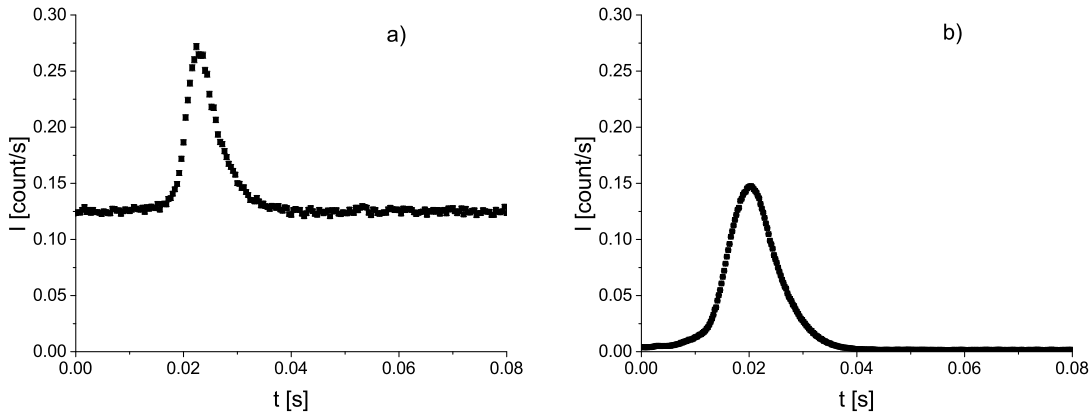
Figure 3.9.: Measured time of flight spectra: a) cell in front of polyethylene chopper, b) cell behind titanium chopper

to neutrons during the chopper opening time. This leads to a reduced and temporally structured up-scattering signal, which can distinguished clearly from the ultra-cold neutron spectrum.

The vacuum of the chopper, the feeding UCN guide and the flight path is separated from the glass cell using two 0.2 mm thick AlMg3 foils. Keeping the sample at atmospheric pressure has the advantage, that it can be changed easily without breaking vacuum.

On the back side of the glass cell 0.5 mm thick cadmium stripes serve as an aperture. Neutrons which pass the cell only partly or neutrons which are reflected on the cell holder are filtered out this way.

The glass cell itself is composed of three layers of sodium-glass glued together with ultraviolet curing glue. A cavity in the center layer forms the filling volume of the cell. The internal dimensions of the cell are $60 \times 90 \times 1.02 \pm 0.003$ mm^3. Since only the thickness of the cavity is important for the later calculation of the absorption cross section only for this value an error was calculated form measurements done during the production of the cells.

The thickness of the outer glass plates is 0.9 mm.

The flight path, a stainless steel tube with a diameter of 100 mm and a length of 218 mm is installed on the backside of the cell holder. Including the cell holder respectively the chopper housing the total effective flight path has a length of 263 mm. A picture of the setup is shown in Fig. 3.10.

The maximal time a neutron needs to cross the flight path is given by the minimal to expect neutron velocity, i.e. v_{c,D_2O}. Hence, the maximal time is in the range of 50 ms. Consquently, frame overlaps of the time-of-flight measurements can be excluded at a chopper frequency of 10 Hz.

A polyethylene foil, placed on the inside of the flight-path-tube acts as collimation, removing all otherwise reflected UCN. The negative neutron optical potential of the PE foil and its high
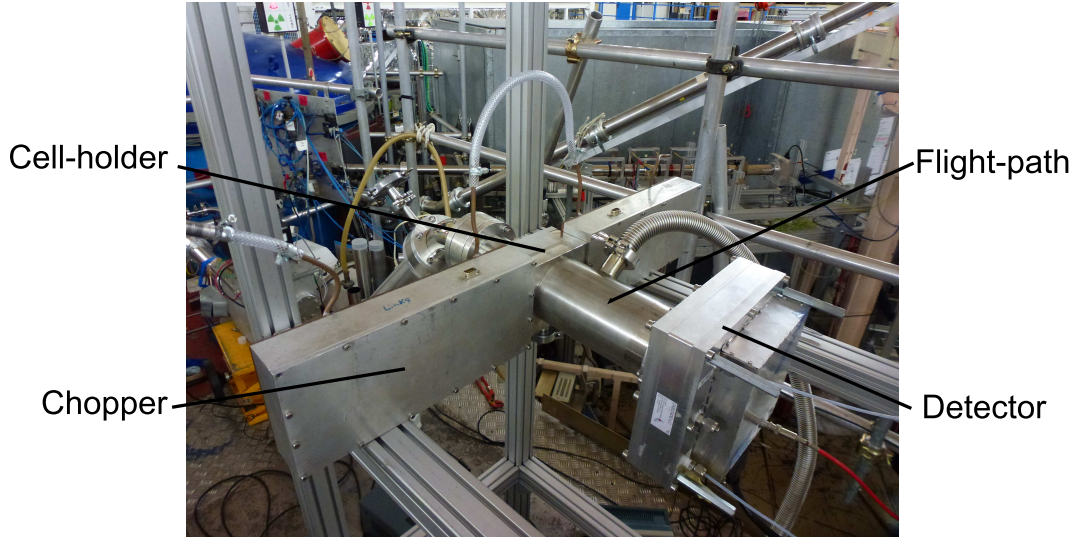
Figure 3.10.: Time-of-flight setup

incoherent scattering cross section scatters neutrons hitting the foil to thermal velocities. In this way they can exit the experimental setup. Therefore diffusive scattering, falsifying the time-of-flight spectrum, can be suppressed. This effect was investigated in an separate measurement, performed with and without the polyethylene foil. The spectra of the neutron passing through the with D_2O filled cell were observed. The results diagrammed in Fig. 3.11 show a relatively increased number of neutron at the slow velocity side of the spectrum, caused by diffuse scattering in case the foil is not used. The foil is an important improvement relating to [1]. Avoiding reflection gives also reason to choose a short flight path. This way as many as possible neutrons can pass the tube, without getting in contact with the confinement. The other parameter which determines the length of the flight path is the time resolution given by:

$$\frac{\Delta t}{t} = t_{open}/\bar{t}_{flight} = \frac{t_{open}\bar{v}}{l} \tag{3.17}$$

where t_{open} is the opening time of the chopper, $\bar{t}_{flight}$ the mean time of flight in the region of interest, $\bar{v}$ the corresponding velocity and l the length of the flight path. For the critical velocity of D_2O $v_{c,D_2O} = 5.62$ m/s, the given opening time and length, the time resolution is in the range of 10%.

The flight path follows a CASCADE U-100 [30] detector.

The transmission experiment was performed with four different gadolinium solutions, varying the particle density and the isotopic distribution. The measured Gd solutions were natural gadolinium with a particle density of $6.66 \cdot 10^{23}$ m^{-3} respectively $4.04 \cdot 10^{23}$ m^{-3} and isotopic pure ^{157}Gd with a particle density of $1.4 \cdot 10^{23}$ m^{-3} respectively $1.39 \cdot 10^{23}$ m^{-3}. The sequence of the different measurements is shown in Fig. 3.16.

The densities are chosen to fulfill the optimal transmission for a absorption cross section measurement. Inserting the definition of the transmission $T = \frac{I}{I_0}$ into Eqn. 3.13, where I and I_0 are the measured intensities with and without absorber and calculating the uncertainty results

$$\frac{\Delta \sigma}{\sigma} = \sqrt{\left(\frac{1}{\ln \frac{I_0}{i}} \frac{\Delta I}{I}\right)^2 + \left(\frac{1}{\ln \frac{I_0}{I}} \frac{\Delta I_0}{I_0}\right)^2} \tag{3.18}$$

3. Giant absorption cross section and check of the 1/v-law
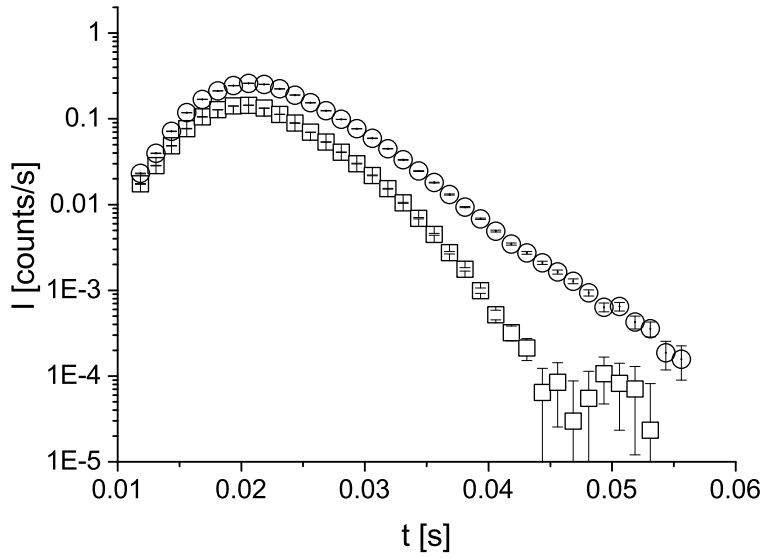
Figure 3.11.: Time-of-flight spectra measured for pure D_2O with polyethylene foil $\bigcirc$ in the flight path and without $\square$.

using $\Delta I_0 = \sqrt{I_0}$ what arises from Poison statistics

$$\frac{\Delta \sigma}{\sigma} = \sqrt{\left(\frac{1}{T} + 1 \right) \frac{1}{I_0 (\ln T)^2}} \tag{3.19}$$

is achieved. This expression has a minimum for $T = 0.109$. According to Eqn. 3.13, Eqn. 3.1 and the b_c'' values listed in [7], $b_c''(^{\mathrm{nat}}\mathrm{Gd})=13.6$ fm and $b_c''(^{157}\mathrm{Gd})=47$ fm, the condition for a optimized transmission measurement through the $^{\mathrm{nat}}\mathrm{Gd}$ solvent with the concentration $6.66 \cdot 10^{23}$ m^{-3} are given at a velocity in the range of 3 m/s. For the three other samples the transmission is optimized at a velocity in the range of 2 m/s.

The preparation of the solution is a two step process. In the first step a macroscopic amount of Gd_2O_3 with a mass in the region of 100 mg is prepared and weighed. After the determination of the exact weight the powder is dissolved in D_2O. The liquids volume is specified by a filling a beaker with a high precision pipette. In order to dissolve gadolinium in heavy water an acidic environment is required. For this reason a small amount of DCl is added to the D_2O. Also the DCl is filled in with the high precision pipette. Contemporary the mass of all components of the solvent is measured with a high precision balance. To achieve the desired Gd concentration a minor quantity of the primary solution is diluted in additional D_2O in the corresponding ratio. The final DCl concentration is below 200 ppm. Like all other measurements corresponding to the preparation of the Gd solutions the contamination by DCl is negligible small for the further data analysis.

All D_2O for the solution process as well as for the reference measurements was taken from the same batch of D_2O, which has a purity of 99.98%
. The major part of the impurities are given by H_2O. To prevent further the contamination with H_2O form the atmosphere the bottle containing the D_2O was opened the first time for the production of the solution and re-closed immediately after extracting a part of the liquid.

The share of H_2O causes inelastic scattering of the neutrons. Since the amount of H_2O in the control measurement and in the Gd-solution is the same it does not affect the measurement of the

absorption cross section, but it reduces the number of the transmitted neutrons.

3.2.3. Experimental results and analysis

With respect to the user structure of the UCN turbine each time-of-flight measurement consist of several consecutive time-of-flight data files. The PF2 UCN platform is able to serve four experiments with UCN. While a continues UCN beam with low intensity can be used at the TES beam, three UCN beam ports, Mambo, UCN and EDM, share UCNs periodically via a mechanical UCN switch. The maximal available measurement time at these beam ports is around 200 s. All single spectra recorded at the UCN beam port were measured for 130 s. Due to lack of this user structure at the TES beam total measuring time of the single data files has been set to 10 min.

The detector dwell time for a single time bin was set to 250 μs for all measurements. The result-
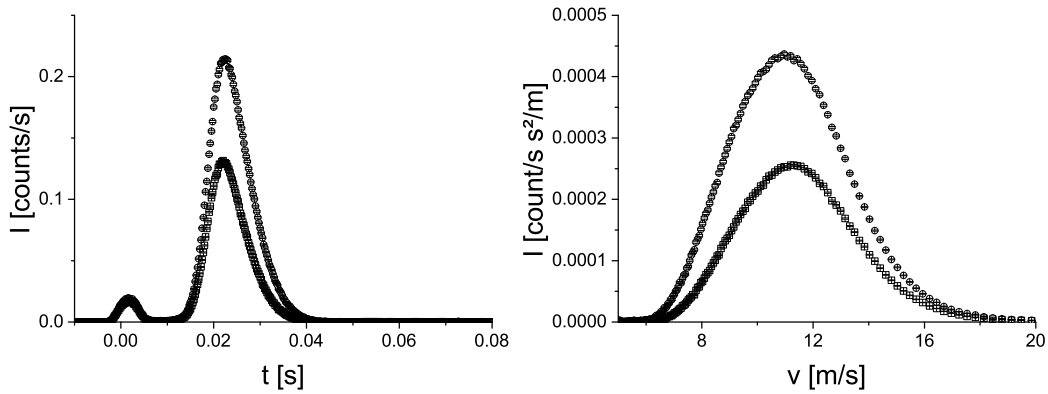
Figure 3.12.: Time-of-flight spectra measured for pure D_2O $\bigcirc$ and Gd-solution $\square$ normalized to their total measurement time.

ing spectra as a function of time of flight and neutron velocity are shown in Fig. 3.12. By the transformation from time of flight into velocity it must be considered that

$$dt = \frac{t^2}{l} dv \tag{3.20}$$

where l denotes the length of the flightpath.

The peak in the region around 0 s is caused by UCNs up-scattered in the heavy water sample and therefore moving with thermal velocities through the flight path. The background arising from a thermal neutron background in the reactor environment can be extracted from the time-of-flight spectra itself. After subtracting this constant background from the spectra the comparison of the counts for a single time bin for measurements with gadolinium solution and pure D_2O leads to the velocity dependent transmission.

Finally the absorption cross section as a function of the neutron velocity, presented in Fig. 3.13, can be extracted by applying three important corrections:

- **Position of the sample behind the chopper**
  The time of flight is changed because the neutrons are decelerated in the potential of the sample. The total measured time of flight can be divided in to multiple section, corresponding

3. Giant absorption cross section and check of the 1/v-law
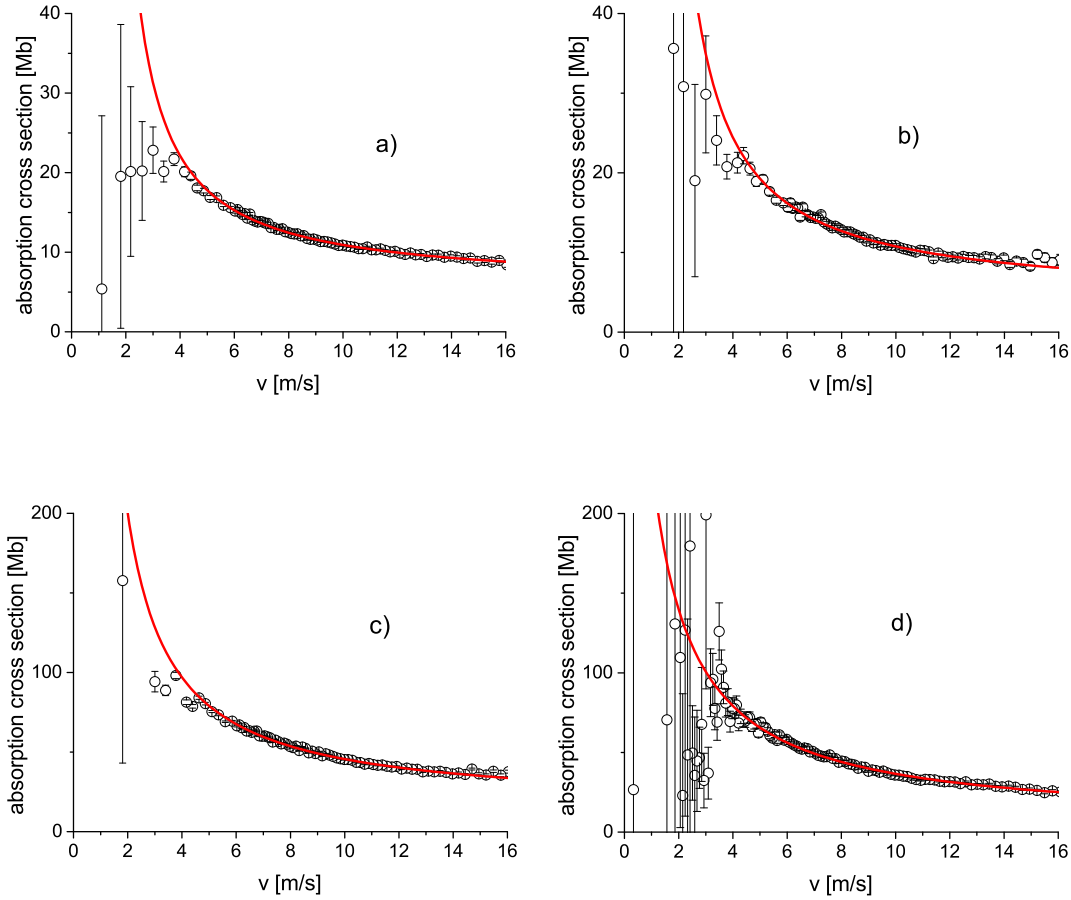
Figure 3.13.: Absorption cross section as function of the velocity;
line: 1/v-law, a) ^{nat}Gd $6.66 \cdot 10^{23}$m^{-3}, b)^{nat}Gd $4.04 \cdot 10^{23}$m^{-3}, c) ^{157}Gd $1.40 \cdot 10^{23}$m^{-3}, d) ^{157}Gd $1.39 \cdot 10^{23}$ m^{-3}

to the different media in the flight path with their different neutron velocities according to Eqn. 3.11:

$$t_{measured} = 2 \cdot t_{Cell} + t_{D_2O} + t_{reFP} = 2 \cdot \frac{d_{Cell}}{v_{SiO_2}} + \frac{d_{D_2O}}{v_{D_2O}} + \frac{d_{FP} - d_{D_2O} - 2 \cdot d_{Cell}}{v_{vac}} \quad (3.21)$$

where the index FP refers to the total flight path and $reFP$ to the reduced flight path. The corrected time, the neutron would need to cross the flight path without passing the cell, is calculated by solving Eqn. 3.21 on $t_{corr} = \frac{d_{FP}}{v_{vac}}$ and inserting Eqn. 3.11 and the different neutron scattering lengths for the corresponding materials. Fig. 3.14 shows the numerical achieved solution.

- **Multiple reflection**
  Neutrons can be reflected on the transition of D$_2$O to the glass cell. This leads to multiple crossing of the sample. Considering this effect, the transmission coefficient is given as

$$\tau = \frac{\alpha T^2}{1 - \alpha^2 R^2} \quad (3.22)$$

with $\alpha = e^{-N\sigma_t d}$, $T = \frac{4v_0 Re(v')}{|v_0 + v'|^2}$ and $R = |\frac{v_0 - v'}{v_0 + v'}|^2$ where T is the transmissivity and R the reflectivity of the D$_2$O surface [31]. Both values depend on the UCN velocity outside
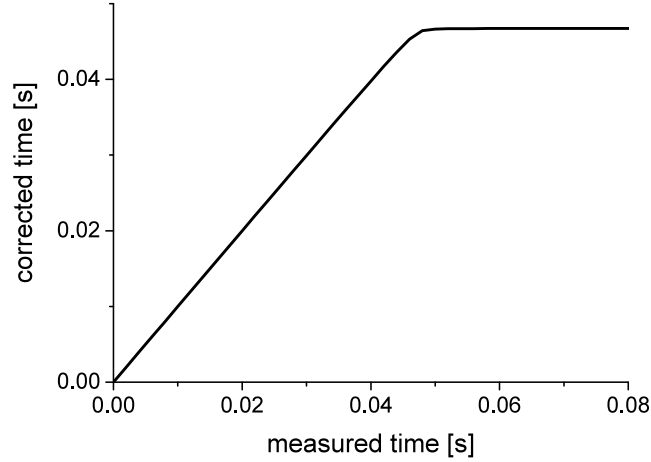
Figure 3.14.: Correlation of the measured time of flight and the theoretical without sample

the sample, v_0 and on the, in general complex, velocity v' inside the sample. σ_t is the sum of the inelastic and incoherent scattering cross section, which is dominated in this case by the absorption. The latter is dominating in the present case. Without multiple crossings the transmission coefficient would reduce to α as expected.

- **Deceleration of the neutrons within the potential**
  The UCN velocity within the potential of the D_2O is calculated according Eqn. 3.11.

Applying this corrections to the acquired data the values plotted in Fig. 3.13 are achieved. The error bars are calculated according the law of error propagation [32]

$$\sigma_y^2 = \sum_i \left[\frac{dy}{dx_i}\right]^2 \sigma_1^2 \tag{3.23}$$

while the initial error of a single intensity measurement is given by the Poison statistics. An additional correction that can be done is the deconvolution of the spectra. Every measured time of flight spectra represents a convolution of the effective time of flight and the opening function of the chopper. The here used deconvolution algorithm is discussed in appendix B. The algorithm produces an additional uncertainty, because it includes fitting a continuous function to the measured vales. If the time resolution of the setup, given by the ratio of the chopper opening time t_{open} to the time of flight t_{flight}

$$\frac{\Delta t}{t} = \frac{t_{open}}{t_{flight}} \tag{3.24}$$

is small enough the uncertainty given by the convolution is smaller than that produced by the deconvolution algorithm. Applying the deconvolution algorithm to the spectra the absorption cross sections in Fig. 3.15 are calculated. The deconvolved data show a decreasing tendency of the absorption cross section for velocities below 3 m/s. But taking the size of the error bar into account, this effect is not conclusive. More like it is a result of the higher count-rate in the D_2O measurement, what leads to a better determination of the background count-rate level compared to the Gd measurements.

The results of the measurements performed at the UCN beam, Fig. 3.13 a)-c), provide no absolute value for the absorption cross section within acceptable error limits, because the total count rate for the single 130 s spectra is fluctuating, as shown in Fig. 3.16. This fluctuation produces an additional Gaussian type error for the calculation of the absolute value, calculated as the
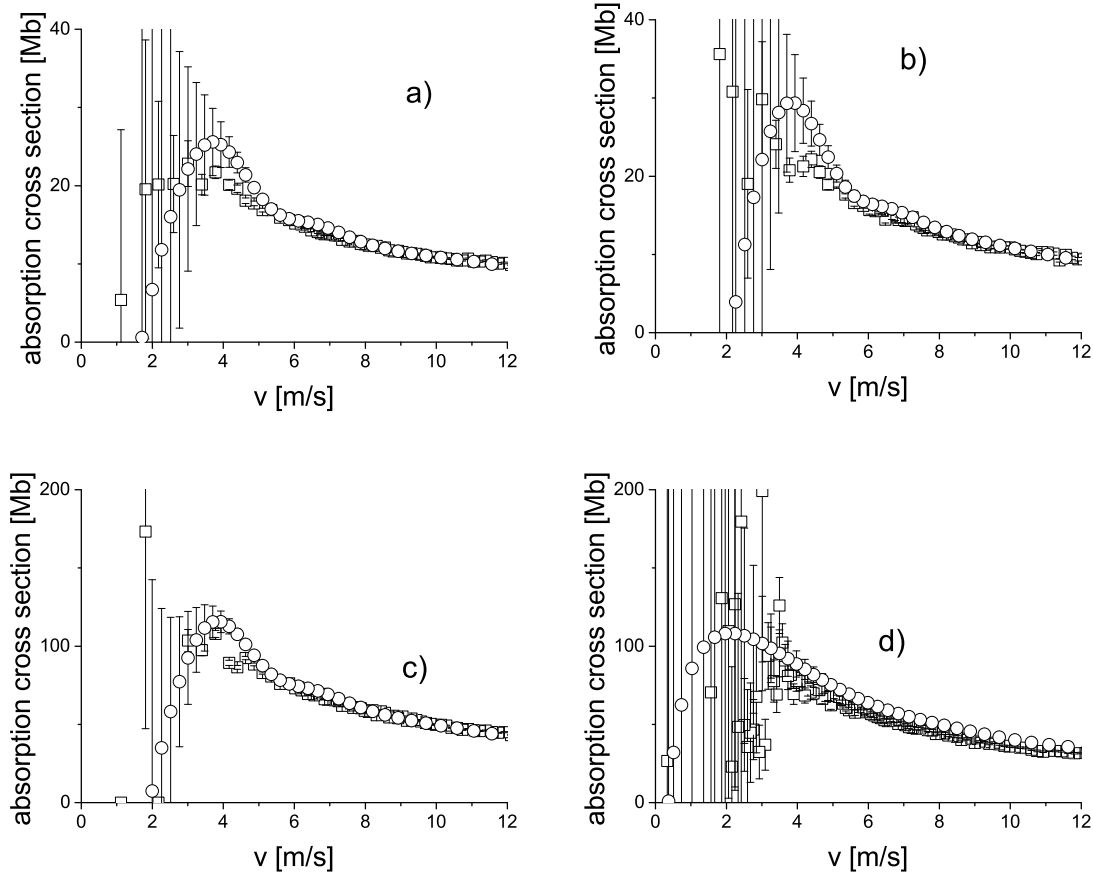
Figure 3.15.: Absorption cross section as function of the velocity: a) ^{nat}Gd $6.66 \cdot 10^{23}$ m^{-3}, b) ^{nat}Gd $4.04 \cdot 10^{23}$ m^{-3}, c) ^{157}Gd $1.40 \cdot 10^{23}$ m^{-3}, d) ^{157}Gd $1.39 \cdot 10^{23}$ m^{-3}, □ not deconvolved data ◯ deconvolved data

standard deviation of the single measurement total count-rate. In Tab. 3.1 absolute values and error limits for the different performed measurements are listed. Hereby the error limits are distinguished in the Gaussian error and the Poison error given by the total counts of a single measurement. Both measurements, performed on different beam, provide matching results and Poison type errors in the same region. But in contrast to the TES beam measurement, the UCN beam measurement shows very large Gaussian type errors, with relative errors up to 46.1%. Nevertheless the dependence of the absorption cross section form the velocity can be calculated. The results shown in Fig. 3.13 a) - c) do not include the additional error caused by the fluctuation. The measurement performed at the TES beam port does not show a significant fluctuation of the count-rate. For that reason the absolute value of the cross section can be calculated and are within acceptable error limits, shown in Fig. 3.13 d).

To evaluate the behavior of the absorption cross section the measured data can be fitted with different functions, like the 1/v function, or modified versions which reach a saturation value or, like proposed in [22], a function combined by a part proportional to 1/v and the other proportional to v. To compare the different models the reduced χ^2 values and the corresponding p values can be used. In Tab. 3.2 this values are listed for the mentioned fit models.

The imaginary part of the bound coherent scattering length b_c'' can be extracted according

3 m/s							
	N	beam port	$\sigma[Mb]$	$\Delta\sigma_P[Mb]$	$\Delta\sigma_P/\sigma[\%]$	$\Delta\sigma_G[Mb]$	$\Delta\sigma_G/\sigma[\%]$
^{nat}Gd	6.66	UCN	17.28	2.91	16.9	3.3	19.1
^{nat}Gd	4.04	UCN	29.5	7.33	15.8	5.81	19.7
^{157}Gd	1.40	UCN	96.70	18.85	19.5	21.98	22.7
^{157}Gd	1.39	TES	102.54	20.27	19.8	2.82	2.7
5 m/s							
^{nat}Gd	6.66	UCN	11.33	0.24	2.1	3.30	29.1
^{nat}Gd	4.04	UCN	18.85	0.54	2.9	5.82	30.9
^{157}Gd	1.40	UCN	77.87	1.50	1.9	21.98	28.2
^{157}Gd	1.39	TES	73.17	1.60	2.2	2.82	3.8
10 m/s							
^{nat}Gd	6.66	UCN	5.36	0.09	1.74	3.30	61.6
^{nat}Gd	4.04	UCN	10.58	0.21	2.0	5.82	55
^{157}Gd	1.40	UCN	47.69	0.52	1.1	21.98	46.1
^{157}Gd	1.39	TES	40.64	0.49	1.2	2.82	6.9

Table 3.1.: Measured absorption cross section of the four different gadolinium solutions with Poison type error $\Delta\sigma_P$ and Gaussian type $\Delta\sigma_G$.

to Eqn. 3.1 from the fit-function. Its value calculated based on the measurement presented in Fig. 3.13 d) and the corresponding 1/v-fit-curve is 41.7 ± 2.5 fm.

fitting function	v_0 [m/s]	χ^2	p value
$\sigma_a \propto \frac{1}{v}$		1.78	$1.3 \cdot 10^{-6}$
$\sigma_a \propto \frac{1}{v}, v > v_0$	5	1.57	$1.9 \cdot 10^{-4}$
	4	1.37	$9.5 \cdot 10^{-3}$
$\sigma_a \propto \text{const}, v < v_0$	3	1.67	$2.2 \cdot 10^{-5}$
	4.46	1.35	$1.5 \cdot 10^{-2}$
$\sigma_a \propto \frac{1}{v}, v > v_0$	5	3.6	$2.4 \cdot 10^{-24}$
	4	1.32	$2.0 \cdot 10^{-2}$
$\sigma_a \propto v, v < v_0$	3	1.58	$1.5 \cdot 10^{-4}$
	3.66	1.27	$4.8 \cdot 10^{-2}$

Table 3.2.: Reduced χ^2 and p values (117 degrees of freedom) for different fitting models. 4.46 m/s and 3.66 m/s are the optimized velocities for the corresponding fitting model.

3.2.4. Conclusion

In a series of experiments the neutron absorption cross section for Gd was measured. The results show values, depending from the velocity, up to 100 Mb. Additional the 1/v-law has been examined. Contrary to [1], no significant violation in the region above 3 m/s is visible . An explanation therefore is the improved experimental setup in particular the polyethylene absorber foil. This foil eliminates non angular reflected neutrons. The falsification of the spectrum due to these neutrons is shown in Fig. 3.11 for a flight path of 263 mm. A longer flight path, as used in the previous experiments, influences the results even stronger. More specifically it leads to an overrating of the neutron transmission in the falling flanks of the spectrum.

Fitting models for the measured data beside the 1/v-law provide slightly better reduced χ^2 values, but not to an extant for the proof of a significant violation of the 1/v-law. The missing statistic in the velocity region below 3 m/s inhibits the further extrapolation of the absorption cross section. This demonstrates the main problem for the measurement: two signals, both tending to zero, are compared. Although the experiment could acquire data for a long time, more than 40 days, a definitive answer to the check 1/v-law can not provide. This suggests that the possibilities of the used concept are on its limit, significant improvements on the error limits in the lower velocity range are not to expect. For further investigations another approach will be necessary.
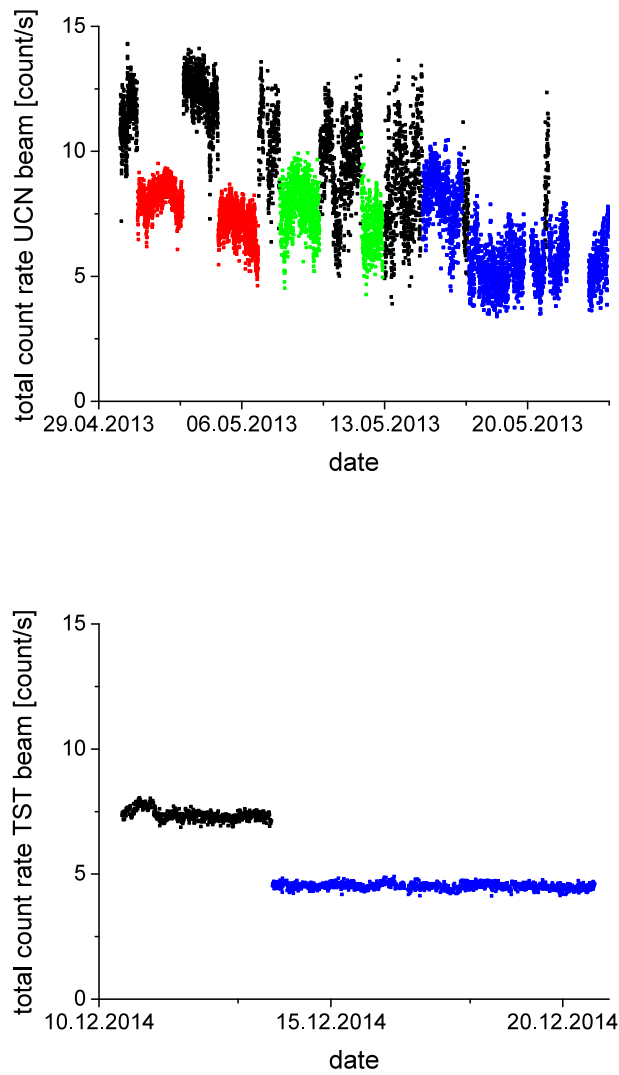
Figure 3.16.: Total count-rate for UCN beam and TES beam experiments.

UCN beam: black: pure D_2O fluctuation for the full spectrum 20%, red: ^{nat}Gd $6.66 \cdot 10^{23}$ m^{-3} fluctuation 10.3%, green: ^{nat}Gd $4.04 \cdot 10^{23}m^{-3}$ fluctuation 13.3%, blue: ^{157}Gd , $1.40 \cdot 10^{23}$ m^{-3} fluctuation 24.4%

TES beam: black: pure D_2O fluctuation 3%, blue: ^{157}Gd , $1.39 \cdot 10^{23}$ m^{-3} fluctuation 2.6%

3.3. Velocity selector method

3.3.1. An ultra-cold neutron velocity selector

As already evident in the previous section, investigation of energy or velocity dependent effects with neutrons demand correspondent preparation of the neutron beam. So far the time of flight method was used, where the neutron beam gets pulsed, which results in a time resolution. An alternative method is the reduction of the velocity spectrum to a narrow band. To achieve a velocity dependent resolution the reduced spectrum is needed to be tunable. This can be realized with a neutron velocity selector. Apparatuses like this are described in [33–37]. But none of the described velocity selectors is capable to provide a velocity spectrum in the range of 0 to 15 m/s. Therefore a new velocity selector adapted to UCN was constructed as part of this work.

To achieve a transmission spectrum with a narrow velocity range all neutrons with the "wrong" velocity have to be rejected, only the neutrons with the "right" velocity are allowed to transmit. This rejection of the neutrons is done by rotating disk of a neutron absorbing material. Windows in the disk allow the transmission of the neutrons within intended spectrum. Passes a neutron the
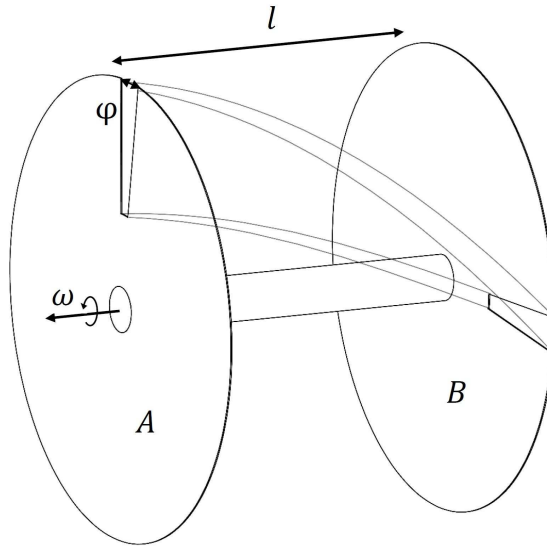
Figure 3.17.: Schematic of the working principle

window in the disk A, referring to Fig. 3.17, it can only pass the window in disk B, if it takes the same time to cover the distance l between the two disks, as the disks need to rotate over the angel ϑ, included by the two windows:

$$\frac{l}{v} = \frac{\vartheta}{\omega} \tag{3.25}$$

where v denotes the velocity of the the neutron and ω is the rotation frequency of the disks.

The transmission function is given by the geometric properties of the selector disks. The longest allowed time to pass is $t_{\max} = \frac{\vartheta+\varphi}{\omega}$, the shortest $t_{\min}\frac{\vartheta-\varphi}{\omega}$. Hence, the length of the transmission function defined by this two cases is $\Delta t = t_{\max} - t_{\min} = \frac{2\phi}{\omega}$, always assuming a parallel neutron beam, i.e. all neutron have trajectory normal to the selector disks. The resulting transmission function consequently has a triangle shape, if it is expressed as function of the time-of-flight. Expressed as a function of the neutron velocity it has the shape shown in Fig. 3.18 and the functions width
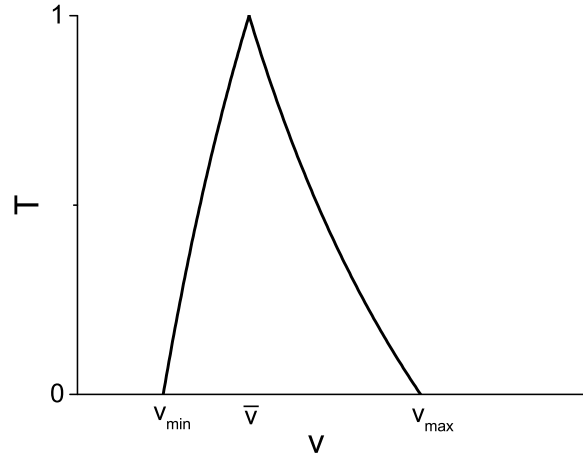
Figure 3.18.: Transmission as function of v

Δv is given in this case by

$$\Delta v = v_{\text{max}} - v_{\text{min}} = \frac{4lf\varphi\pi\bar{v}^2}{4l^2 f^2\pi^2 - \varphi^2\bar{v}^2} \tag{3.26}$$

where $\bar{v}$ is the velocity with the highest transmission value which corresponds to the mean time-of-flight, f is the rotation frequency, and φ is the opening angle of the transmission windows.

To avoid transmission of neutrons with velocity $v = \bar{v}/n$ where n is an integer number, hence transmission of higher velocity modes, additional disks can be mounted between the outer disks. The position where the disk N is mounted for this purpose must fulfill

$$l_N = \frac{l}{N^2} \tag{3.27}$$

Multiple windows on the disks increase the number of the transmitted neutrons. However the number of the windows must be chosen in a way that the neutrons have only one possibility to pass through the selector, so that they can not to pass from one window channel to an other. This would allow the passing of neutrons with a "wrong" velocity. As consequence, with the increase of the number of windows also the number of disks has to increase. For a one-slit selector with the same window opening angle ϕ as actually chosen in the finale design two additional disks would satisfy to cancel out all higher velocity modes present in the ILL-PF2-UCN-source spectrum. But to get an reasonable neutron intensity for the selector was planed with 22 slits, what increases the number of disks to eight.

3.3.2. Construction parameters

All construction parameters for the selector are adapted to a round neutron beam with 70 or 80 mm in diameter, what corresponds to the diameters of the PF2 beam ports. This size affect the radii of the absorber disks and so the rotor's mass and moment of inertia. All other construction parameters are optimized by computer simulation with two goals, on the one hand that the highest reasonable rotation frequency is applied and on the other hand that no transmission side peaks should in the spectrum. ÃŸ Test of the motor showed that due to the rotor's mass and moment of inertia as well as due its unavoidable imbalance the operating frequency should be less than

80 Hz. At its original purpose the motor operates in region between 750 and 1000 Hz.

The resulting layout of the rotor is displayed in Fig. 3.19 and Fig. 3.20.

The neutrons are guided in a distance of 150 mm from the rotation axis to the selector. This
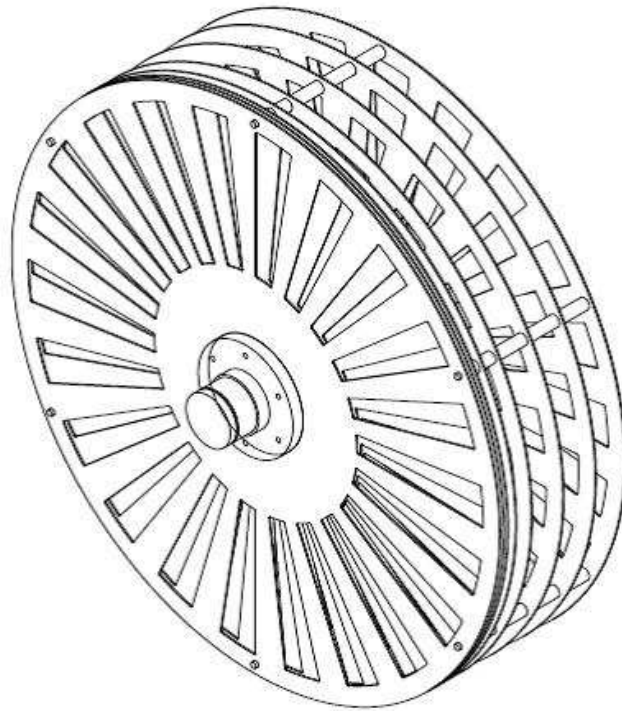
Figure 3.19.: Rotor of the selector construction drawing

distance is influenced by the beam cross section, as mentioned 70 or 80 mm and the commercial available vacuum vessels. As vacuum vessel a ISO-K 400 setup was chosen, hence the inner
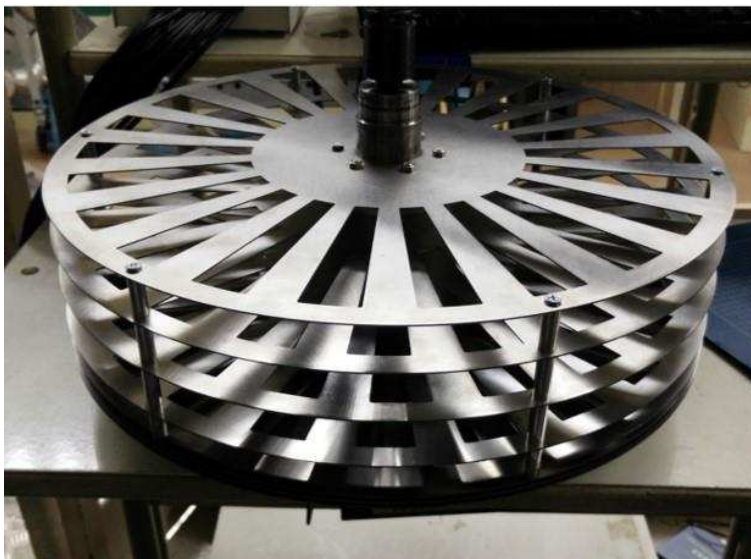
Figure 3.20.: Rotor of the selector

diameter is 400 mm. The vessel setup consists of two blank flanges and a 115 mm long tube. Into the blank flanges are cut inlets for the neutron beam as well as holes for the bearing holders. As

bearings which connect the vacuum vessel with the rotor 6007-KER-SI3N4-PEEK [38] bearings are used. These are self-lubricating ceramic grooved ball bearings. They provide the desired vacuum suitability and can resist the mechanical stress caused by the weight and the rotation of the rotor. Beside they are not vacuum suitable, normal lubricated bearings proved to have a too large resistance at the desired operational frequency. During the operation of the selector it has shown that the ceramic bearings are sensible to pollutions. They had to be changed or at least cleaned when an influence on the performance became evident. However, this became less frequently the longer to selector was operating.

The selector's rotor is build up by eight 1 mm thick titanium disks, with a diameter of 386 mm, supported by an axis made of stainless steel. The transmission probability of UCN through 1 mm titanium is in the range of $T = 5 \cdot 10^{-4}$ and can be therefore neglected. The negative scattering length of titanium b_c =-3.37 fm has the advantage, compared to material with positive scattering length, that no total reflection appears and hence, the overall reflection probability is lower.

Every disk has 22 windows, with the form of a circle sector with an included angle of $\phi = 9°$. The distances from the front side of the first disk to the following are 3 mm, 6 mm, 12.5 mm, 25 mm, 50 mm, 75.5 mm and 99 mm. The position of the disk is chosen according Eqn. 3.27. The disk at 75.5 mm corresponds to one at 0.5 mm but shifted due to lack of space to a corresponding position. So the overall length of the setup is 100 mm. The twisting of the window channels is 1800 °/m. This results in a correlation of the rotation frequency and the selected neutron velocity of $v = 0.2 \, \frac{\text{m/s}}{\text{Hz}} \cdot f$. The measured frequency-velocity relation is shown in Fig. 3.21. According to
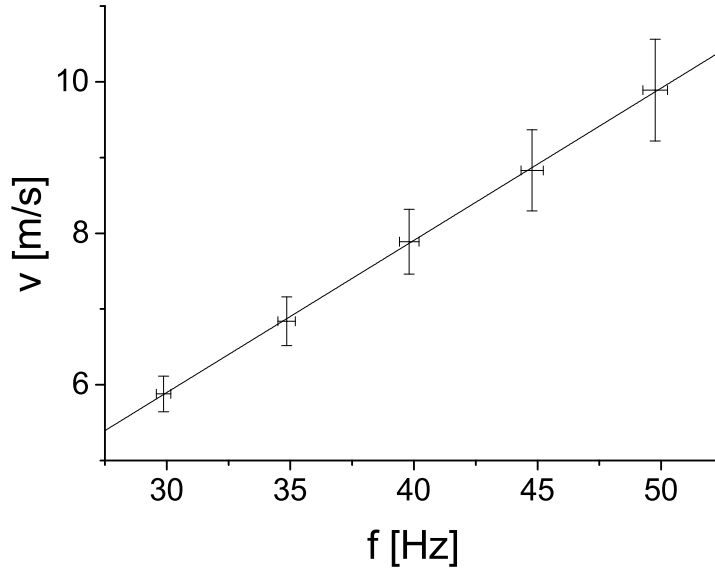
Figure 3.21.: Measured frequency-velocity relation. Error bar in f is given by the hysteresis of the two-point-control, error bar in v by the by the time resolution of the time-of-flight setup; line: expected relation

this construction parameters and Eqn. 3.26 a velocity resolution of $\frac{\Delta v}{v} = 10\%$ would be achieved for a parallel neutron beam at 50 Hz, respectively 10 m/s.

3.3.3. Drive unit and control

The selector is driven by the electric motor of a "Pfeiffer TPH170". Given that the handling of ultra-cold neutrons conditions a vacuum environment, using the motor of a turbo pump has the advantage that it can be installed directly at the vacuum vessel. The electrical feed through is hereby already integrated into the motor.

On the same axes, which supports the absorber discs, the motors armature is mounted. The axes conical shape and a screw-nut keep the armature in position and prevent it from overrunning. Hall-sensors are integrated in the motor. These allow the read out of the motor position, respectively the rotation frequency. Based on the turbo pump control "Pfeiffer TCP300" a electrical control was build, which is capable to actuate the four coil pairs of the motor and read out the operational frequency. In contrast to the original motor control with the self-made version the rotation frequency can be regulated. This is done by a two point control operating the power supply. In the first version of the control the Hall-sensor signal are read in by the data acquisition device NI USB 6009 [39] and analyzed by software based on NI LabVIEW language. The power supply is regulated by the same data acquisition device and software. In the second version an Arduino UNO [40] micro-controller board assumes this function, reducing this way software problems. In both cases the selectors frequency and the two point control hysteresis settings can be set via a software interface. In Tab. 3.3 measured values for the frequency distribution within an 1% range and an 1.5% range of the mean frequency are listed, while the hysteresis of the two-point control was set to 1% of the mean frequency. The measured values show a stable operation of the setup. The slight deviation of the

f_{mean}[Hz]	1%	1.5%
29.87	77.6%	99.1%
34.85	80.3%	99.8%
39.82	81.1%	99.9%
44.78	84.0%	99.9%
49.77	82.0%	99.1%

Table 3.3.: Measured frequency distribution within a 1% and a 1.5% range of the mean frequency

set hysteresis and the actual measured is caused by the systems inertia.

3.3.4. Characterization

For further use the actual transmission spectrum of the selector must be measured. For this purpose the velocity selector has been installed on the TES-beam of the PF2 instrument at the ILL Grenoble. A time-of-flight setup is used to determine the velocity spectra. The same linear chopper [29] as used in the previous section and a flightpath mounted on the exit of the selector build this setup. Hereby two flight paths of different length are alternately used. The first is a 218 mm long steel tube with 100 mm in diameter, with a polyethylene foil placed on the inside. The foil acts as a collimation, removing all otherwise reflected UCNs. This way diffusive scattering, which would falsify the time-of-flight spectrum, can be suppressed, as already discussed in 3.2.2. It is the same flight path assembly as used for the time-of-flight measurements in the previous section. Because of a modified chopper housing the effective flight path in this setup is 253 mm. The second flight path is an 1 m long stainless steel neutron guide, 70 mm in diameter. This longer flight path decreases according to Eqn. 3.24 the time resolution and thereby the convolution effect

of the chopper opening function and the time-of-flight spectrum. The deconvolved spectra for
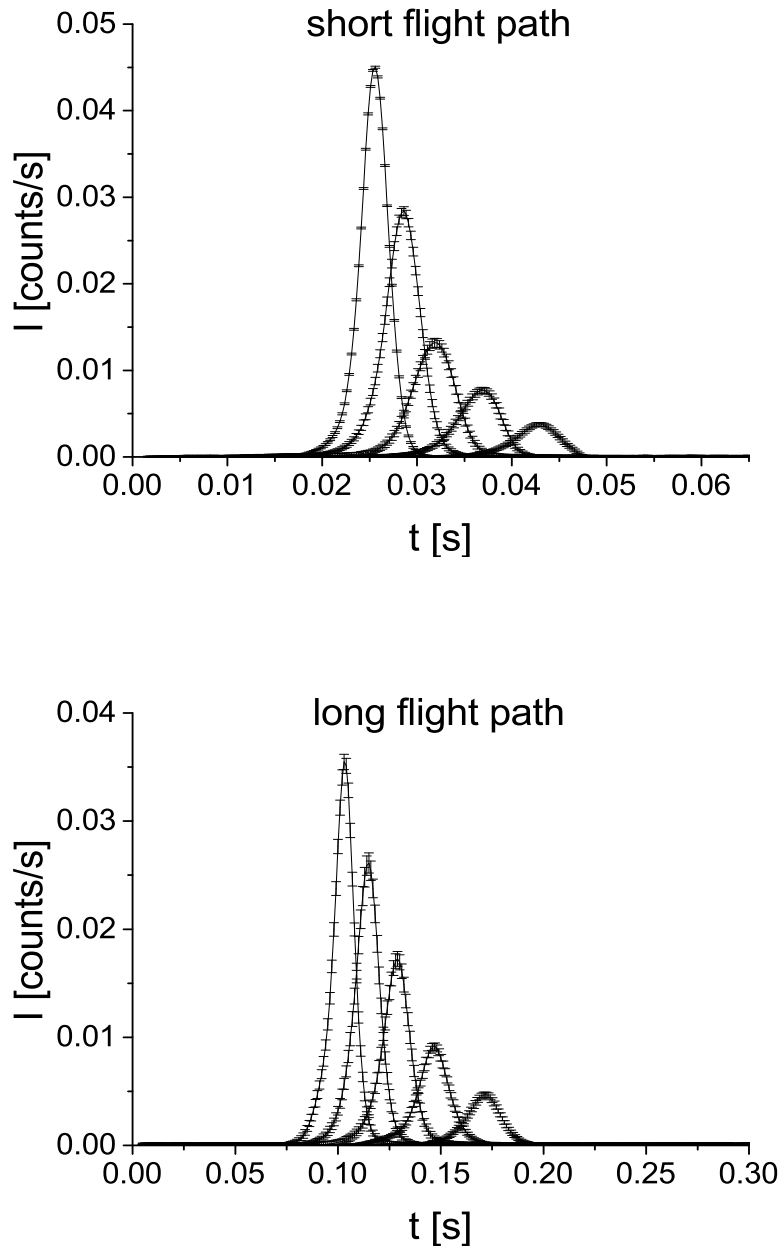
Figure 3.22.: Time-of-flight spectra for the two different flight paths with different frequency settings

both flight paths are shown in Fig. 3.22.

As detector again a Cascade U 100 [30] is used. The transmission spectra are calculated by normalizing the measured time-of-flight spectra with the unchanged spectrum. This was measured with the same setup but without selector. The velocity dependent transmission, shown in Fig. 3.23, is the result of converting time of flight into velocity. The deviation from the calculated transmission triangle function is caused by the non parallel UCN beam. The angular distribution of neutron trajectories allows neutrons with the "wrong" velocity in forward direction to pass the selector, if the transverse velocity matches with rotational motion of the selector disk. This leads to a widening of the transmission spectrum. In Tab. 3.4 the velocity resolutions for different
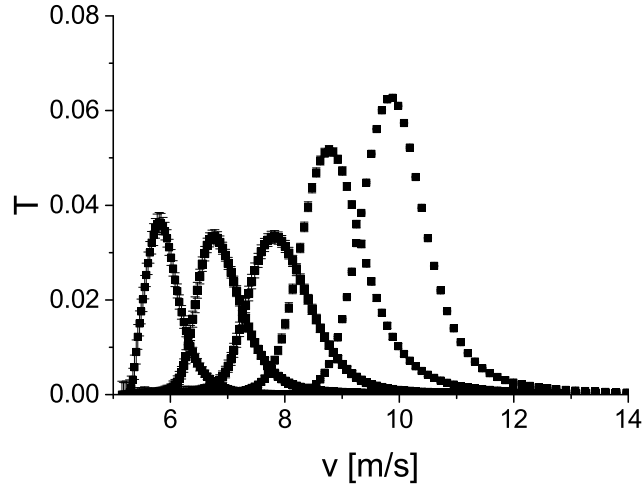
Figure 3.23.: Transmission spectra for different velocities

velocities are listed. Since the measured transmission function is not given by discrete function like the calculated function for a parallel beam, Fig. 3.18, it is not clear how to identify the velocity resolution $\frac{\Delta v}{v}$. One possible definition is the functions full width at half maximum (FWHM). An

v [m/s]	Δv [m/s]	Δv/v
5.81	0.68	0.11
6.76	0.89	0.13
7.81	1.25	0.16
8.77	1.27	0.15
9.84	1.28	0.13

Table 3.4.: Measured velocity resolution

other cause for the deviation from the transmission function in Fig. 3.18 can be found in the fact, that neutrons with the "right" velocity in forward direction can not pass the selector, if their transverse velocity is too high. Therefore the maximum of the transmission is not at the level of the primary spectrum but significantly lower in the range of 3-6%.

The higher transmission probability for neutrons faster than 8 m/s is a result of the changed angular distribution of the neutron trajectories in this velocity range. The reflection probability of the steel neutron guides decreases with increasing neutron velocities. Neutrons with a higher velocity component perpendicular to the guiding tube surface than the critical velocity for total reflection can exit the guiding system. Therefore the angular distribution is reduced to smaller angles. The angular acceptance of the selector in combination with the changes angular distribution of the neutron trajectories leads to the apparently increased efficiency for higher velocities.

3.3.5. Absorption cross section measurement

One of the possible applications the selector was build for is the measurement of velocity dependent neutron absorption cross section. The selector provides a method for this measurement alternative to the time-of-flight method. Some critical aspects appearing there can be avoided with the selector arrangement. For example non specular reflections can be neglected because of the possibility to shorten the distances between the single elements of the setup. The correction concerning the positioning of the sample mentioned in 3.2.3 is obsolete using the selector method. Other aspects like the convolution effect of the choppers opening function with the neutron spectrum appear in a similar way. Here the velocity resolution of the selector has the same effect.

To measure neutron absorption cross sections the same concepts as discussed in the time-of-flight chapter were used. As before the sample is a glass cell filled with Gd dissolved in D_2O. The used cells are build the same way as described before. A slightly change concerns the their inside dimension, in this experiment it is 1.03 mm.

In the selector arrangement the measurement also contributes from the fact, that the neutrons are decelerated according to Eqn. 3.11 in the D_2O Fermi-potential. In this manner the neutron spectrum is shifted within the sample to lower velocities. The main difference to the time of flight method is that not the hole velocity spectrum is measured at the same time, but only a narrow velocity band, which is cut out of the spectra by the velocity selector. Doing this sequentially for different velocities the velocity dependent transmission can be measured and thus also the absorption cross section. In figure Fig. 3.24 the setup of the experiment is shown. To mention is that a second
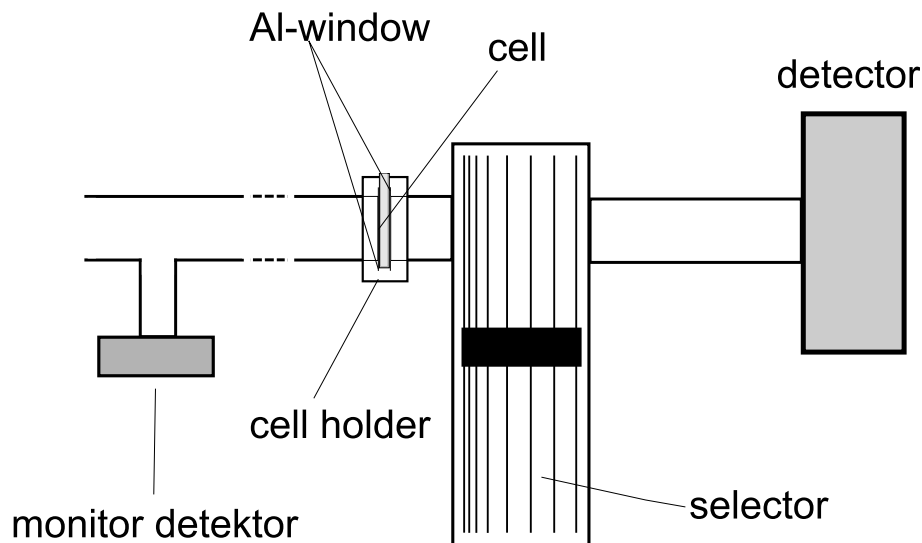
Figure 3.24.: Experimental setup for the measurement of the neutron absorption cross section with a velocity selector

detector is mounted directly below the beam port, connected with a T-piece to the beam line. Like the main detector it is a Cascade U 200. Its function is the monitoring of the incident beam intensity. Possible fluctuations can be taken into account this way. The monitor data, displayed in Fig. 3.25, show no significant fluctuation of the beam intensity. Also during this measurement the TES-beam port of the PF2 instrument provides a contestant neutron flux in contrast to the time-of-flight measurement performed at the UCN-beam port. Consequently the distribution of the measured values is only associated with their measurement uncertainty. Hence, Gauss statistics and Poisson statistics provide uncertainty values in the same range: $\frac{\Delta\sigma_G}{\sigma} = 2.38\%$, $\frac{\Delta\sigma_P}{\sigma} = 2.2\%$.

The cell holder, which contains the glass cell with the dissolved absorber, is mounted as close
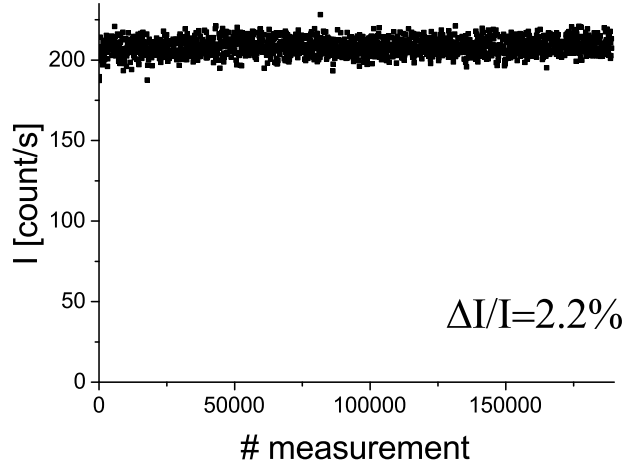
Figure 3.25.: Monitor detector count rate during the measurement. Every data point represents a 10 s measurement.

as possible in front of the velocity selector. This reduces the number of neutron reflected on the walls of the connecting neutron guide and therewith the possibility of a non specular reflection. In conjunction with the angular acceptance of the selector the effect of the falsification of spectrum discussed in 3.2.2 is thereby minimized. Reflections after the selector do not contribute to the falsification of the spectra, because their velocity is already analyzed in the selector. The better handling of this source of error is an advantage of the selector method against the time-of-flight method.

The selector provides shielding for possible thermal neutrons produced by up-scattering in the glass cell and the D_2O. Therefore the sample is mounted in front of the selector and not vice-versa. This increases also the distance between cell and detector, what additional reduces the amount of detectable thermal neutron. Their intensity decreases as an $1/r^2$-function, because of the 4π character of the inelastic scattering, which is the origin of the neutron thermalization.

Taking this facts into account a 10 cm long stainless steel neutron guide was used for the connection between the cell holder and the selector, a 40 cm long guide between selector and detector.

The transmission through the Gd and thus the absorption cross section is calculated by comparing the measured detector count-rates of a pure D_2O sample with the Gd-solution sample. The Gd-solution has been prepared the same way like discussed in section 3.2.2. The sample's Gd concentration was $6.09 \cdot 10^{23}$ m^{-3}.

Using the time of flight setup the background count-rate I_{bg} has been extracted from the measured spectra. This is not possible with the velocity selector setup. A separate measurement is needed, which is performed with stopped selector. This way for the calculation of the Gd-transmission three measured intensities has to be taken into account:

$$T = \frac{I_{Gd} - I_{bg}}{I_{D_2O} - I_{bg}} \tag{3.28}$$

To minimize the background signal the detector as well as parts of the selector are covered with a layer of Cd-metal. Nevertheless the determination of the background has proven to be the week point of the concept. One problem is that the background signal is strongly influenced by the performance of the neighboring instruments, especially by the PF2-VCN-beam port. Because of the low count-rate in the data of the background measurements, shown in Fig. 3.26, clearly two different levels can be seen. This appears also in all measurements for D_2O and Gd in the lower velocity

region. This two levels can be related to the an open respectively a closed VCN-beam. Every data point in the figure represents a 15 min measurement, what was the standard setting, during the whole data acquirement. Stopping the selector takes, depending from the initial rotation frequency,
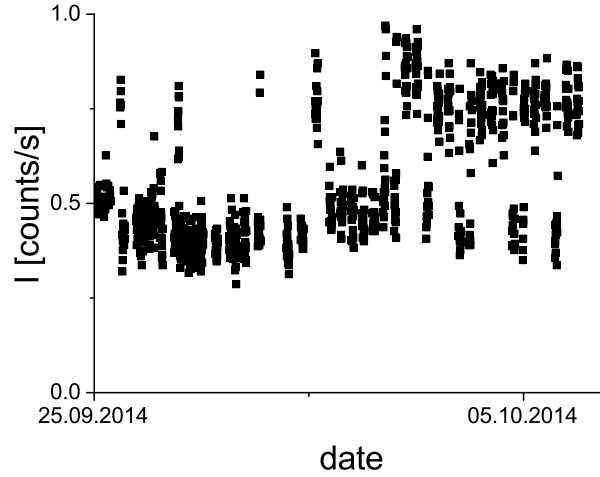
Figure 3.26.: Background intensity over time, measured with stopped selector

up to 20 min. Therefore the background measurement can not considered strictly related to the previous measurement. For the calculation of the velocity dependent absorption cross section the data is sorted into groups. Criteria for the grouping are the additional Cd shielding, that was added after concluding the first measurement cycle, and the status of the VCN-beam. This sorting leads to the set of values listed in Tab. 3.6.

The absorption cross sections are calculated by evaluating corresponding values according to Eqn. 3.28 and Eqn. 3.13. Corrections according the deceleration of the neutron in the D_2O Fermi-potential and multiple crossing of the cell because of reflections on the transition between the liquid sample and the glass cell were considered, the same effects as already discussed in 3.2.3. The results are listed in Tab. 3.5 and plotted as a function of the neutron velocity in Fig. 3.27. Because of the

v[m/s]	σ_a [Mb]	$\Delta\sigma_a$ [Mb]
1.95	1.65	30.74
2.95	-16.35	1238
2.95	9.61	29.25
3.36	8.23	20.65
3.36	24.14	38.66
3.73	12.06	15.19
3.73	20.89	24.61
4.08	18.51	11.65
4.08	23.47	10.37
5.89	13.32	1.69
8.19	9.78	0.53

Table 3.5.: Measured velocity dependent neutron absorption cross section

size if the error bars fitting a theoretical function to the data is not meaningful.

The imaginary part of the bound coherent absorption cross section b_c'' can be calculated from the

sample	VCN beam	add. Cd	f[Hz]	I[counts/s]	Δ I[count/s]
D_2O	closed	no	0	0.536	0.034
D_2O	closed	no	30	0.583	0.036
D_2O	closed	no	32	0.602	0.041
D_2O	closed	no	35	0.833	0.039
D_2O	closed	no	41	2.188	0.068
D_2O	closed	no	50	6.398	0.078
Gd	closed	no	0	0.491	0.050
Gd	closed	no	30	0.534	0.047
Gd	closed	no	32	0.527	0.030
Gd	closed	no	35	0.584	0.042
Gd	closed	no	41	1.208	0.046
Gd	closed	no	50	3.667	0.079
D_2O	open	yes	0	0.809	0.075
D_2O	closed	yes	0	0.475	0.040
D_2O	open	yes	30	0.803	0.051
D_2O	open	yes	32	0.808	0.082
D_2O	closed	yes	32	0.440	0.045
D_2O	open	yes	33	0.979	0.072
D_2O	closed	yes	33	0.571	0.039
D_2O	open	yes	34	1.034	0.058
D_2O	closed	yes	34	0.641	0.056
D_2O	closed	yes	35	0.887	0.059
Gd	open	yes	0	0.769	0.062
Gd	closed	yes	0	0.407	0.040
Gd	open	yes	32	0.764	0.077
Gd	closed	yes	32	0.434	0.041
Gd	open	yes	33	0.806	0.062
Gd	closed	yes	33	0.464	0.053
Gd	open	yes	34	0.829	0.065
Gd	closed	yes	34	0.484	0.054
Gd	closed	yes	35	0.501	0.044

Table 3.6.: Measured intensities depending from velocity, sample, shielding and status of the VCN-beam

value of the measurement. Hereby the value at a rotation frequency of 50 Hz is to prefer. For this value the influence of the background fluctuation is the lowest because of the highest measured intensity. With the help of Eqn. 3.1 a value of $b_c'' = 10.12 \pm 0.54$ fm is obtained.
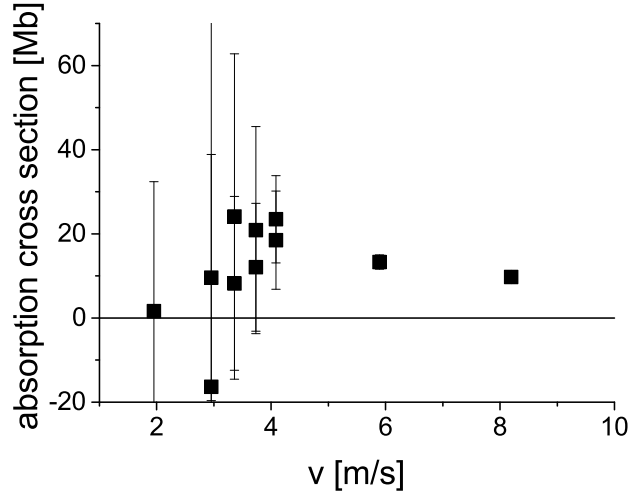
Figure 3.27.: Measured velocity dependent neutron absorption cross section

3.3.6. Conclusion

As part of this work a velocity selector for ultra-cold neutrons has been designed, build and tested. The selector fulfills the requirements presented to it: a broad UCN velocity spectrum can be reduced to a narrow range, tunable from 0-15 m/s, with no visible side-peaks in the spectra. A theoretical velocity resolution of $\frac{\Delta v}{v} = 10\%$ would be achieved for a parallel neutron beam. For the neutron beam and its angular distribution found on the PF2 TES beam a maximal resolution of 16% with a transmission efficiency within the range of 3-6% was measured. The frequency setting has been proven to be stable.

As an application of the selector the velocity dependent neutron absorption cross of Gd has been measured. Compared to a time-of-flight measurement this method has proven to be less practical. The main problem is the determination of the background count-rate. Since this has do be done in a separate measurement it can not be considered strictly related to the preceding measurement. In combination with the low count-rate for neutrons with low velocities this is a serious problem. The first time the signal count-rate exceeds the background is at a velocity of 5.89 m/s within the sample. This fact causes a large uncertainty of the calculated values. On account of this no new insights in the behavior of the absorption cross section for velocities tending to 0 m/s arise from this measurement. Also the calculated value for the imaginary part of the bound coherent absorption cross section $b_c'' = 10.12 \pm 0.54$ fm have to be treated with caution.

4. Neutron absorption in a moving sample

4.1. Introduction

So far giant neutron absorption cross sections have been realized be using neutrons with the lowest available velocity spectrum, i.e. UCNs. However, the use of UCNs has several disadvantages, compared to higher energy neutron sources. The average neutron flux is significant lower, what extends the measuring time to achieve reasonable error bars, especially in measurement like the previous presented, where the transmission values are additionally decreased by absorption effects. In addition the UCN trajectories have a broad angular distribution. An UCN beam can not be compared with a typical particle beam, where it can be assumed that all particles have the same direction. Its behavior is better described by a gas streaming through the guide-tubes. Collimation of such a beam is connected in any case with high losses. A further problem is that because of the low energy of the neutrons, the reflectivity of the most materials is not negligible. Neutrons are reflected on windows, which separate different vacuum environments and also on the surface of the sample itself, so that they do not contribute any more to a transmission measurement.

To avoid all this factors the use of neutrons with higher energy has been considered. Realizing nevertheless the desired low velocities and the related high absorption cross section can be done with the help of a Galilean transformation. In practice this means that the absorbing nucleus must travel along the neutron's trajectory, reducing thereby the relative velocity between them.

The simplest way to realize such an experiment is to send a neutron beam through a rotating absorber, so that the neutron trajectories appear as a secant line in the rotationally symmetric sample. Although the relative velocity between the neutrons and the nuclei in a setup like this is not constant, but position-dependent, this is the only possibility, which allows a continuous measurement.

In context of the meaning of such an experiment the question arises, which effect the movement of dense matter has on its complex neutron optical potential V_0, see Eqn. 2.174,

$$V_0 = \frac{2\pi\hbar}{m_n} N b_c \tag{4.1}$$

whereby its imaginary part refers to the neutron absorption. The potential results from an averaging in space over all nuclei, see Eqn. 2.170

$$V_m(\mathbf{r}) = \left\langle \sum_j \frac{2\pi\hbar^2}{m_n} b_j \delta(\mathbf{r} - \mathbf{r}_j) \right\rangle \tag{4.2}$$

this includes in fact only the total number of the absorbing nuclei, but not their state of movement. In the case of a rotating sample the number of nuclei in the corresponding volume is constant, hence not dependent from the rotation frequency. However, considering only a single nucleus the absorption is clearly dependent on the neutron-absorber relative velocity.

A known effect that appears when a neutron beam is transmitting a moving sample, what in the most experiments is realized by a rotation, is the neutron Fizeau effect [41, 42]. Contrary to the previous discussed case it concerns a phase shift appearing for a neutron wave when transmitting a moving sample. Since a phase shift of a neutron wave can only be observed in a context of interference phenomena, in the experimental demonstration the moving sample is mounted within a neutron interferometer setup.

The effect results from the Galilean transformation of the incident neutron wave into the system of the sample. The Fizeau phase shift appears because the phase shift caused by the transmission of the sample depends on the wave vector of the neutron beam. Consequently the phase shift of a Galilean-transformed neutron wave differs from the phase shift appearing in a system at rest.

According to [42] the additional phase shift is given by

$$\Delta\Phi_{Fizeau} = \frac{\alpha\beta k_x L}{2(1-\alpha)} \tag{4.3}$$

where k_x is the component of the wave vector in x-direction, L is the thickness of the transmitted sample, α is the ratio of the velocity of the boundary w_x to the x-component of the neutron velocity v_x and β is the ratio of the optical potential to the x-part of the incident neutron kinetic energy $E_{x0} = \hbar^2 k^2/2m_n$, so that

$$\alpha \equiv \frac{w_x}{v_x} = \frac{mw_x}{\hbar K - x} \ , \ \beta = \frac{V_0}{E_{x0}} \tag{4.4}$$

Contrary to the analog Fizeau effect in light optics, where the phase shift has a volume character, in neutron optics the effect is only due the movement of the sample boundaries and not due the movement of its matter proper.

Another effect resulting from a Galilean transformation of an incident neutron beam into the system of a moving sample is reported in [43]. More precisely the authors discuss an effect that appears when a neutron transmits an accelerated sample. The neutron incident velocity v_0 and the reduced velocity of the neutron inside the sample v, given in Eqn. 2.200, are firstly transformed with respect to a system moving with velocity V_1 and then with respect to a second system with velocity V_2. V_1 is here the velocity of the sample when the neutron traverses the its front surface and V_2 the sample's velocity when the neutron traverses the rear side surface. The authors obtain a final neutron velocity after transmitting the sample given by

$$v_f = V_2 + \sqrt{v_0^2 - 2V_1 v_0 + V_2^2 - 2(V_2 - V_1)\left[V_1 + \sqrt{(v_0 - V_1)^2 - v_c^2}\right]} \tag{4.5}$$

which differs from the incident neutron velocity v_0. The resulting change of velocity is

$$\Delta v = v_f - v_0 = \frac{ad}{v_0}\left(\frac{1}{n} - 1\right) \tag{4.6}$$

where a is the acceleration of the sample, d is its thickness and n is its index of refraction. The related energy shift is approximated with

$$\Delta E \approx m_n a d \left(\frac{1}{n} - 1\right) \tag{4.7}$$

This energy shift has been observed in the experiment.

Like these two effects in the following experiment an effect is expected resulting from the Galilean transformation of an incident neutron beam into the system of a moving sample. Contrary to the previous mentioned examples in the present experiment the focus is on the neutron absorption.

A special feature of this measurement is the realization of a neutron-absorber relative velocity tending to zero and the corresponding absorption cross section.

4.2. Concept of the experiment

To accelerate the absorbing nuclei in order to match the neutron's velocity a rotating sample in the shape of a cylinder is used. The setup is schematically shown in Fig. 4.1.

The velocity of the neutrons $\mathbf{v}'$ in a frame moving corresponding to the velocity of the absorbing sample $\mathbf{V}(\mathbf{r})$ is given by Galilean transformation:

$$\mathbf{v}' = \mathbf{v} - \mathbf{V}(\mathbf{r}) \tag{4.8}$$

Detector Reflection

Detector Transmission

Chopper

Aperture

VCN

Vacuum vessel   Rotating sample
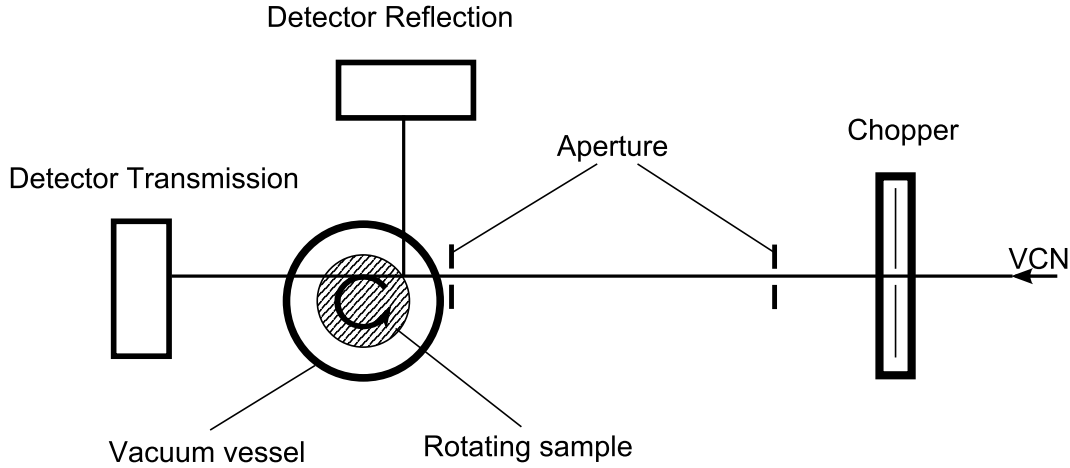
Figure 4.1.: Concept of the experiment

where $\mathbf{v}$ is the neutron velocity in the laboratory system. Assuming the neutron trajectory lies within a plane perpendicular to the sample's rotational axis the system reduces to two dimensions. Without loss of generality the neutron velocity is set parallel to the x-direction and the rotational axis of the sample is set to the origin of the coordinate system. In this case $\mathbf{v}'$ is given by

$$\mathbf{v}'(\mathbf{r}) = \begin{pmatrix} v \\ 0 \end{pmatrix} - \begin{pmatrix} \omega y \\ \omega x \end{pmatrix} = \begin{pmatrix} v - \omega y \\ -\omega x \end{pmatrix} \tag{4.9}$$

where ω denotes the angular velocity of the sample's rotational movement.
Choosing this angular velocity as

$$\omega = \frac{v}{y_0} \tag{4.10}$$

the transformed neutron velocity on the point $(0, y_0)$ results to be 0 m/s and therefore the absorption cross section diverges, if the 1/v-law is valid. Away from this point $|\mathbf{v}'(\mathbf{r})|$ increases, decreasing thereby the absorption cross section. Fig. 4.2 shows the calculation of the position dependent ab-
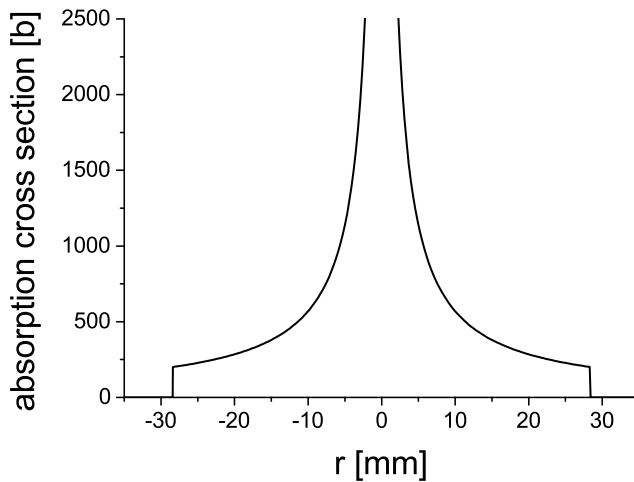
Figure 4.2.: Calculated position dependent neutron absorption cross section for a neutron velocity $v_n = 100$ m/s in a rotating Al-cylinder with matching rotational frequency

sorption cross section concerning thereby the absorbers rotational motion.
To demonstrate this effect an experiment is best performed using neutron velocities in the order

of 100 m/s, what correspondence to the very-cold neutron spectrum. Using neutrons from a lower energy band, like ultra-cold neutrons, the detectible neutron flux will decrease strongly. One reason is the stronger absorption respectively the resulting lower transmission given by Eqn. 3.1 and Eqn. 3.13. Another reason is the general lower neutron flux of UCN-sources. An additional effect concerning UCN that must be taken into account is refraction. The index of refraction n is a function of the neutron energy, see Eqn. 2.178

$$n^2 = 1 - \frac{V_F}{E} \tag{4.11}$$

For example the angel α a neutron is diffracted when passing a graphite cylinder with a radius $r = 40$ mm in a distance of $d = 28.2$ mm is calculated for a neutron velocity of 10 m/s to be 32.2°, for a velocity of 100 m/s only 0.2°. The diffraction changes the length of the neutron trajectory in the sample, like shown in Fig. 4.3. Hence, for VCN diffraction effects can be neglected, what has
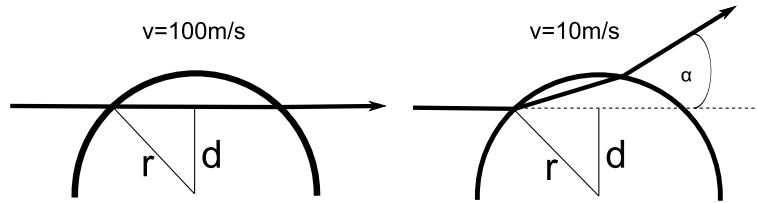
Figure 4.3.: Neutron trajectory through a cylinder shaped graphite sample with a radius $r = 40$ mm, entering in a distance $d = 28.2$ mm for different velocities

also the advantage the effects arising from the surface roughness of the sample are negligible.

For faster neutrons the dimensions of the proposed experiment grow to an unreasonable size, in particular the energy stored in the rotating cylinder. Considering that the rotational energy is given by

$$E_{rot} = \frac{1}{2}I\omega^2 \tag{4.12}$$

where I denotes the moment of inertia, which is calculated for a homogenous cylinder by

$$I = \frac{1}{2}mr^2 \tag{4.13}$$

where m is the cylinder's mass and r is its radius. Considering Eqn. 4.9 the energy increases as the square of the neutron velocity for a fixed absorber radius and a variable angular velocity. For a fixed angular velocity and a variable sample radius it increases even with the fourth power of the neutron velocity, because of the additional grow of the mass.

4.3. Experimental setup

For the previous mentioned reasons an experiment was designed for the neutron spectrum present at the VCN-beam of the ultra-cold and very-cold neutron facility PF2 of the ILL, where the experiment was also performed.

The lower boundary for the radius of the absorber cylinder is given, beside by the neutron beam collimation, by the realizable rotation frequencies. As a device, which provides the necessary rotation frequencies, a turbo pump motor is used. It has the additional advance, that it is equipped with a housing suitable for vacuum. Rotating the cylinder in vacuum reduces the necessary energy for maintaining the rotation frequency by reducing friction. For this reasons the absorber cylinder was mounted in stead of its rotor on a "Pfeiffer TPH170". The upper part of the housing is changed

in order to get a closed vacuum vessel. During the experiment the setup is pumped to a pressure in the range of 10^{-2} mbar. A 0.5 mm thick AlMg3 foil provides a neutron transmission window and separates the vacuum from the environment. Fig. 4.4 shows the setup. The turbo pump motor can

Figure 4.4.: Experimental setup with an without vacuum vessel

provide with this modifications rotation frequencies up to 600 Hz. Therefore an absorber cylinder with a diameter of 80 mm was chosen for the experiment. The neutron beam should passes the cylinder in a distance of $\frac{1}{\sqrt{2}}$ times the radius from the rotation axes, what is the condition for reflection of the neutrons on the surface on a 90° angle. The effective distance in the experiment was measured by scanning the absorber with the neutron beam, shown in Fig. 4.5. The scan is done with the help of the moveable table on which the device is mounted. A value of 29.8 mm was
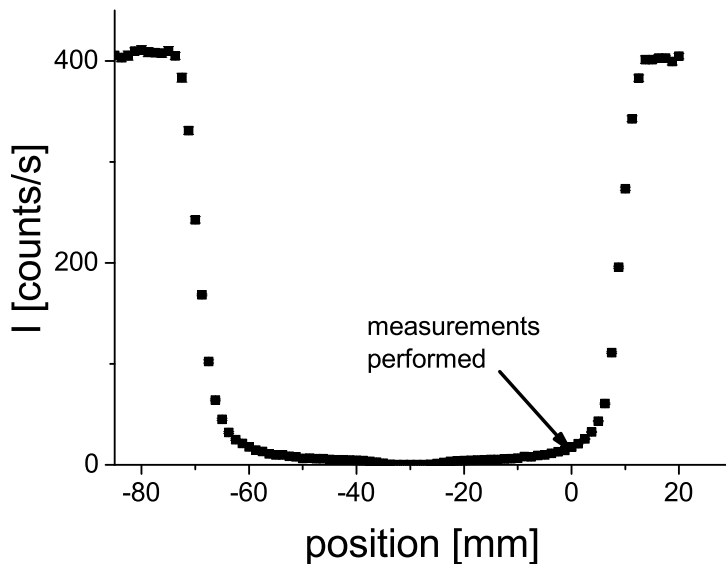
Figure 4.5.: Position scan of the absorber relative to the neutron beam; the origin correspondence to the measuring position

measured.

As absorber materials Al and graphite have been chosen. Considering the dependence of the transmission T from of the absorption cross section, given in Eqn. 2.217, the velocity dependency of the absorption cross section, given Eqn. 3.1, and the neutron-nuclei relative velocity in the sample, Eqn. 4.9, the transmission can be calculated. In principle the problem can be solved analytically

for defined starting conditions. Using distributions as starting values the calculation is done more efficient if based on Monte-Carlo simulation algorithms. The used distributions are the measured spectrum for the neutron velocity, a spacial distribution of the neutron starting point cause by the not point-like aperture and the angular distribution of the neutron trajectories. In Fig. 4.6
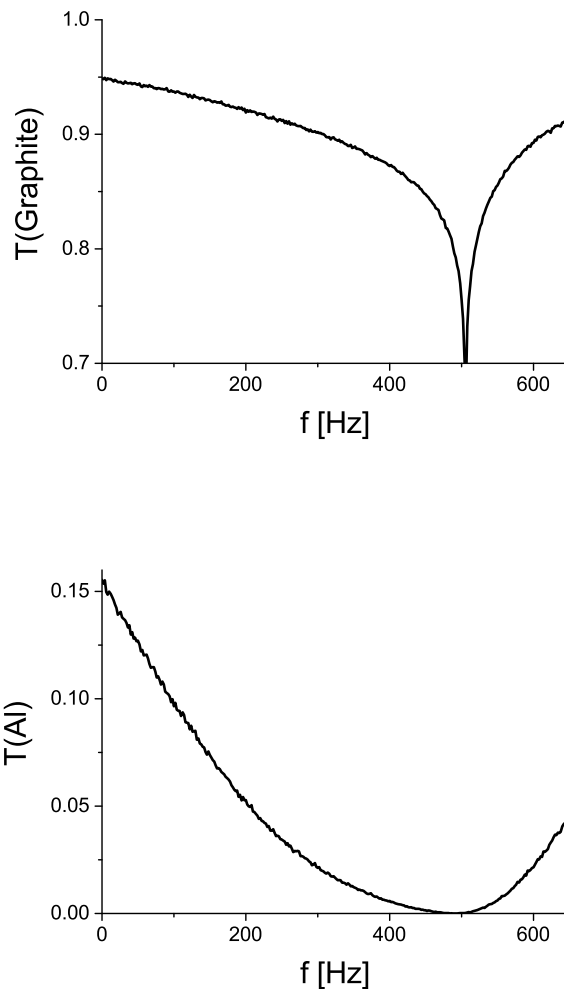
Figure 4.6.: Calculated transmission function for graphite and Al for a neutron velocity of 90 m/s, an absorber radius of 40 mm and a trajectory in 28.2 mm distance from the rotation axes

the results of the calculations for Al and graphite are shown. Only the velocity dependence of the absorption cross section has been considered, other effects, like elastic or inelastic scattering, have been neglected. The calculations show, that the use of weaker absorbers results in a sharper signal with higher contrast. This gives reason to the choice of the sample materials. Carbon with an absorption cross section for thermal neutrons of 0.0035 b and Al with 0.231 b [28] are both weakly absorbing elements.

For the mentioned construction parameters and the measured neutron velocity spectrum, shown in Fig. 4.7, the minimum of the transmission spectrum is expected in the region of 400 - 500 Hz. For the realizable frequency range these settings allow the measurement of the complete transmission
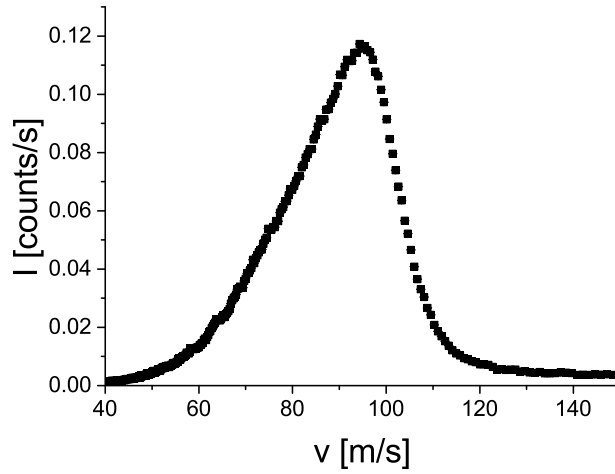
Figure 4.7.: VCN velocity spectrum, measured with time of flight method; same collimation used as in the other measurements reported in this work is used

function: the falling edge, the minimum and the rising edge.

After the alignment of the beam the collimation of the neutron beam is done by two Cd apertures. The first one is mounted directly on the device's vacuum vessel. It has an opening width of 2 mm in horizontal direction. The second aperture is mounted in a distance of 1.2 m, its opening width is set to 1 mm.

In a distance of 350 mm from the rotational axes a neutron detector is placed in the axes of the primary beam. A second detector is mounted under an angel of 90° to monitor the reflection of the neutrons on the surface of the absorber.

2035 mm in front of the primary detector a rotating disk chopper is positioned in the neutron beam. This allows measurement of time-of-flight spectra. The rotational frequency of the chopper is set to 20 Hz. The choppers transmission slit width of 15° implements a neutron pulse length of 2 ms. For full spectrum transmission measurements the chopper is fixed at its opening position.

The total neutron velocity spectrum, Fig. 4.7, was measured by dismounting the absorber sample.

4.4. Experimental results and analysis

The transmission signal was recorded with a modified Bidem-detector [44], i.e. a He^3-detector with a two-dimensional resolution. Its spacial resolution is given by a 128 x 128 pixel structure. Every pixel has the size of 2 x 2 mm^2 so that the total sensitive area is 256 x 256 mm^2. The actual signal was located in a limited region of the total active detector surface, as shown in Fig. 4.8. The neutron intensity was calculated only by the signals counted in this 23 x 19 pixel region of interest, which for all measurements includes the effective beam cross section. The detected signal outside the region of interest is used to define the background count-rate, what was in good agreement with a control background measurement. This control measurement was performed with a totally closed aperture in front of the sample.

For the standing samples a count-rate of 12.4 counts/s was measured for Al and 1.0 counts/s for graphite, while in the measurement with dismounted absorber a count-rate of 224 counts/s was obtained. The inconsistency with the expected values, plotted in Fig. 4.6, are probably related with scattering effects in graphite and possible water deposit in the material. The low count-rate for the
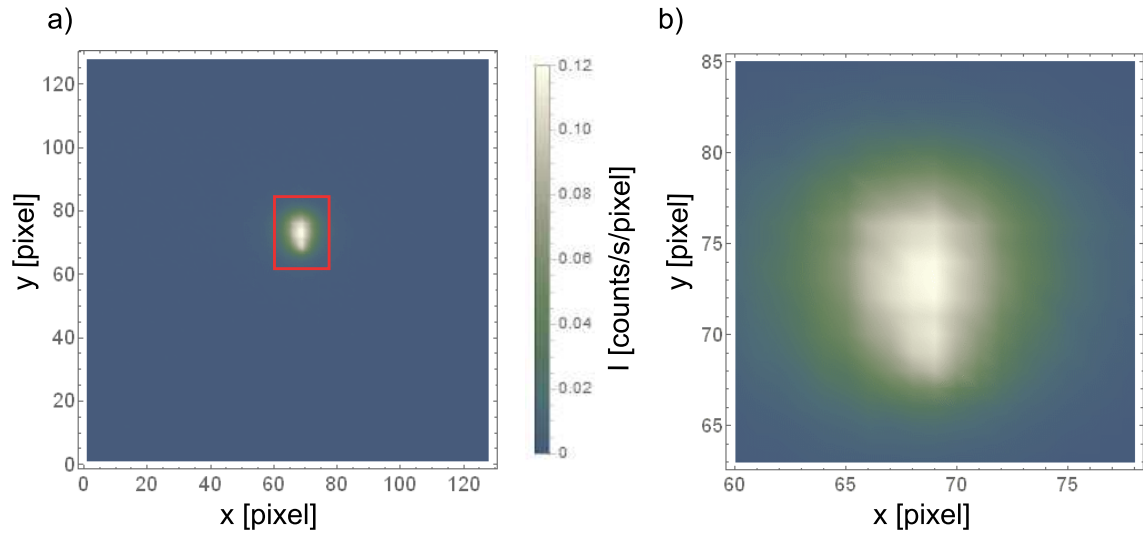
Figure 4.8.: Measured 2d-signal for standing Al-sample: a) total detector b) region of interest

graphite sample gave reason to concentrate the further measurements on the Al sample.

Another reason therefore is, that during the preparation for the experiment one of the graphite samples could not withstand the mechanical stress occurring at the maximal rotational frequency. For the Al sample measurements with multiple frequency settings were performed.

The detector monitoring the reflected beam, a Cascade U-200 detector [30], recorded for all settings only a signal at background level. This was to expect when calculating the reflectivity for Al according to Eqn. 2.204. A value of $R \approx 10^{-7}$ is obtained for the mean neutron velocity of the VCN spectrum. Even for Al_2O_3, what can expected to be found on the surface of an Al part, the reflectivity increases only by a factor of two.

The primary detector in contrast registered a significant signal with a clear dependency on the sample's rotational frequency. Fig. 4.9 shows the results. The transmission values are calculated
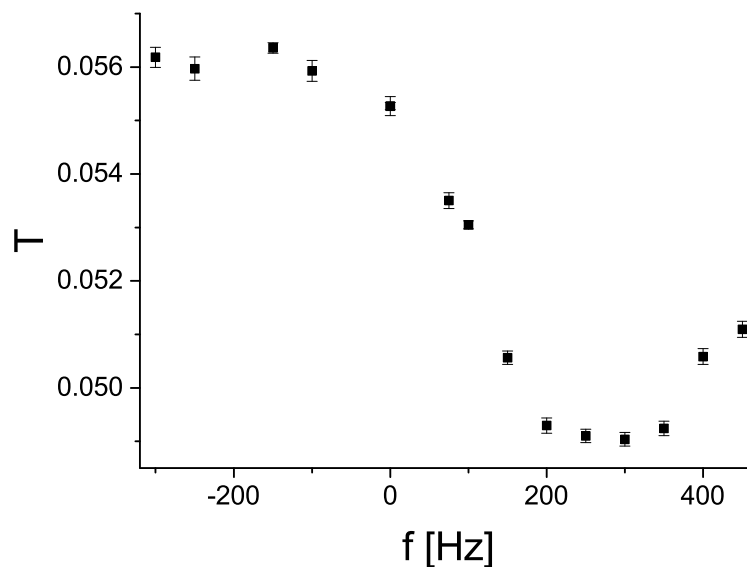
Figure 4.9.: Measured transmission as function of the rotating frequency of the Al sample

by comparing the recorded intensity for each frequency setting with the intensity of the control measurement with dismounted sample. As prove of consistency also measurements were performed with the sample rotating in the inverted direction. They result in the data points with negative frequency values.

In Fig. 4.9 a clear, significant minimum is visible in the transmission function. Additionally it is not symmetric in the origin, what rules out, that the effect is only caused by mechanical movements of the setup, like resonant vibration phenomena. That proves, that the measured effect actually depends on the relative velocity between neutrons and nuclei in the sample.

In Fig. 4.10 Monte Carlo simulation based calculations of the expected transmission function considering the measured neutron velocity spectrum are plotted. For the calculation Eqn. 3.1, Eqn. 2.217 and Eqn. 4.9 are used. The calculation shows the same behavior like the measured
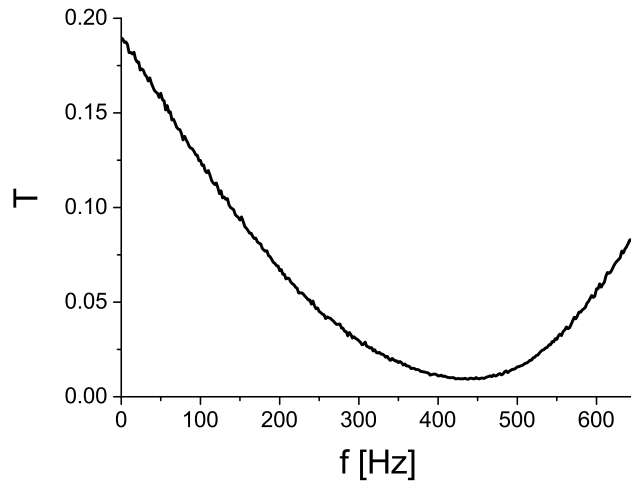
Figure 4.10.: Monte Carlo simulation base calculation of the transmission function

data, but no quantitative agreement has been observed. For the transmission value of the standing absorber as well as for the amplitude of the frequency dependent effect the measurement yields lower values than the calculation. This is an indication, that additional loss effects contribute to the measurement, which are not considered in the calculation. The origin of this additional effects can be scattering effects or impurities in the absorber material.

What can be excluded as origin of this inconsistency is, how already demonstrated, the reflectivity of the sample. As well as the influence of the Al_2O_3 layer on the surface. The typical thickness of such a oxide layer is in the range of 0.5 μm. Comparing with the overall sample thickness of 56.5 mm it is obvious that an influence is negligible, since the real part as well as the imaginary part of the scattering length density for both materials are comparable.

A possible explanation for an inconsistency between the measurement and the simulation could be given, when it is assumed that part of the detected neutrons have not participated on the interaction process with the sample. This could be the case, when the neutron beam is misaligned so that a part of the beam passes above or below the sample. In this case an additional correction term must be insert in the expression for the transmission, so that:

$$T = \frac{I_{mes} - I_{cor}}{I_0 - I_{cor}} \qquad (4.14)$$

where I_{mes} is the measured neutron beam intensity with sample, I_0 is the measured intensity without sample and I_{cor} the intensity of the neutron beam not participating on the interaction.

Using the values of the simulation for T values for I_{cor} can be calculated. This values should be constant with respect of the corresponding error bars, if a misalignment of the beam is the origin of the discrepancy between measurement and simulation. In fact however, the values vary to a large degree, so that this explanation can be excluded.

Not only the numerical value of the simulated transmission does not match with the measured data, but also the position of the minimum and the corresponding resonance frequency are shifted to lower values. The minimum of the measured values lies in the range of 300 Hz. The Monte Carlo based simulations expect this minimum at 438 Hz. In the simple model used for the simulations the resonance frequency would appear at the measured value, if the maximum of the neutron spectrum is in the range of 56 m/s. An error in the measurement of the neutron spectrum in this size can be excluded. The offset between the TTL-signal given by the chopper as start signal for the measurement and the effective chopper opening function has been measured via a light optical setup and has been taken into account for the neutron spectra calculation. The second quantity needed for the velocity spectrum calculation is the length of the flightpath. An optical length measuring instrument supplied a value of 2035 mm. To shift the spectrum's maximum to 56 m/s the flight path length has to be in the range of 3500 mm.

Excluding a incorrect measurement the origin of the shifting of the resonance frequency is not understood.

Beside the transmission measurements in which the total spectrum of the VCN-source was used, also time-of-flight measurements were performed. This allows the investigation of the transmission function for a single velocity component. The results are shown in Fig. 4.11. A relation between the transmission minimum and the neutron velocity is visible. For lower velocities the minimum can be found at lower frequencies. This is consistent with the premise of a dependence of the absorption cross section from the velocity of the absorbing nuclei. Because of the large error bars an exact calculation of the transmission function for a single velocity component is not possible. The bad statistic is caused, beside by the spectral resolution, by chopper duty cycle. The neutron flux is reduced because of the use of the chopper to 4% of the previous value.

The transmission as a function of the neutron velocity in the laboratory system can be calculated from the measured time-of-flight spectra. The comparison of two resulting transmission data sets for different rotational frequency settings of the sample is plotted in Fig. 4.12. A decrease of the transmission is shown for the sample rotating with 250 Hz in the region between 60 and 100 m/s compared with the results for the sample at rest. The expected increase in the region of 0 m/s can

$f\,[\text{Hz}]$	x	y
0	67.26	72.95
75	67.01	72.75
100	66.74	72.83
150	66.93	72.78
200	66.68	72.75
250	66.59	72.61
300	66.93	72.70
350	66.81	72.38
400	66.90	72.53
450	67.08	72.50
500	66.91	72.58

Table 4.1.: Averaged position of the beam for different sample rotational frequencies
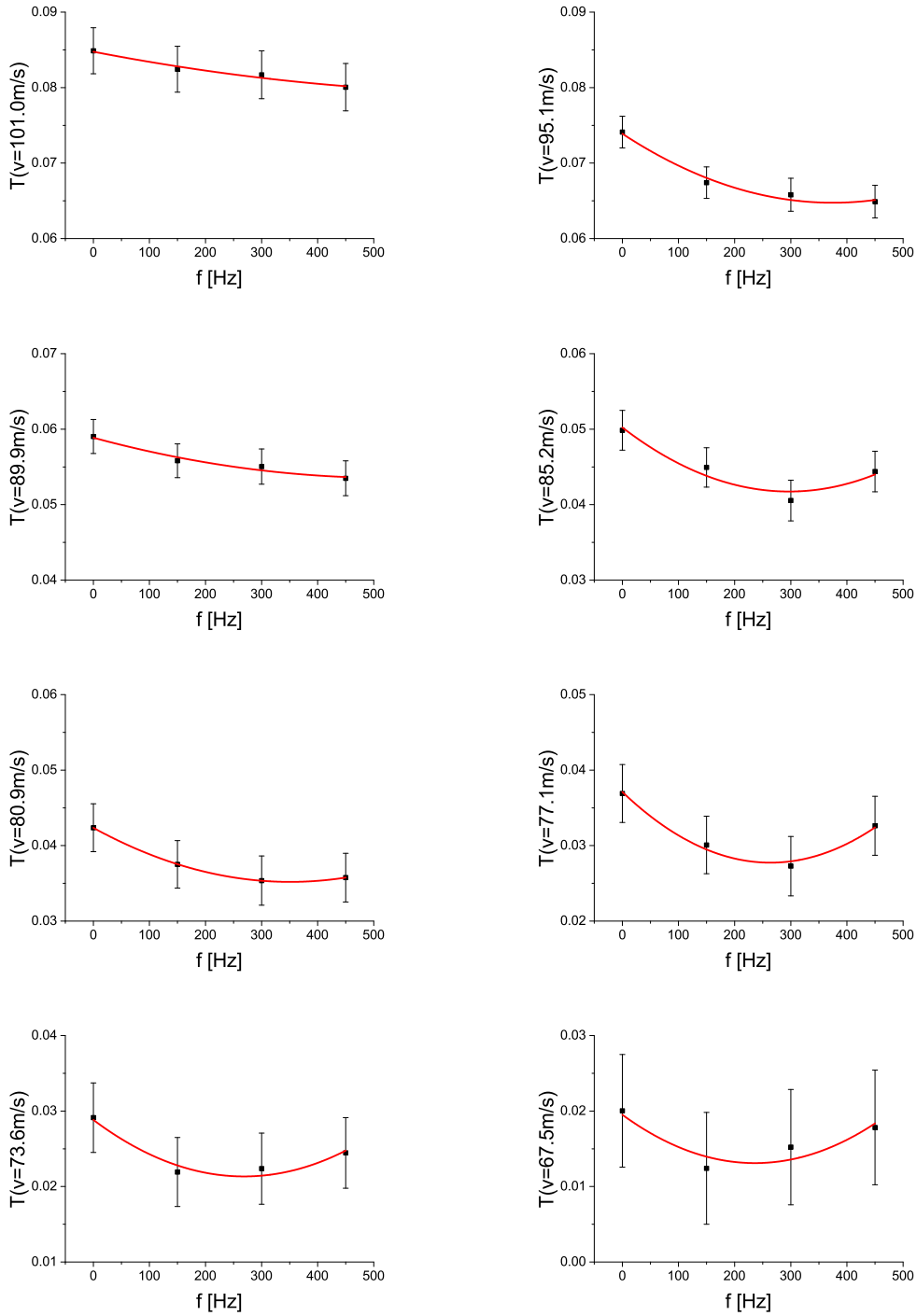
Figure 4.11.: Transmission as function of the rotating frequency of an Al sample for different neutron velocities, measured with time-of-flight method. Line: polynomial fit of the data points, error bars not considered; demonstrates the shift of the transmission function's minimum.
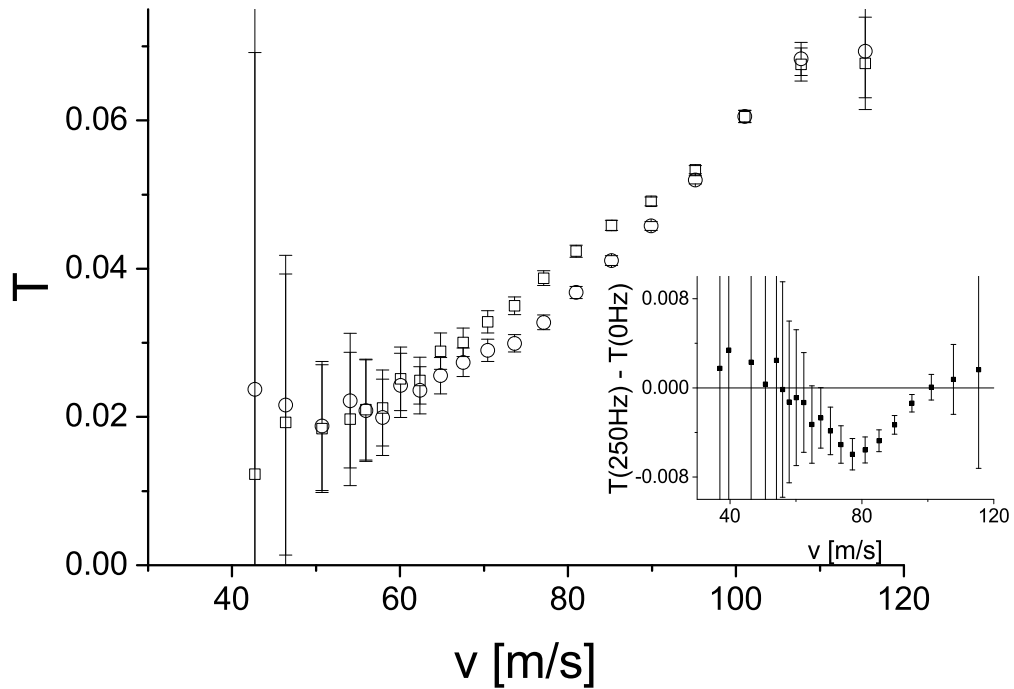
Figure 4.12.: Transmission as function of the neutron velocity, calculated from time-of-flight spectra. □ sample at rest, ○ sample rotating with 250 Hz

not be displayed due to the lack of neutron intensity.

The acquired data allow the investigation in the velocity dependence of other quantities. For example possible occurring refraction effects can be examined on dependencies of the samples rotational frequency. If such an effect exists, then a change in the angel of the outgoing beam should appear, what would change the position of the beam on the detector. To quantize the effect the averaged position of the beam is calculated in Tab. 4.1. From the data no significant shift of the beam position is visible.

The comparison of the beam cross section of the control measurement with dismounted sample with the beam cross section of a measurement with the sample shows clearly a broadening of the beam, as visible in Fig. 4.13. The origin of this broadening lies in scattering processes within the sample. To examine, if this effect depends on the rotational frequency of the sample, the size of the areas of the same signal intensity can be analyzed. In Fig. 4.14 the equipotential areas for different beam intensities are plotted. A slightly dependence of the beam cross section on the rotational frequency is visible. Near the resonance frequency the beam cross section is larger than away from it.
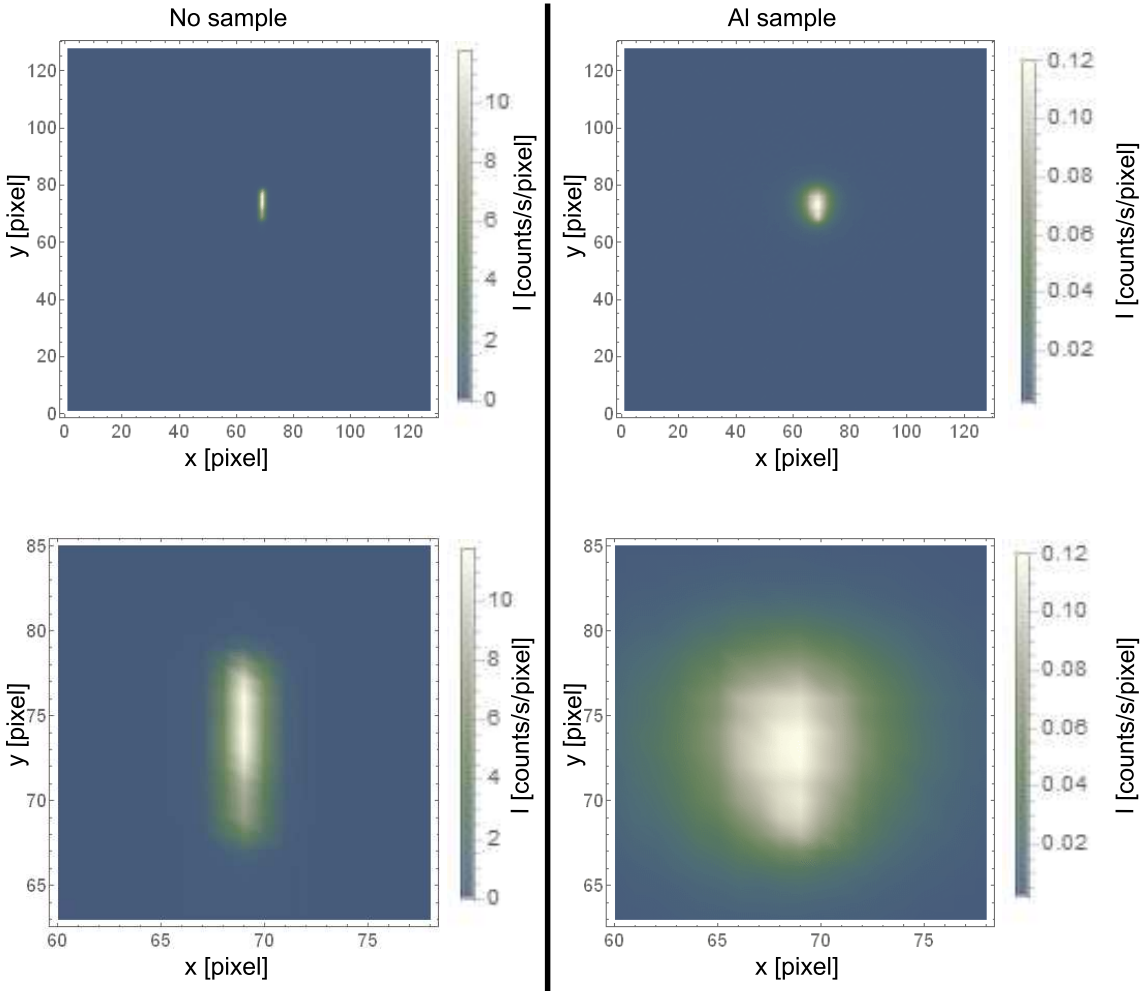
Figure 4.13.: Beam cross sections for control measurement and Al sample
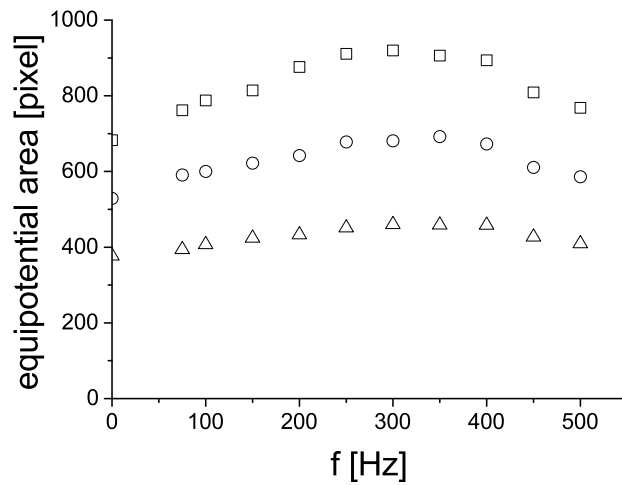
Figure 4.14.: Equipotential areas for different intensities as function of the sample rotational frequency. □ 3 x the background level, ◯ 5 x the background level, △ 10 x the background level

4.5. Conclusion

The dependence of the neutron absorption cross section from the movement of the absorbing nuclei has been demonstrated experimentally. For this purpose the transmission of VCN through a rotating Al cylinder has been measured. The result shows a resonance structure, depending from the rotation frequency of the absorber. Although the measurement shows, that consideration of a Galilean transformation of the incident neutron velocity and its effect on the absorption cross section is not enough to describe the system completely, there is no doubt, that the movement of the absorber has an influence on the transmission function.

The use of samples with a higher degree of purity would improve further experiments. The in this experiment used Al sample was a standard workshop piece of AlMg3 with unknown impurities. It fulfills the requirements of a prove-of-principle measurement but for a precision measurement the use of a high purity material is necessary.

For a future reinvestigation of the observed effect the use of a monochromatized neutron beam or a time-of-flight setup is recommended. The analysis of the effect is more conclusive, if a single neutron velocity component is used. However, a condition therefore is a measurement with sufficient statistics. The present results were recorded during an effective measuring time of approximately two weeks, while the time-of-flight measurements were performed in less than one week. For future experiments a significant longer measuring time is recommended.

Another possible improvement is the use of materials with a lower imaginary scattering length b_c'', what implies a lower absorption. This leads to a sharper resonance structure with higher contrast. More information about the processes in the sample could so be obtained.

An additional aspect that must be taken into account is the structure of the sample. Measurements with crystalline and amorphous materials could provide some additional information about scattering effects in the system.

An improved experiment in principle would allow the measurement of b_c'', it also could provide information on the behavior of the absorption cross section for velocities even closer to 0 m/s than these reached in the experiments discussed in the previous chapters.

5. Cold neutron reflectometry with Gd

5. Cold neutron reflectometry with Gd

5.1. Introduction

According to Eqn. 2.204 not only the transmissivity of a sample but also its reflectivity is given by the bound neutron scattering length density. With the help of the critical incident angel of total reflection

$$\phi_c = \sqrt{\xi} = \frac{\lambda}{\lambda_c} = \lambda\sqrt{\frac{Nb_c}{\pi}} \tag{5.1}$$

the reflectivity can be written as a function of the incident angle ϕ

$$R = \left|\frac{1 - \sqrt{1 - (\phi_c/\phi)^2}}{1 + \sqrt{1 + (\phi_c/\phi)^2}}\right|^2 \tag{5.2}$$

Total reflection is measurable even with thermal and cold neutrons under small but still resolvable angels. Typical reflectivity functions with respect to the incident angle are shown in Fig. 5.1, where it is assumed that b_c is real. In this case ϕ_c is real for $b_c > 0$ and for $b_c < 0$ it is purely
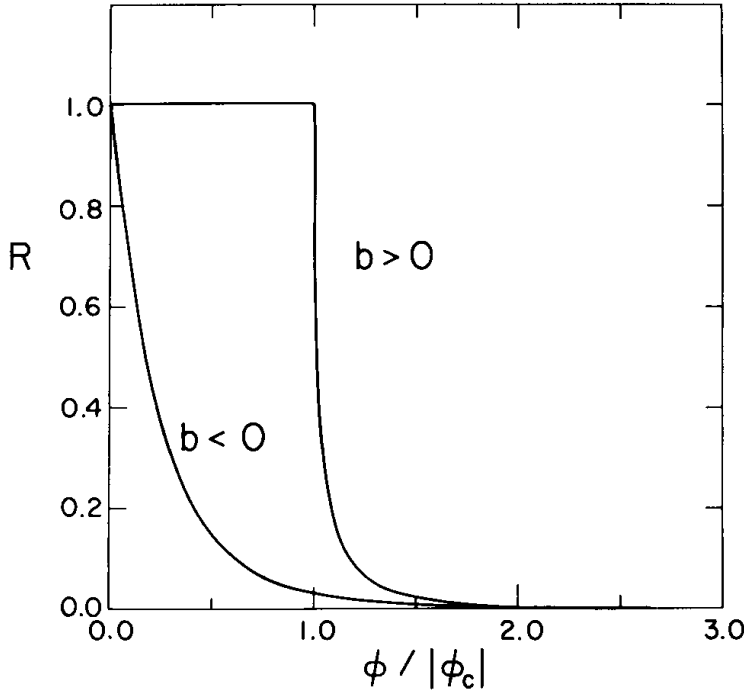
Figure 5.1.: The reflectivity as a function of the reduced angle of incidence for mirror reflection at a plane boundary. The bound coherent scattering length b_c is assumed to be real. [6] p.69

imaginary. In the former case is $R = 1$ for $\phi < \phi_c$ and decreases rapidly for $\phi > \phi_c$. Using this fact the optical potential respectively the bound neutron scattering length density can be determined precisely. The neutron mirror reflection technique [6, 45] is therefore a well-known and established method for the measurement of b_c. Using this technique the reflectivity R of a sample is measured as a function of the incident angle by scanning this angle with a collimated monoenergetic neutron beam. To avoid diffuse reflection on the sample a surface with high planarity is required.

In the case of strongly absorbing materials like Gd b_c can not assumed anymore to be real, consequently also its imaginary part b_c'' must be taken into account. The primary effect of the imaginary part on the the reflectivity function is to round off edges at the critical angle, like it is shown in Fig. 5.2. The plot shows that even for strongly absorbing materials the reflectivity does
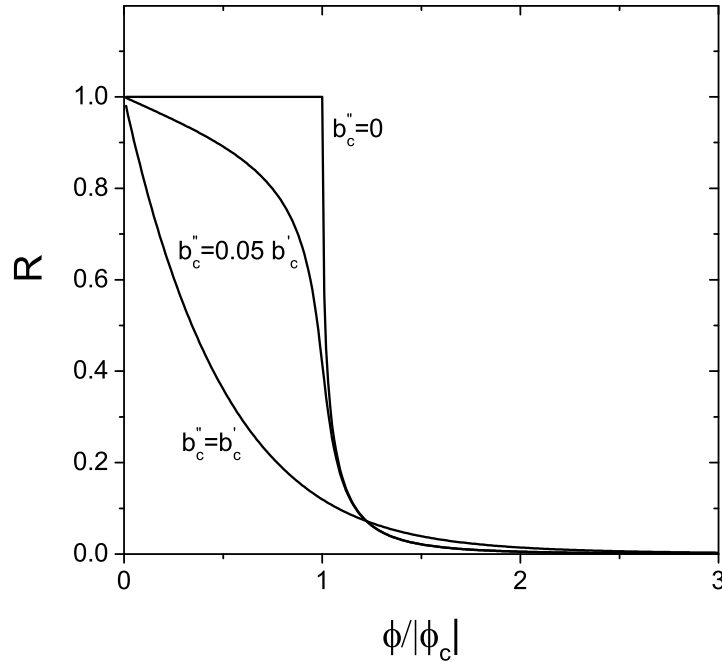
Figure 5.2.: The reflectivity as a function of the reduced angle of incidence for mirror reflection at a plane boundary for different relation of b'_c to b''_c

not vanish. For example even for Gd a reflectivity of 18% is expected at ϕ_c for thermal neutrons. With an adapted model the complex scattering length can be extracted from such a reflectivity measurement.

5.2. Experimental setup

To determine the imaginary part of the scattering length of Gd independently form the methods presented previously in this work a reflectometry measurement was performed at the TREFF instrument at the Forschungs-Neutronenquelle Heinz Maier-Leibnitz (FRM-II) research reactor in Garching (Germany) [46].

The instrument provides a monochromatic neutron beam with a wavelength of $\lambda = 4.8$ Å collimated by two apertures with a width of 0.5 mm in a distance of 1.8 m. Therefrom results a angular divergence of $2.7 \cdot 10^{-4}$ rad. For the measurement the angular resolution of the angle ϕ is set to 0.02° and the range from 0° to 3° is scanned.

As sample a glass substrate coated with a 200 nm thick layer of Gd is used. On top of the Gd layer an additional 10 nm thick layer of Si is placed to prevent the Gd form reacting with the atmospheric oxygen. Both layers were build up in a sputtering facility. Because of this production process the density of the deposit Gd corresponds not with the density of the conventional metal phase. Therefore the particle density must be determined in a independent measurement. For this purpose X-ray-reflectometry was used. Here the X-ray reflectivity of the same sample is measured like in the neutron reflectometry as a function of the incident angle. In contrast to the neutron case the interaction potential of the X-rays are mainly given by electron shell of the atoms. This potential are well-known and documented in the literature.

For the measurement a Bruker D8 Discover X-ray reflectometer [47] was used. It operates with a

Cu target X-ray-tube and provides therefore a monochromatic beam, using the Cu-Kα line with a wavelength of $\lambda = 1.54$ Å.

5.3. Experimental results and analysis

Fig. 5.3 shows the result of the X-ray measurement of the Gd sample. The red line in the plot
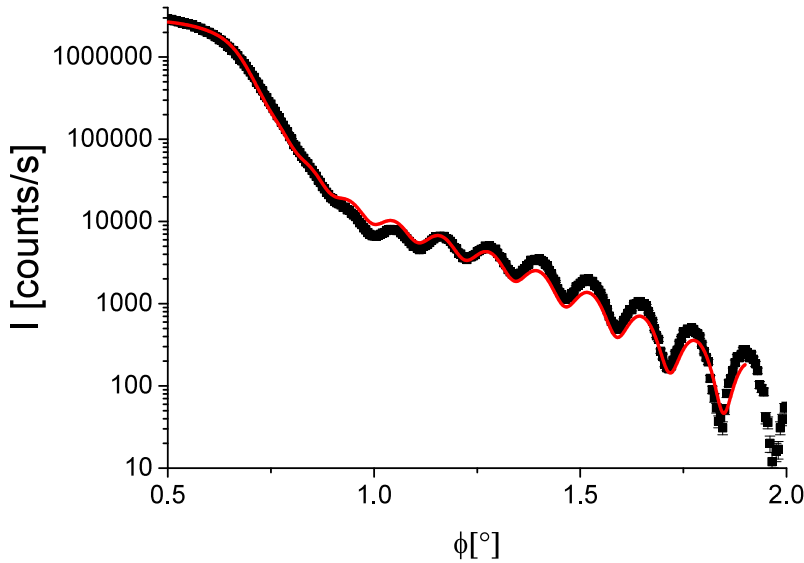
Figure 5.3.: X-ray reflectometry measurement of the Gd sample. Red line: fitted theoretical reflectivity function

represents the fit of the reflectivity function in respect to the measured data. The free fit-parameter in the algorithm [48] are the roughness of boundaries between the different materials, as well as the thickness of the single layers and the particle density N in the Gd layer. A particle density in the Gd layer of $N = 2.391 \pm 0.0066 \cdot 10^{28}$ m^{-3} is found as result of the fit. This corresponds to 79.18% of the particle density in the conventional metallic bonding of Gd.

The bound neutron scattering length can be calculated with this knowledge from the results of the neutron reflectometry measurement. The results of the measurement and the corresponding fit of the reflectivity curve are shown in Fig. 5.4. The real part of the scattering length b'_c has been fixed in the fit algorithm. The literature value of 9.5 fm [28] is assumed to be correct. The free parameter in the fit are the imaginary part of the scattering length and as before the thickness of the layers and the roughness of the boundaries. In both measurements the thickness of the layers and the roughness of the boundaries are calculated with matching values with respect to their error bars. The roughness of the Si surface and the boundary between Si and Gd is for both measurements in the region of 2 nm. For the thickness of the Si layer a value of 11.48 ± 0.35 nm. is calculated For the Gd layer a value of 62 ± 0.5 nm is determined. Finally for b''_c a value of 12.81 ± 0.47 fm is obtained.
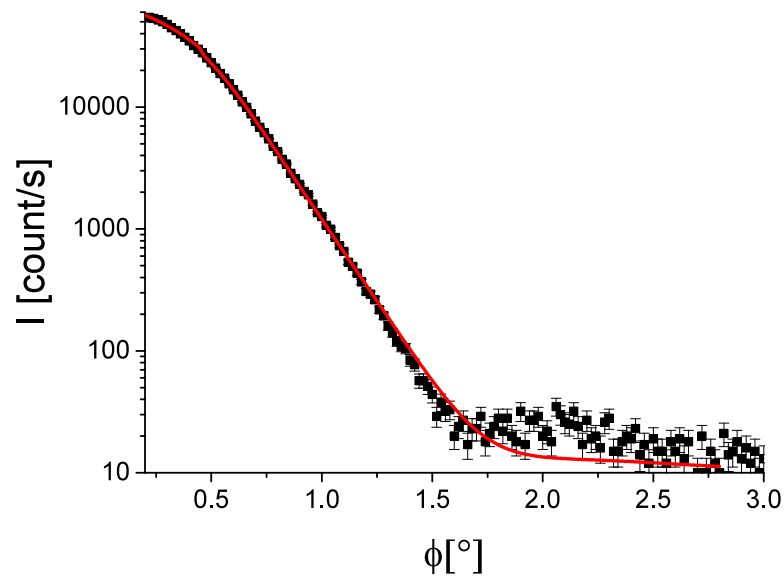
Figure 5.4.: Neutron reflectometry measurement of the Gd sample. Red line: fitted theoretical reflectivity function

5.4. Conclusion

With neutron reflectometry, an alternative method to the previous presented, the imaginary part of the bound neutron scattering length of Gd was measured. Despite the high absorption of the material a value of 12.81 ± 0.47 fm could be extracted from the measured data. The value varies from the value listed in literature [49] of 13.6 fm, however it lies within a region of 2σ.

6. Conclusion and Outlook

6. Conclusion and Outlook

In the present work several experiments to the topic of the giant absorption of neutrons are presented.

The neutron absorption cross section for Gd in its natural isotopic abundance and for enriched ^{157}Gd was measured with a time-of-flight setup installed on two different beam ports of the ILL PF2 instrument. Hereby the Gd is dissolved in D_2O, what allows the optimization of the transmission value by choosing the corresponding Gd concentration in the sample. A further advantage is that hereby lower neutron velocities can be realized than present in the spectrum of the neutron source, because the neutrons lose a part of their kinetic energy in the optical potential of the solvent.

From comparison with a transmission measurement of a sample with pure D_2O the absorption cross section of the Gd can be calculated.

After several steps of improvement it was possible to measure absorption cross sections up to 100 Mb for ^{157}Gd with this setup.

Additionally the 1/v-dependency of the absorption cross section is examined. In the velocity region above 3 m/s no significant deviation is visible. In the region below further extrapolation of the absorption cross section as function of the velocity is not meaningful because of the size of the measured value's error bars. Although fitting models for the measured data beside the 1/v-law provide slightly better reduced-χ^2 values, this happens not to an extant, that a significant violation of the 1/v-law can be proven.

This result is in agreement with the theoretical calculations of the absorption cross section in [6] but not with the extensions of the theory given in [22] or [24]. Also in [1] values deviating from the 1/v-dependency are reported measured in a similar experiment. The present experiment can be considers as a continuation of this measurements. The different results are explained by the improvement of the setup. The most important is the use of a polyethylene foil as absorber on the inside of the walls of the flight path. This foil absorbs all otherwise reflected neutrons and prevents thereby possible non specular reflection. Such reflections lead to a falsification of the measured time-of-flight spectrum. The transmission values in the falling flanks of the spectrum are overrated in this case.

The main problem for the measurement is that two signals, both tending to zero, are compared. Although the experiment could acquire data for a long time, more than 40 days, a definitive answer to the check 1/v-law can not provide. This suggests that the possibilities of the used concept are on its limit. Significant improvements on the error limits in the lower velocity range are not to expect. For further investigations another approach will be necessary.

An alternative way to measure the absorption cross section is the use of a velocity selector setup. For this purpose a velocity selector operating in the velocity region of the ultra-cold neutron spectrum was designed and tested. For this velocity region it is the first functional apparatus of its kind. The selector was characterized at ILL PF2 instrument, installed on the TES beam port. It fulfills the requirements presented to it: a broad UCN velocity spectrum can be reduced to a narrow range, tunable from 0-15 m/s, with no visible side-peaks in the spectra. A theoretical velocity resolution of $\frac{\Delta v}{v} = 10\%$ would be achieved for a parallel neutron beam. For the neutron beam and its angular

distribution found on the beam port a maximal resolution of 16% with a transmission efficiency within the range of 3-6% was measured. The frequency setting has been proven to be stable, what implies the reproducibility of the transmission spectra.

For the measurement of the velocity dependent absorption cross section a similar concept as in the time-of-flight measurements is used. The transmission of a reduced neutron spectrum through Gd dissolved in D_2O is measured and compared with the that of pure D_2O.

Compared to a time-of-flight measurement this method has proven to be less practical. As in the previous measurement also here appears the problem that two signals, which are both tending to zero, have to be compared. The problem is even enforced by the fact that background count-rate can not be measured in situ. Since this has to be done in a separate measurement it can not considered strictly related to the preceding measurement. In combination with the low count-rate for neutrons in the lower velocity region this is a serious problem. The first time the signal count-rate exceeds the background is at a velocity of 5.89 m/s within the sample. This fact causes a large uncertainty of the calculated values. On account of this no new insights in the behavior of the absorption cross section for velocities tending to zero arise from this measurement. Also the calculated value for the imaginary part of the bound coherent absorption cross section $b_c'' = 10.12 \pm 0.54$ fm have to be treated with caution.

Although the selector setup does not perform as good as the time-of-flight setup in the measurement of the absorption cross section, the selector itself has proven to be a reliable instrument in UCN-physics. It can be used for better suite experiments. For example colleagues form LANL used it to supply their storage measurements with different nearly monochromatic neutron spectra.

On the search on a new approach to the topic of the giant absorption the idea was born to accelerate the absorbing nuclei to the velocity of the neutrons instead of using slow neutrons. This way the neutron-absorber relative velocity is reduced and as consequence the absorption increases. For this purpose the transmission of VCNs through a rotating Al cylinder has been measured. The result shows a resonance structure, depending from the rotation frequency of the absorber. This effect has been measured the first time.

Although the measurement shows that consideration of a Galilean transformation of the incident neutron velocity and its effect on the absorption cross section is not enough to describe the system completely, there is no doubt, that the movement of the absorber has an influence on the transmission function.

From the presented experiments this is probably the most promising for further investigation, especially since there is room for several improvements, beside a longer measuring time. For future experiments the use of samples with a higher degree of purity is recommended. The in this experiment used Al sample was a standard workshop piece of AlMg3 with unknown impurities. It fulfills the requirements of a prove-of-principle measurement but for a precision measurement the use of a high purity material is necessary.

Another possible improvement is the use of materials with a lower imaginary scattering length b_c'', what implies a lower absorption. This leads to a sharper resonance structure with a higher contrast. More information about the processes in the sample could thereby be obtained.

An additional aspect that must be taken into account is the structure of the sample. Measurements with crystalline and amorphous materials could provide some additional information about scattering effects in the system.

An improved experiment in principle would allow the measurement of b_c'', it also could provide information on the behavior of the absorption cross section for velocities even closer to 0 m/s than these reached in the time-of-flight measurement.

The final reported experiment is the measurement of the imaginary part of the scattering length b_c''

6. Conclusion and Outlook

of Gd. This is done with a reflectometer setup. With reflectometry the quantity can be measured independent form absorption effects and can give thereby a prove of consistency with the previous experiments.

Despite the high absorption of the material a value of $b_c'' = 12.81 \pm 0.47$ fm could be extracted from the measured data.

This method offers a possibility to reinvestigate the few values of b_c'' listed in the literature and to achieve new ones for material not yet measured. Most of the published values are extracted form absorption measurements in the region of thermal neutrons. Since resonance phenomena play in this region an important role, they can falsify easily the calculated value for b_c''.

Bibliography

[1] H. Rauch, M. Zawisky, C. Stellmach, and P. Geltenbort. Giant absorption cross section of ultracold neutrons in gadolinium. *Physical Review Letters*, 66(10):4955–4958, 1999.

[2] K.A. Olive et al. (Particle Data Group). *Chin. Phys. C*, 38(090001), 2015.

[3] Wolfgang Demtröder. *Experimentalphysik 4*, volume 2. Springer, 1998.

[4] J. Baumann, R. Gähler, J. Kalus, and W. Mampe. Experimental limit for the charge of the free neutron. *Phys. Rev. D*, 37:3107–3112, 1988.

[5] R. Golub, D. Richardson, and S. K. Lamoreaux. *Ultra Cold Neutrons*. Inst of Physics Pub, 1991.

[6] V. F. Sears. *Neutron Optics*. Oxford University Press, 1989.

[7] `www.ati.ac.at/~neutropt/scattering/ImaginaryScatteringLengths.PDF`, July 2015.

[8] A Serebrov, V Varlamov, A Kharitonov, A Fomin, Yu. Pokotilovski, P Geltenbort, J Butterworth, I Krasnoschekova, M Lasakov, R Tal'daev, A Vassiljev, and O Zherebtsov. Measurement of the neutron lifetime using a gravitational trap and a low-temperature Fomblin coating. *Physics Letters B*, 605(1-2):72–78, 2005.

[9] A Pichlmaier, V Varlamov, K Schreckenbach, and P Geltenbort. Neutron lifetime measurement with the UCN trap-in-trap MAMBO II. *Physics Letters B*, 693(3):221–226, 2010.

[10] S Materne, R Picker, I Altarev, H Angerer, B Franke, E Gutsmiedl, F J Hartmann, A R Müller, S Paul, and R Stoepler. PENeLOPE on the way towards a new neutron lifetime experiment with magnetic storage of ultra-cold neutrons and proton extraction. *Nuclear Instruments and Methods in Physics Research Section A: Accelerators, Spectrometers, Detectors and Associated Equipment*, 611(2-3):176–180, 2009.

[11] C. A. Baker, D. D. Doyle, P. Geltenbort, K. Green, M. G. D. van der Grinten, P. G. Harris, P. Iaydjiev, S. N. Ivanov, D. J. R. May, J. M. Pendlebury, J. D. Richardson, D. Shiers, and K. F. Smith. Improved experimental limit on the electric dipole moment of the neutron. *Phys. Rev. Lett.*, 97:131801, 2006.

[12] R. Golub and J.M. Pendlebury. Super-thermal sources of ultra-cold neutrons. *Physics Letters A*, 53(2):133–135, 1975.

[13] A. Steyerl, H. Nagel, F.-X. Schreiber, K.-A. Steinhauser, R. Gähler, W. Gläser, P. Ageron, J.M. Astruc, W. Drexel, G. Gervais, and W. Mampe. A new source of cold and ultracold neutrons. *Physics Letters A*, 116(7):347–352, 1986.

[14] Göltl. L. *Characterization of the PSI Ultra-Cold Neutron Source*. PhD thesis, ETH Zürich, 2012.

Bibliography

[15] Albert Steyerl and Herbert Vonach. Total cross-sections of various homogeneous substances for ultracold neutrons. *Zeitschrift für Physik*, 250(2):166–178, 1972.

[16] A. Palmgren, K. Krebs, and E. Tunkelo. Total neutron cross-section measurements in the 10 μev range. *Physics Letters B*, 27(9):554–556, 1968.

[17] A. Steyerl. Measurements of total cross sections for very slow neutrons with velocities from 100 m/sec to 5 m/sec. *Physics Letters B*, 29(1):33 – 35, 1969.

[18] J.A. Polo and J.M. Robson. Total cross section of vanadium for neutrons of 4.4 to 15.7 m/sec. *Physical Review C*, 27(1):133–136, 1983.

[19] A. Steyerl. Very low energy neutrons. In *Neutron Physics*, volume 80 of *Springer Tracts in Modern Physics*, pages 57–130. Springer Berlin Heidelberg, 1977.

[20] J. Felber and R. Gähler and R. Golub. Comment on giant absorption cross section of ultracold neutrons in gadolinium. *Physical Review Letters*, 85(26), 2000.

[21] H. Rauch, M. Zawisky, C. Stellmach, and P. Geltenbort. Rauch et al. reply. *Physical Review Letters*, 85(26), 2000.

[22] V. V. Lomonosov and A. I. Gurevich. Capture of ultracold neutrons in thin absorbing films. *Journal of Experimental and Theoretical Physics*, 95(5):800 – 804, 2002.

[23] A. I. Frank, V. I.Bodnarchuk, P. Geltenbort, I.L.Karpikhin, G. V.Kulin, and O.V.Kulina. Neutron optics of strongly absorbing media and interaction of long-wave neutrons with gadolinium films. *Physica of Atomic Nuclei*, 66(10):1831–1845, 2003.

[24] I. I. Gurevich and P.E. Nemirovsky. "Metallic" Reflection of Neutrons . *Sov. Phys. JETP*, 14:838, 1962.

[25] A. I. Frank, P. Geltenbort, G. V. Kulin, and A. N. Strepetov. Experimental verification of the 1/v law for the absorption cross section of ultracold neutrons in natural gadolinium. *JETP Letters*, 84(3):105–109, 2006.

[26] I. V. Bondarenko, A. V. Krasnoperov, A. I. Frank, S. N. Balashov, S. V. Masalovich, V. G. Nosov, P. Geltenbort, P. Hoghoj, A. G. Klein, and A. Cimmino. Experimental check of the dispersion law for ultra cold neutrons. *JETP Letters*, 67(10):786–792, 1998.

[27] J. Schroffenegger, P. Fierlinger, A. Hollering, P. Geltenbort, T. Lauer, H. Rauch, and T. Zechlau. Improved measurement of the neutron absorption cross section for very low velocities. *Physics Letters B*, 752:212 – 216, 2016.

[28] A. Dianoux and G. Lander. *Neutron Data Booklet.* Institute Laue-Langevin, Ocpscience, 2003.

[29] T. Lauer. *Investigation of a superthermal ultracold neutron source based on a solid deuterium converter for the TRIGA Mainz reactor.* Dissertation, Johannes Gutenberg Universität Mainz, Fachbereich Chemie, Pharmazie und Geowissenschaften, 2010.

[30] CDT CASCADE Detector Technologies GmbH. `http://www.n-cdt.com.`, 2015.

[31] A. Steyerl. A time-of-flight spectrometer for ultracold neutrons. *Nuclear Instruments and Methods*, 101:295–314, 1972.

[32] Glen Cowan. *Statistical data analysis.* Oxford University Press, 1998.

[33] L. Rosta. Neutron physical properties of a multiblade neutron velocity selector. *Physica B*, 156 & 157:615–618, 1989.

[34] B. Hammouda. Multidisk neutron velocity selectors. *Methods in Physics Research A*, 321:275–283, 1992.

[35] H. Friedrich, V. Wagner, and P. Wille. A high-perfomance, neutron velocity selector. *Physica B*, 156 & 157:547–549, 1989.

[36] C. M. Fleck, F. Höfferl, A. Slibar, and H. Springer. Ein Neutronenselektor mit hohem Auflösungsvermögen für die Materialforschung. *Atomenergie/Kerntechnik*, 35, 1980.

[37] C. D. Clark, E. W. Mitchell, D. W. Palmer, and I. H. Wilson. The design of a velocity selector for long wavelength neutrons. *J. Sci. Instrum.*, 43, 1966.

[38] Sturm Präzision GmbH. `www.sturm-bearings.com`, July 2015.

[39] National Instruments. `www.ni.com/pdf/manuals/371303m_0113.pdf`, July 2015.

[40] `www.arduino.cc/en/main/arduinoBoardUno`, July 2015.

[41] U. Bonse and A. Rumpf. Interferometric Measurement of the Neutron Fizeau Effect. *Physical Review Letters*, 56(23):2441–2445, 1986.

[42] Helmut Rauch and Samuel A Werner. *Neutron Interferometry: Lessons in Experimental Quantum Mechanics, Wave-Particle Duality, and Entanglement.* Oxford University Press, USA, 2015.

[43] A. I. Frank, P. Geltenbort, M. Jentschel, D. V. Kustov, G. V. Kulin, V. G. Nosov, and a. N. Strepetov. Effect of accelerated matter in neutron optics. *Physics of Atomic Nuclei*, 71(10):1656–1674, 2009.

[44] P. Geltenbort. Private communication, February 2016.

[45] W. C. Dickinson, L. Passell, and O. Halpern. Studies of the optics of neutrons. i. measurement of the neutron-proton coherent scattering amplitude by mirror reflection. *Phys. Rev.*, 126:632–642, 1962.

[46] www.mlz-garching.de/wissenschaft-und-projekte/instrumentservice/neutronenoptik.html, February 2016.

[47] Bruker Corporation. `/www.bruker.com/`, March 2016.

[48] T. Lauer. Private communication, 2016.

[49] SF Mughabghab. Neutron cross sections bnl-325. v. 1. parts b, edited by mughabhab sf, divideenam m., holden ne, 1984.

[50] T. Lauer. Private communication, May 2013.

[51] Wolfram Research, Inc. Mathematica, 2014.

List of Figures

List of Tables

Appendix

A. Chopper properties

The used linear chopper is build up by two titanium grinds. This grids are moved by two linear motors. In the closed position the grids are overlapping, in open position the apertures in the grids overlap, so that 60% of the hole cross section is passable for neutrons. Fig. A.1 shows a schematic illustration of the principle. Surveying the chopper opening function, an important value when
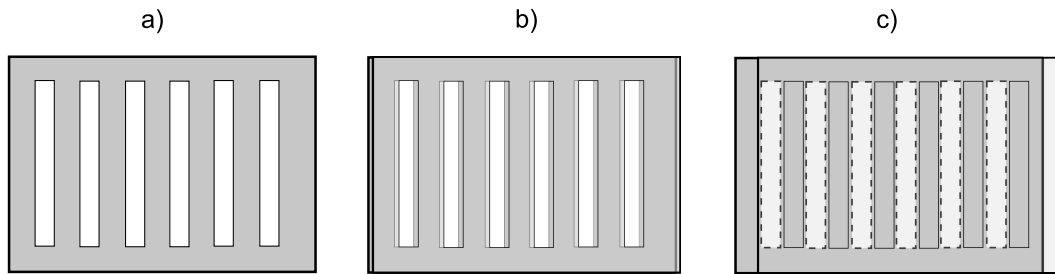

Figure A.1.: Chopper grids: a) single chopper grid, b) grids in open position, c) grids in closed position

it comes to deconvolving a time-of-flight spectrum, is best done in an optical way. To do so a light source is mounted in front of the chopper, behind the chopper a photo diode, screened from surrounding light, is installed. With an electronic data acquisition system the current produced by the diode, can be read out. This current as function of time is direct proportional to the chopper opening function. The normalized opening function for the opening time set to 7 ms is plotted in
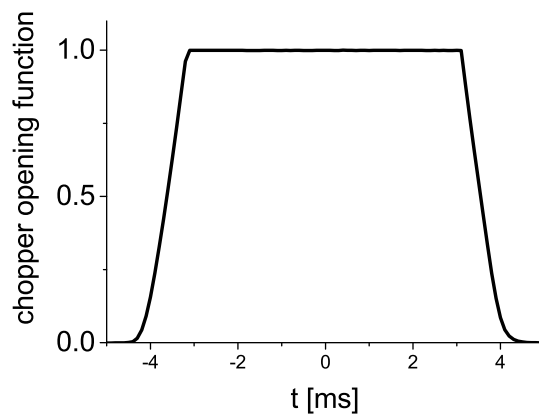

Figure A.2.: Measured opening function of the used linear chopper. Opening time set to 7 ms

Fig. A.2.
An important property of the chopper is the stability over time of its opening function. If this is not granted the reproducibility of acquired data is not given. To prove its stability the opening function in relation to the chopper trigger signal was measured every 3 min over a period of 3 days, what was repeated for different settings. The results are listed in Tab. A.1.
The deviation of the offset, which is the most sensitive quantity in an time-of-flight setup, is below 0.5%. This proves the stability and reproducibility of the opening function.

	value [ms]	std. dev. [ms]	relativ dev. [%]
offset	16.64	0.08	0.47
o.t. 10%	7.99	0.09	1.08
o.t. 90%	6.26	0.10	1.59
offset	23.62	0.06	0.24
o.t. 10%	21.91	0.04	0.18
o.t. 90%	20.13	0.05	0.25

Table A.1.: Chopper opening function properties. Offset refers to the time between trigger signal and middle of the opening function, o.t. 10% is the time the chopper function is higher than 10% of the maximum, o.t. 90% is the corresponding value for 90%.

B. Deconvolution of time-of-flight-spectra

A spectrum measured with a standard time of flight setup, a chopper, a flight path and a detector, is not only given by the neutron velocity distribution, but also the length and the shape of the chopper opening function has an influence on it. The time when a neutron enters the flight path and the corresponding probability is directly related to this opening function. Expressed in mathematical terminus the measured time of flight spectrum w_{mes} is a convolution of the chopper opening function w_{open} and the effective spectrum w_{eff}:

$$w_{\mathrm{mes}}(t) = (w_{\mathrm{eff}} * w_{\mathrm{open}})(t) = \int_{-\infty}^{\infty} w_{\mathrm{eff}}(t) w_{\mathrm{open}}(t - t_0) \, \mathrm{d}t_0. \tag{B.1}$$

$w_{\mathrm{open}}(t)$ can be measured for example with a light source and a photo diode, like discussed in appendix A. $w_{\mathrm{eff}}(t)$ is the only unknown function.

Fourier transforming the equation and using the convolution theorem is the analytical way to solve the problem:

$$\mathcal{F}(w_{\mathrm{mes}}) = \mathcal{F}(w_{\mathrm{eff}} * w_{\mathrm{open}}) = \mathcal{F}(w_{\mathrm{eff}}) \cdot \mathcal{F}(w_{\mathrm{open}}) \tag{B.2}$$

where $\mathcal{F}$ represents the Fourier transformation operator. By solving on $\mathcal{F}(w_{\mathrm{eff}})$ and applying the inverse Fourier transformation $\mathcal{F}^{-1}$ the effective spectrum is obtained

$$\mathcal{F}(w_{\mathrm{eff}}) = \frac{\mathcal{F}(w_{\mathrm{mes}})}{\mathcal{F}(w_{\mathrm{open}})} \quad \rightarrow \quad \mathcal{F}^{-1}\mathcal{F}(w_{\mathrm{eff}}) = w_{\mathrm{eff}} = \mathcal{F}^{-1}\left(\frac{\mathcal{F}(w_{\mathrm{mes}})}{\mathcal{F}(w_{\mathrm{open}})}\right) \tag{B.3}$$

However finding a solution typical fails in finding a integrable function for w_{mes} and w_{open}.

Mathematical software like Wolfram Mathematica [51] provide ready to use deconvolution algorithms. As an example the spectrum measured in December 2014 for the D_2O and the corresponding chopper opening function, shown in Fig. B.1, is deconvolved with the Wolfram Mathematica "ListDeconvolve" algorithm. The result, Fig. B.2, shows sinusoidal artifacts what is a correct so-
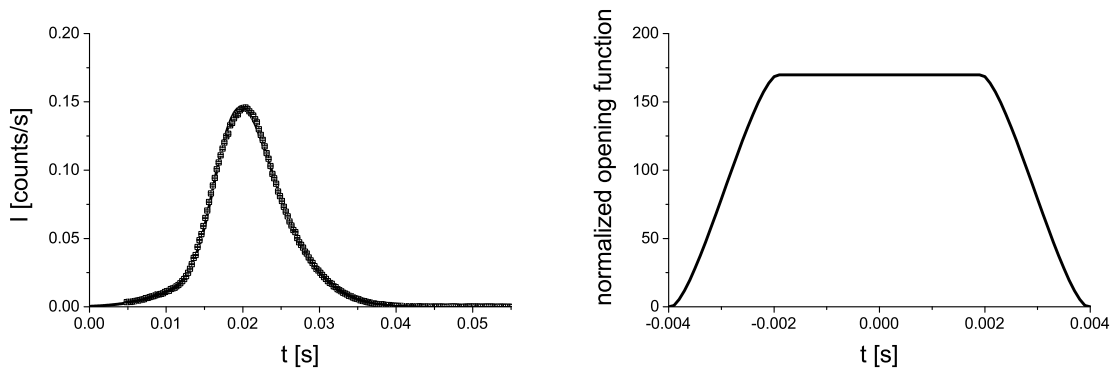

Figure B.1.: Time of flight spectrum for D_2O sample and corresponding chopper opening function

lution of the mathematical problem, but it does not leads to realistic velocity distribution of the neutrons.

A practical way to receive a physical meaningful velocity distribution is to adapting a spline-function to the measured date [50]. This is done by a fitting algorithm. Hereby the spline interpolations set points are the fitting parameters. In principle this procedure generates a spline-fit to the measured data point. Defining the fit-function as a convolution of the choppers opening function and a spline-function

$$f_{\mathrm{fit}}(t) = \int w_{\mathrm{open}}(t - t_0) f_{\mathrm{spline}}(p_1, p_2, ..., p_n, t) \, \mathrm{d}t_0. \tag{B.4}$$
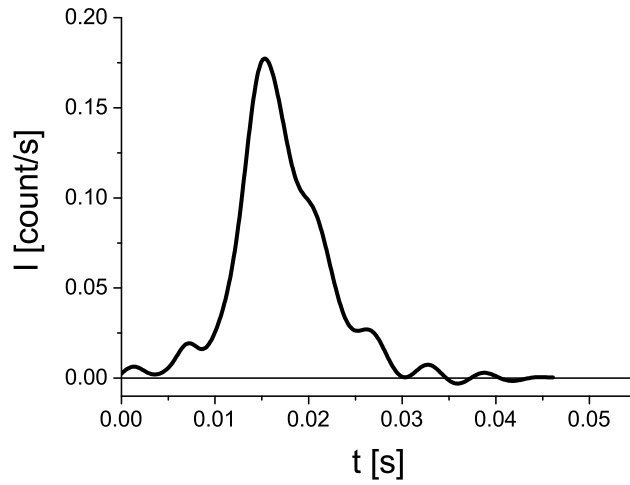
Figure B.2.: Result of the "ListDeconvolve" algorithm

gives the required interpolation set points p_i for the function $f_{\mathrm{spline}}(p_1, p_2, ..., p_n, t)$, which correspond to w_{eff}.

The result of this algorithm is plotted in Fig. B.3. As starting point the same data as before, Fig. B.1 were used. A critical parameter for this algorithm is the number of interpolation set points n.
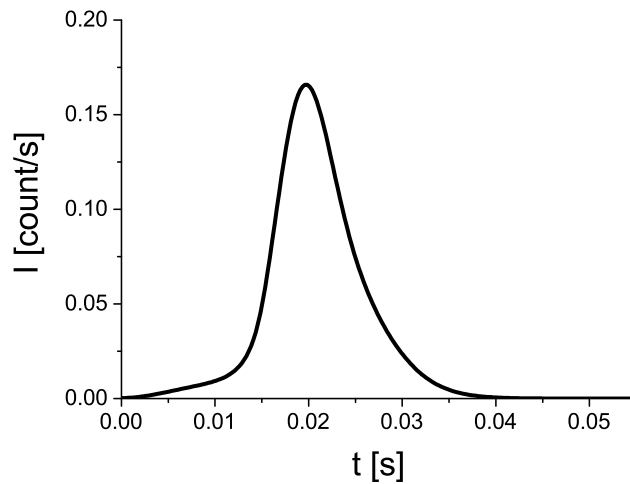

Figure B.3.: Result of the convolved-spline-fit-algorithm

With higher n increases the precision of the fit, but also the computing time. In the present work the algorithm was performed with n between 6 and 10. Lower n produce no adequate fit, for higher n the computing time reaches a non reasonable value.
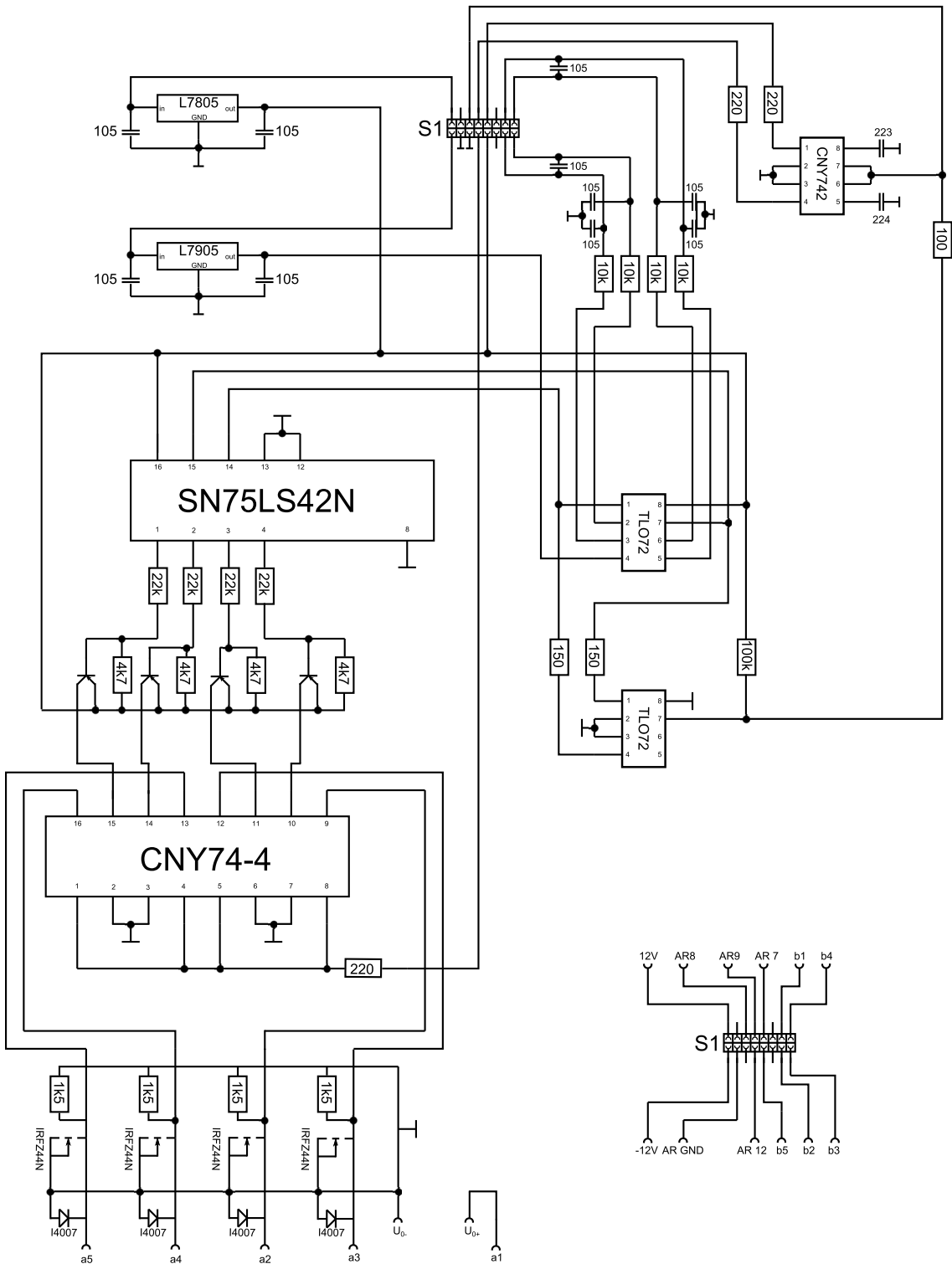
C. Motor control

Figure C.1.: Motor control circuit diagram

Arduino source code

```
const int switchPin=8; // Eingangspin
const int ledPin=13;
const int stromPin1=12;
const int stromPin2=11;
const int fehlerPin=10;
const int tiefpass224=9;
const int tiefpass223=7;


float foben=10.1;
float funten=10;
float f=0;
int fehler=0;
float fehlerzeit=10000;
float Zeit1,Zeit2,ausZeit;
int halten=0;
int strom=0;
float zeitbisfehler;
float zeitbreak1;
int f2=1;
int tp1,tp2;


void setup()
{
pinMode(switchPin, INPUT);
pinMode(ledPin, OUTPUT);
pinMode(stromPin1,OUTPUT);
pinMode(stromPin2,OUTPUT);
pinMode(fehlerPin,OUTPUT);
pinMode(tiefpass224,OUTPUT);
pinMode(tiefpass223,OUTPUT);
digitalWrite(switchPin, HIGH);
Serial.begin(9600);
}


void loop()
{
if(f<50) {digitalWrite(tiefpass224,HIGH);tp1=0;}
else
{
tp1++;
if(tp1>10)
{
digitalWrite(tiefpass224,LOW);
tp1=12;
```

```
}
}


if(f<500) {digitalWrite(tiefpass223,HIGH);tp2=0;}
else
{
tp1++;
if(tp1>10)
{
digitalWrite(tiefpass224,LOW);
tp1=12;
}
}


if(f<1)
{
digitalWrite(stromPin1,HIGH);
digitalWrite(stromPin2,HIGH);
strom=1;


if(digitalRead(switchPin)==LOW)
{
zeitbreak1=millis();
while(digitalRead(switchPin)==LOW& &f2!=0)
{
if(millis()-zeitbreak1>1000)f2=0;
}


}
if(digitalRead(switchPin)==HIGH)
{
digitalWrite(ledPin,HIGH);
zeitbreak1=millis();
while(digitalRead(switchPin)==HIGH& &f2!=0)
{
if(millis()-zeitbreak1>1000)f2=0;
}
Zeit1=millis();
digitalWrite(ledPin,LOW);


zeitbreak1=millis();
while(digitalRead(switchPin)==LOW& &f2!=0)
{
if(millis()-zeitbreak1>1000)f2=0;
}
```

114

```
digitalWrite(ledPin,HIGH);


zeitbreak1=millis();
while(digitalRead(switchPin)==HIGH& &f2!=0)
{
if(millis()-zeitbreak1>1000)f2=0;
}
Zeit2=millis();
digitalWrite(ledPin,LOW);


if(f2==0)f=0;
else f=1000/(Zeit2-Zeit1);


f2=1;
}
}
else if(f>1& &f<300)
{
if(digitalRead(switchPin)==LOW)
{
zeitbreak1=millis();
while(digitalRead(switchPin)==LOW& &f2!=0)
{
if(millis()-zeitbreak1>1000)f2=0;
}
}
if(digitalRead(switchPin)==HIGH)
{
digitalWrite(ledPin,HIGH);
zeitbreak1=millis();
while(digitalRead(switchPin)==HIGH& &f2!=0)
{
if(millis()-zeitbreak1>1000)f2=0;
}
Zeit1=micros();
digitalWrite(ledPin,LOW);
while(digitalRead(switchPin)==LOW& &f2!=0)
{
if(millis()-zeitbreak1>1000)f2=0;
}
digitalWrite(ledPin,HIGH);
zeitbreak1=millis();
while(digitalRead(switchPin)==HIGH& &f2!=0)
{
if(millis()-zeitbreak1>1000)f2=0;
```

```
}
Zeit2=micros();
digitalWrite(ledPin,LOW);
if(f2==0)f=0;
else f=1000000/(Zeit2-Zeit1);


f2=1;
}
}
else
{
digitalWrite(ledPin,HIGH);
Zeit1=Zeit2=micros();
int zaehler=0;
while(Zeit2-Zeit1<500000)
{
Zeit2=micros();
if(digitalRead(switchPin)==LOW)
{
zeitbreak1=millis();
while(digitalRead(switchPin)==LOW& &f2!=0)
{
if(millis()-zeitbreak1>1000)f2=0;
}
}
if(digitalRead(switchPin)==HIGH)
{
zaehler++;
zeitbreak1=millis();
while(digitalRead(switchPin)==HIGH& &f2!=0)
{
if(millis()-zeitbreak1>1000)f2=0;
}
}
}
if(f2==0)f=0;
else f=zaehler*2;


f2=1;
}


if(f<funten)
{
if(fehler==0)strom=1;
zeitbisfehler=fehlerzeit-millis()+ausZeit;
if(halten==1& &zeitbisfehler<0){fehler=1;strom=0;}
```

```
}

if(f>foben)
{
strom=0;
ausZeit=millis();
halten=1;
}


if(funten<0)fehler=1;


if(fehler==1)strom=0;


if(strom==1){digitalWrite(stromPin1,HIGH);digitalWrite(stromPin2,HIGH);}
else {digitalWrite(stromPin1,LOW);digitalWrite(stromPin2,LOW);}


if(fehler==0)digitalWrite(fehlerPin,LOW);
else digitalWrite(fehlerPin,HIGH);


if (Serial.available()>0)
{
char i;
char buffer;
i=Serial.read();


if(i=='e')
{
foben=Serial.parseInt();
funten=Serial.parseInt();
foben=foben/100;
funten=funten/100;
//fehlerzeit=Serial.parseInt()*1000;
halten=fehler=0;
while(Serial.available())buffer=Serial.read();
}


if(i=='a')
{
while(Serial.available())buffer=Serial.read();
Serial.print(f);
/*Serial.print(',');
Serial.print(fehlerzeit);
Serial.print(',');
Serial.print(zeitbisfehler);*/
```

```
Serial.print(',');
Serial.print(strom);
Serial.print(',');
Serial.println(fehler);
/*Serial.print(',');
Serial.print(foben);
Serial.print(',');
Serial.println(funten);*/
}
}
}
```

Curriculum vitae

Name:	Juri Schroffenegger
Geburtsdatum:	05.11.1985
Geburtsort:	Bozen
Staatsbürgerschaft	Italien

Ausbildung

Seit 12.2012	Doktorat technische Physik: "Giant absorption of neutrons", Technische Universität Wien
6.2011	Dip. Ing. technische Physik, Technische Universität Wien
9.2010-6.2011	Diplomarbeit: "Neutronenstreulängenmessung mit Christiansenfilter im Neutroneninterferometer", Technische Universität Wien, Betreuer: Prof. Helmut Rauch
2004-20011	Physikstudium an der Technischen Universität Wien Projektarbeiten: Physikalische Datenerfassung: MP35N als Trägermaterial in einem Puslfeld-Magnetometer Neutronenphysik: Messung von Neutronenstreulängen mit Christiansenfilter Radiochemie: Messung von in Wasser gelösten Rn
1999-2004	Realgymnasium Bozen / Liceo scientifico Bolzano
1996-1999	Mittelschule Blumau / Scuola media Prato Isarco
1991-1996	Volksschule Steinegg / Scuola elementare Collepietra

Berufserfahrung:

Seit 11.2013	Forschungsassistent (Doktorand), Technische Universität München, FRM II
12.2011-4.2013	Projektassisten (Doktorand), Technische Universität Wien, Atominstitut
5-9.2011	Werkverträge, Technische Universität Wien, Atominstitut
7-9.2009	Praktikum, Labor für physikalische Chemie Bozen/Labratorio di chimica fisica Bolzano, Bereich Radiochemie

Stipendien:

2012	Leistungsstipendium der Autonomen Provinz Bozen Südtirol

Veröffentlichungen:

Improved measurement of the neutron absorption cross section for very low velocities
J. Schroffenegger et al. Physics Letters B, 752:212 – 216, (2016)

Deuterated polyethylene coatings for ultra-cold neutron applications
G. Petzoldt et al., Appl. Phys. Lett. 107, 121604 (2015)